CRANFIELD UNIVERSITY

WEI WANG

Simulation of Hard Projectile Impact on Friction Stir Welded Plate

School of Engineering
MSc Thesis

MSc by Research
Academic Year: 2010- 2011

Supervisor: Dr Tom de Vuyst
December 2011

CRANFIELD UNIVERSITY

School of Engineering
MSc Thesis

Master of Science

Academic Year 2010- 2011

WEI WANG

Simulation of Hard Projectile Impact on Friction Stir Welded Plate

Supervisor: Dr Tom de Vuyst
December 2011

ABSTRACT

A numerical simulation is conducted using LS-DYNA to simulate hard projectile impact on a friction stir welded (FSW) plate. As the hard projectile has a wide range of velocity, mass and shape, when referring to AMC 25.963(e) of CS-25, “Fuel Tank Access Cover”, the hard projectile can be defined as 9.5 mm cubic-shaped steel engine debris with an initial impact velocity of 213.4 m/s (700 ft/s).

This preliminary study was to evaluate whether the fuel tank adjacent skin panel joined by FSW would pass the regulation. First, the geometry and Johnson-Cook material model of the FSW joint were developed based on previous experimental research and validated by comparison with the tensile test on the FSW specimen. Then the impact on an Aluminium Alloy 2024 (AA 2024) plate without FSW was modelled. The minimum thickness of a homogeneous AA 2024 plate which could withstand the impact from engine debris is 3 mm. Finally the impact on 3 mm thick AA 2024 FSW plate was simulated. The welding induced residual stress was implemented in the plate model. The impact centre was changed from the nugget zone to the thermo-mechanically affected zone, heat-affected zone and base material zone of the FSW joint. Penetration only occurred in the model with impact centre on the nugget zone. Additional simulation indicated that increasing the thickness of the FSW plate to 3.6 mm could prevent the penetration.

Keywords:

LS-DYNA, hard projectile, impact, FSW, AMC 25.963(e), Johnson-Cook material model, AA 2024, penetration

This page is intentionally left blank

ACKNOWLEDGEMENTS

I sincerely thank Dr Tom de Vuyst for giving me guidance and help throughout my research. I am also grateful to Dr James Campbell and Dr Al Savaris for their help.

Yang Wang and Chuanliang Guo have shared their experience of modelling and I appreciate for their help.

In addition, I would like to thank my company COMAC for being my sponsor.

Last but not least, I would like to thank my parents for their moral support.

This page intentionally is left blank

TABLE OF CONTENTS

LIST OF FIGURES

LIST OF TABLES

LIST OF ABBREVIATIONS

AS – Advancing Side

BM – Base Material

EOS – Equation of State

FE – Finite Element

FEA – Finite Element Analysis

FSW – Friction Stir Welding

FOD – Foreign Object Damage

HAZ – Heat Affected Zone

RS – Retreating Side

TMAZ – Thermo-Mechanically Affected Zone

TWI – The Welding Institute

1 Introduction

The joining process is inevitable in aircraft manufacture as an aircraft is assembled from many parts. Rivets have been commonly used in aircraft structural joining. Generally, the riveting process costs much manufacture time and rivets increase the structural weight. A new joining process has been developed, which is more efficient and would provide benefit from weight saving in the aircraft structure. This joining process is called friction stir welding (FSW).

FSW is a solid-state welding process. It does not melt the metal because of the low input of total heat. In addition, the material is finely recrystallized in the welded zone. Thus, friction stir welded joints with finer and uniform microstructure have better material property compared with other conventional fusion welding processes [1].

Today, FSW process is considered to be a promising technology which would substitute riveting in joining aircraft skins. However, before this new process can successfully be applied in aircraft manufacture, a wide range of tests and analyses need to be done in order to guarantee that the skins joined by FSW are able to remain safe during the service life of the aircraft.

Foreign Object Damage (FOD) may cause severe danger to the exterior skin, such as bird-strike, hard projectile impact and so on. As the welded joints are considered to bring the weakness to the FSW skin, it is necessary to analyse the dynamic response due to impact on the friction stir welded skin.

Many experiments have been carried out to show the microstructure of friction stir welds and investigate the material properties of the welds. Based on the experimental data, previous numerical studies have been performed to simulate bird-strike impact on the FSW plate [2]. However, this current thesis will perform simulations of impact from hard projectiles and analyse the dynamic response of the friction stir welded plate after impact to evaluate whether this process is suitable for jointing aircraft skins according to Aviation Regulations.

1.1 Friction Stir Welding (FSW)

FSW is an emerging method of welding. It was created in 1991 at The Welding Institute (TWI), Cambridge, UK. When compared with conventional joining methods, this technology in manufacture has advantages including the capability to reduce structural weight cost and time. In addition, this welding process provides the capacity of welding dissimilar metals.

1.1.1 Friction Stir Welding Process

Figure 1-1 illustrates the FSW process. During the process, the plates to be welded are put firmly into contact and secured to prevent from being apart. The welding tool, which is comprised of pin and shoulder, rotates at a high velocity and then plunges into the abutting edges of the sheets.

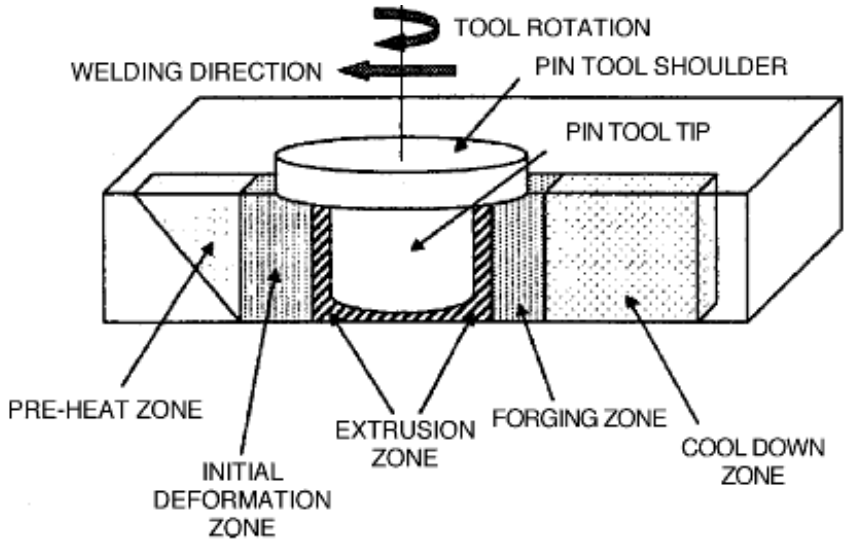

Figure 1-1 Illustration of the FSW Process [1]

Great heat is caused due to the friction between the sheets and the tool. The plastic deformation of the work piece also heats the material. Then the increasing heat softens the material, while the rotating pin mixes the soft material in the zone around the pin. As shown in Figure 1-1, the material is heated in the pre-heat zone, while the material behind forges and cools into welding joints.

1.1.2 Applications

Since FSW was invented, it has received attention from a wide range of industries. Today, FSW technology is being widely used in the aerospace, automotive and railway industries.

In the automotive industry, the use of aluminium alloys together with FSW joining techniques helps to create lighter and more economical car construction.

FSW technology is used in the aerospace industry. This technology brings significant weight savings into aluminium fuselage construction where riveting is usually the main method of joining.

In commercial aircraft manufacture, this process has been successfully applied in the Eclipse 500 Very Light Jet. The FSW process substitutes the riveting process in most assembled structures. As shown in Figure 1-2, in the after fuselage, instead of riveting, the FSW process is used in the assembly process.

Figure 1-2 FSW process applied in the Eclipse 500 Very Light Jet [3]

It is reported that using FSW brings two major benefits in this aircraft. First, up to 136m welds per jet eliminate about 7,380 rivets, which reduce the structural weight. In addition, as friction stir welding can be operated in automation, it can also reduce dramatically time cost up to 1,800 hours per jet in manufacture [3].

1.2 Hard Projectile Impact

Hard projectile impact causes great danger to an aircraft. An extremely dangerous situation is the fuel tank adjacent components being impacted on by high velocity objects such as failed tyre segments or failed engine parts.

On November 4th 2010 at the Singapore Chanqi Airport, Qantas Flight 32, Airbus A380 was forced to make an emerging Landing due to uncontained engine failure. The investigation showed that No. 2 engine failed and caused damages to nacelle, wing, fuel system, landing gear and flight control system [4]. Figure 1-3 presents the failed engine and Figure 1-4 illustrates the damage to the left wing inner fuel tank after engine failure.

Figure 1-3 Pictures of Qantas 32 A380 engine failure [4]

Figure 1-4 Damage to left wing inner fuel tank [4]

In AMC 25.963(e) of CS-25 [5], the fuel tank access cover must be designed to withstand the impact caused by failed tyre segments or engine debris.

The assessment method is to compare the dynamic response between the access cover and the adjacent skin panel without the access cover, which means that the skin panel must also be resistant to this impact as well.

This research is concerned with the skin panel with friction stir welded joints. Since Aluminium Alloy 2024 (AA 2024) is commonly used in aircraft skin [6], the target skin panel to be studied in this research is the AA 2024 FSW plate. In addition, as engine debris is kind of hard projectiles, the current study will focus only on the impact caused by engine debris. The requirement of the assessment is that no penetration is acceptable after impact.

1.3 Objective

The objectives of this project are:

- Building a finite element (FE) model for a friction stir welded plate
- Performing simulations to study the effect of the impact on AA 2024 FSW plate from engine debris using LS-DYNA

- Comparing the dynamic response with the impact on AA 2024 plate without FSW
- Evaluating whether the Aluminium Alloy 2024 skin panel jointed by FSW can remain safe after impact according to regulation AMC 25.963(e) of CS-25.

1.4 Outline of Thesis

Chapter 2 is the literature review including the following relevant studies: the material properties of AA 2024 FSW plate; the residual stress in the FSW structure; the introduction of LS-DYNA; a review of an experimental study on Aluminium Alloy 2024 friction stir welded plate. The requirement of the fuel tank access cover in regulation AMC 25.963(e) of CS-25 will be introduced and the detail of the projectile will be described such as the material, the dimensions and the impact velocity.

Chapter 3 introduce the methodology of this research.

In Chapter 4, a finite element model of FSW joint is built with FSW geometry and material properties. Then the model is validated by comparison with global tensile test specimen.

Chapter 5 presents the penetration model of the AA 2024 plate without FSW joint and comparisons with the experiments. The mesh size will be concentrated on due to its significant influence on ballistic limits. This chapter also contains the simulation of the impact on homogeneous aluminium plate from engine debris according to Regulation AMC 25.963(e) of CS-25. The result of this simulation will determine the minimum thickness of the homogeneous aluminium plate which can withstand the impact.

After mesh size and the minimum thickness have been determined, in Chapter 6 the final impact models of friction stir welded plate are built to assess whether skin panels with friction stir welded joints can remain safe after impact.

Chapter 7 gives the conclusions and several recommendations for future work.

2 Literature Review

This review presents the current level of the knowledge and findings relevant to this thesis. The review includes following parts:

- the microstructure of the FSW joint;
- the experimental studies has been carried out to obtain the mechanical properties of the AA 2024 FSW joint;
- the Johnson-Cook model and data fitting method used for implementing the mechanical properties;
- the residual stresses in FSW joint and its measurement methods;
- experimental study of engine fragments impact on AA 2024 homogeneous plate;
- details of Regulation AMC 25.963;
- the FE software LS-DYNA used in this research.

2.1 Microstructure of the Friction Stir Weld Joint

As shown in Figure 2-1, the microstructure of the FSW joint is divided into four regions: the nugget, the thermo-mechanically affected zone (TMAZ), the heat-affected zone (HAZ) and the base material (BM) [7].

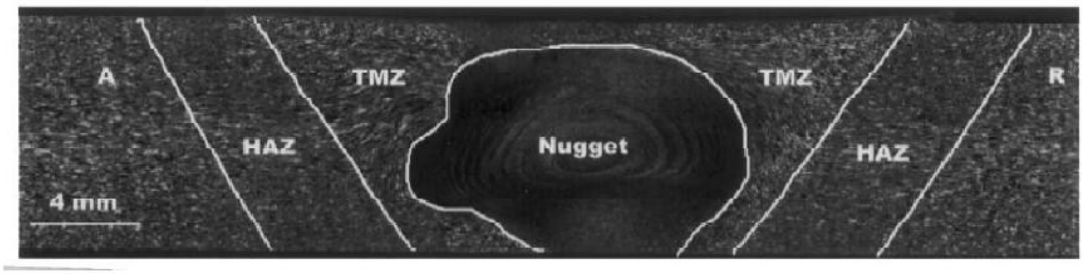

Figure 2-1 Microstructural zones in friction stir welded Aluminium Alloy 2024 joint [8]

(1) In the “stirred zone” the material is recrystallized due to the heat and plastic deformation, which results in a refined grain. This zone is defined as the “nugget”. The shape of the nugget is affected by welding tool geometry, welding parameter and the base material. Reynolds [9] found the relationship between nugget size and pin size, reporting that the nugget zone is generally slightly bigger than the diameter of the pin.

(2) The Thermo-mechanically affected zone (TMAZ) also experiences heat and plastic deformation during the friction stir welding. However, the plastic deformation is not as much as that in the nugget zone because no stir occurs there. Thus the material in TMAZ zone is not recrystallized due to insufficient plastic deformation. The relationship between the TMAZ zone size and the tool size has been also investigated.

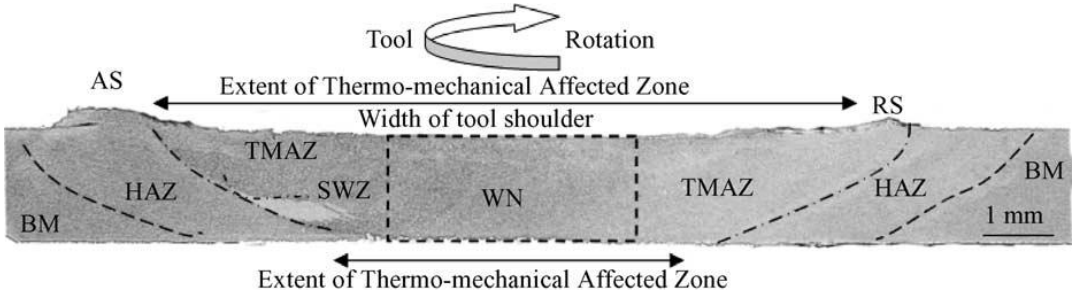

Figure 2-2 Microstructure of AA 2095 FSW sheet [10]

It is reported that the size of the TMAZ upper side is the shoulder diameter and the width of its base is approximately the pin diameter [10]. Figure 2-2 shows the relationship between the shoulder width and the TMAZ zone dimension. As shown in Figure 2-2 “AS” and “RS” are advancing side and retreating side respectively. In FSW process the rotating tool moves the material around the pin from the advancing side to the retreating side.

(3) The HAZ is between the TMAZ zone and the BM. This zone only experiences heat without any plastic deformation.

(4) BM experiences neither heat nor plastic deformation.

2.2 Mechanical Properties of FSW Joints

2.2.1 Global Mechanical Properties of the FSW Joint

Chao et al. [11] used split Hopkinson pressure bar technique to determine the compressive plastic stress-strain of AA 2024 and AA 7075 FSW joint at different strain rates. Figure 2-3 indicates that the yield stress of friction stir welds is lower than that of base material.

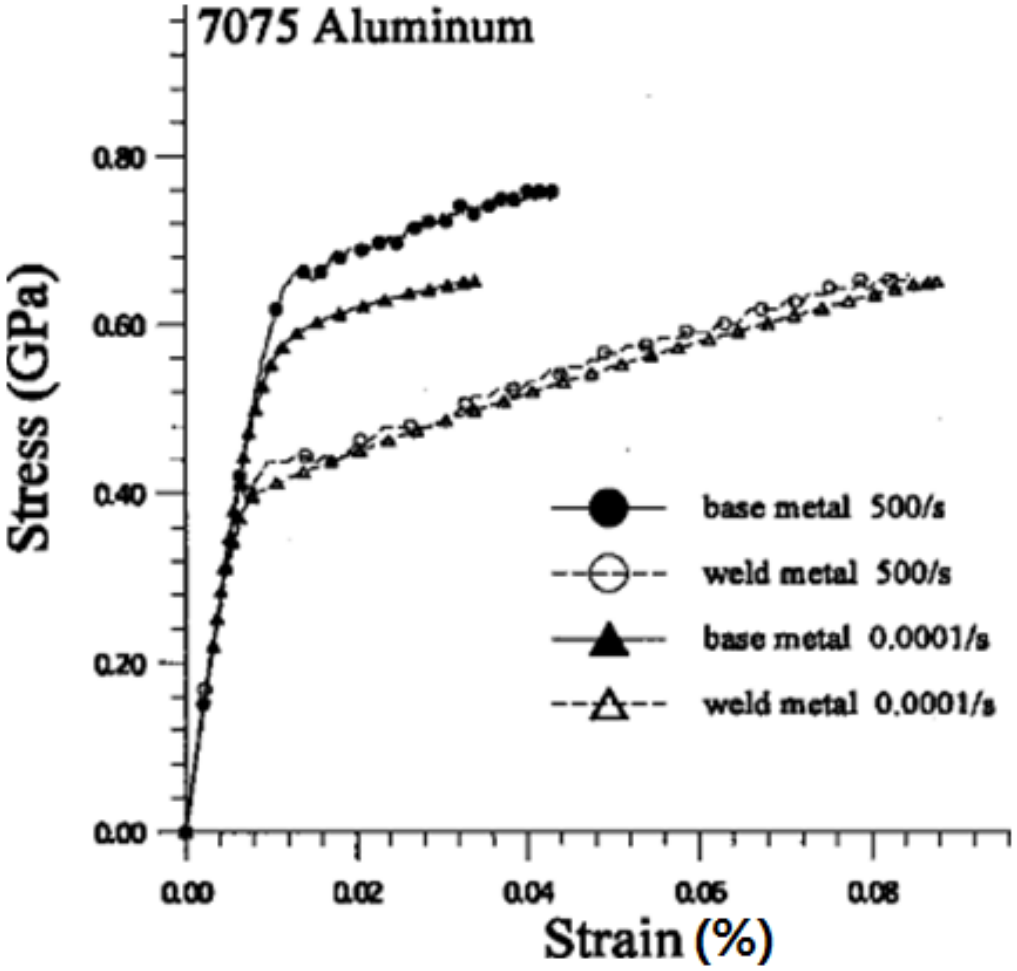

Figure 2-3 Compressive stress-strain curves for AA 7075 FSW joint [11]

Moreiva et al. investigated tensile mechanical properties of AA 6082/6061 friction stir welds [12].

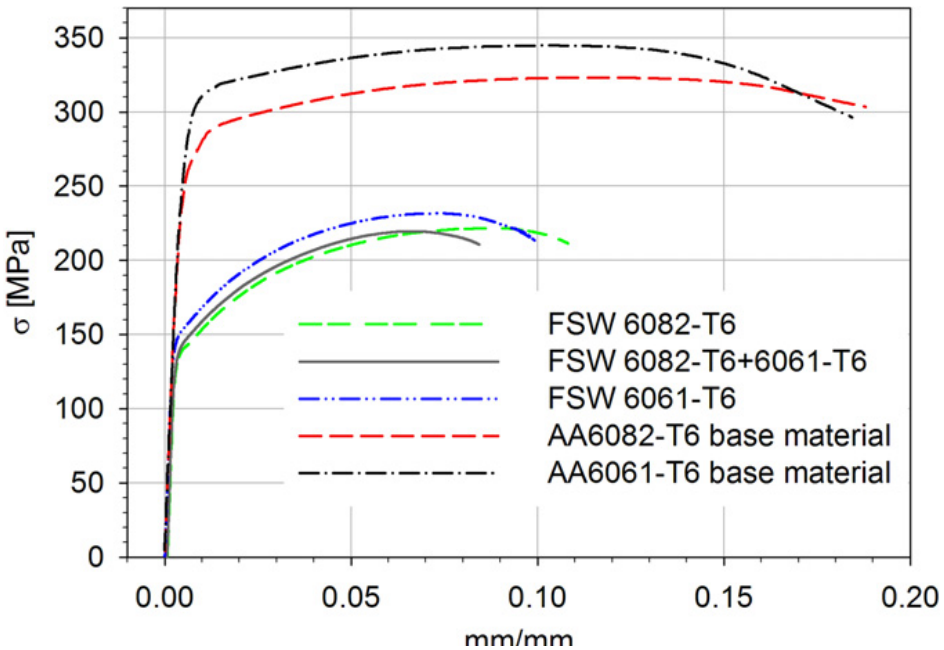

Figure 2-4 Tensile stress-strain curves of FSW AA 6082/6061 [12]

Figure 2-4 shows that the strength of FSW is lower than that of base material in tension condition. Based on the experiments above, it can be concluded that the FSW could weaken the base material.

2.2.2 Local Mechanical Properties of the AA 2024 FSW Joint

The mechanical properties of the nugget, TMAZ and HAZ can be heterogeneous. Implementing global mechanical properties in FE model of FSW joint might be insufficient to get an accurate simulation. Thus local stress-strain curves of each zone in the AA 2024 friction stir welds are required in this thesis.

Genevois [13] has performed experimental research on local material properties of each zone in the Aluminium 2024-T351 FSW plate. The original Aluminium 2024-T351 plate is 495 mm × 150 mm × 6 mm thick plate. The FSW parameters are: the rotation speed of the pin is 850 rpm and the welding speed is 120 mm/min.

In his research, Genevois used two different methods to obtain the mechanical properties of each zone in the welds. One is the digital image correlation method; the other is local micro-tensile tests.

2.2.3 Digital Image Correlation Method

Digital image correlation is a technique of tracking and image analysis, which is used for accurate measurements of changing of images, such as deformation, displacement and strain.

Genevois used the digital image correlation (DIC) method in macro tensile tests for strain mapping to acquire the local stress-strain curves. The macro specimen was taken perpendicular to the direction of welding, as shown in Figure 2-5.

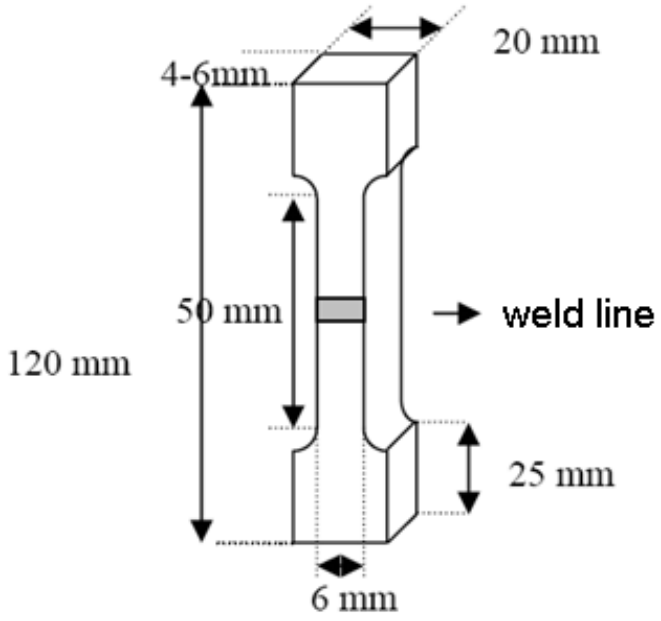

Figure 2-5 Macro tensile specimen [13]

2.2.4 Micro-Tensile Tests

The micro-tensile specimens are cut in the different zones of the FSW joint, parallel to the welding line, as shown in Figure 2-6. The micro specimen is 0.8 mm wide and the tension strain rate is $1.15 \times 10^{-4}\ s^{-1}$ [13].

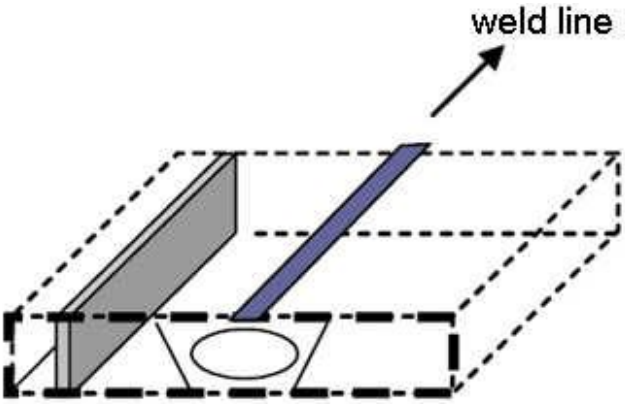

Figure 2-6 Cutting micro specimen [13]

The geometry of the local micro-tensile specimens is shown in Figure 2-7.

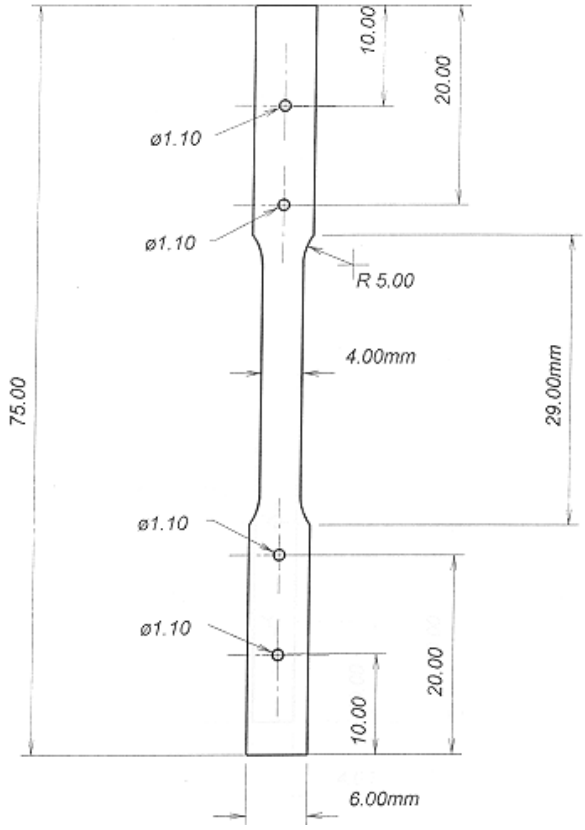

Figure 2-7 Micro specimen [13]

2.2.5 Test Results

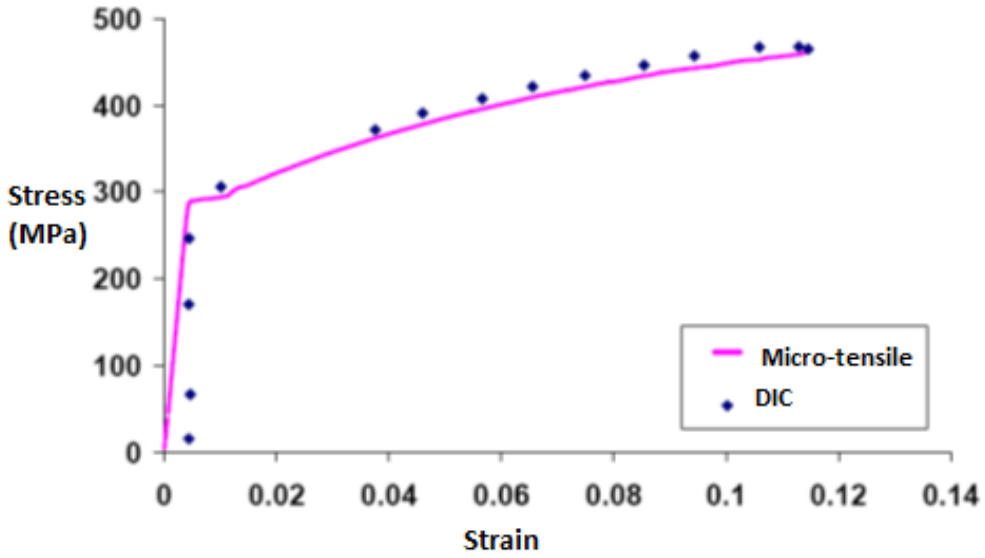

(a) Nugget

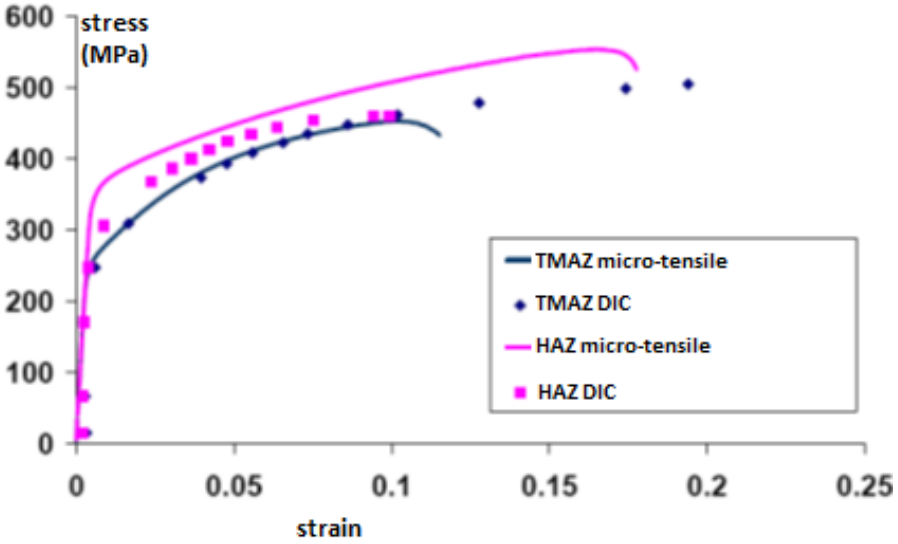

(b) TMAZ and HAZ

Figure 2-8 True stress-strain curves of Nugget, TMAZ and HAZ [13]

Figure 2-8 presents the true stress-strain curves determined by these two methods: (a) is the curve of the nugget zone and (b) is those of TMAZ and HAZ. The line curve presents the stress-strain curve obtained by micro-tensile tests, while the dot curve is determined by the DIC method.

The results show that the stress-strain curves of the Nugget zone and TMAZ zone obtained by these two methods are very close. However, the curves of HAZ are different.

2.2.6 Global Tensile

Genevois also performed global tensile test to determine the global force-displacment curve of FSW macro specimen. Meanwhile he used finite element method to simulate the global tensile test. The comparison of the simulations and experiment is shown in Figure 2-9. The line curve is the result of the global tensile experiment. The dot curves are results of simulations.

“traction” is the global tensile experiment; CASTEM is finite element software used for simulations; “Castem corrélation” is the simulation based on the material properties obtained from the DIC method and “Castem micro-éprouvette” is the simulation based on the material properties obtained from Micro-tensile test.

The result of the global tensile experiment shows that the failure occurs at about 3 mm applied displacement.

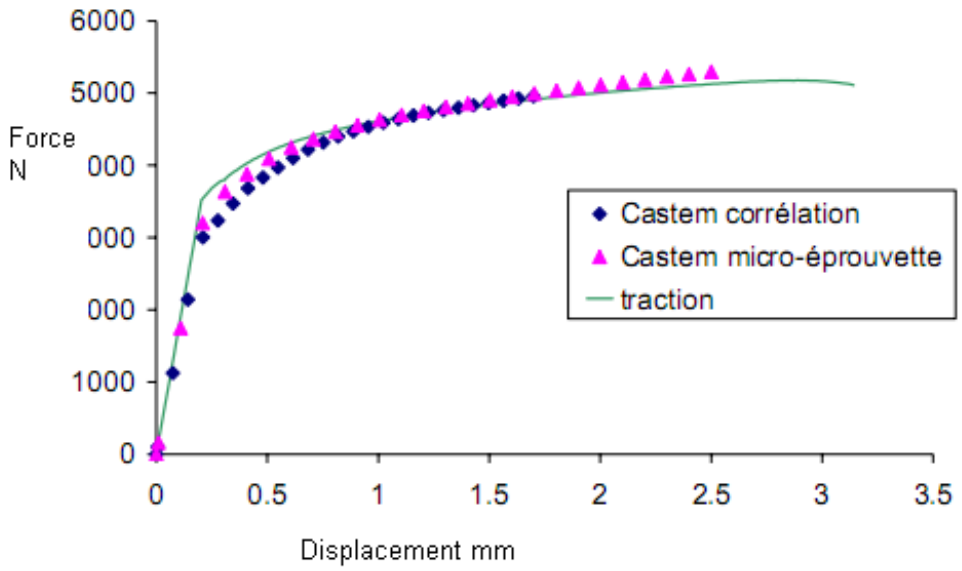

Figure 2-9 Comparison of the simulations and experiment of global tensile experiment [13]

2.2.7 Conclusion of the Experiments

By using digital image correlation method, the strain-stress curves of all regions in FSW joint can be measured in only one macro tests, whereas the micro-tensile tests need several micro-tensile specimens cut from different zones of the FSW joint. Thus digital image correlation method is faster and easier than micro-tensile tests.

However, the limitation of the digital image correlation method is that it only obtains the tensile result for the weakest zone. The fracture condition can only be determined in one zone where failure occurs. In addition, Genevois [13] found the digital image correlation method difficult to obtain the stress-strain curve in the elastic region due to lower strains in that region. Thus the stress-strain curve obtained by micro-tensile tests is better.

The stress-strain curves determined by micro-tensile tests can be plotted in one figure, as shown in Figure 2-10.

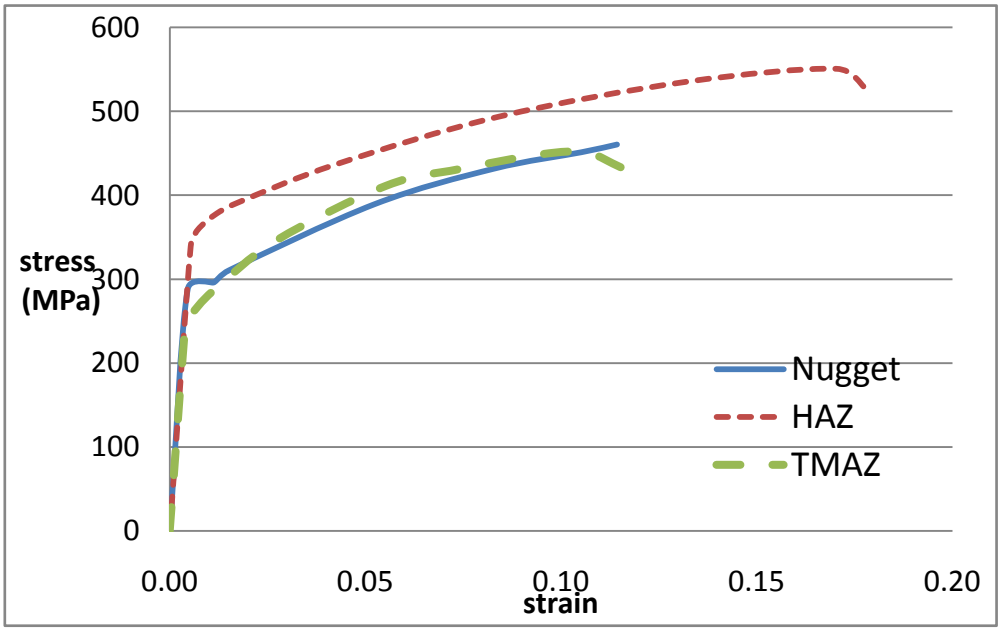

Figure 2-10 Comparison of Nugget, TMAZ and HAZ stress-strain curve

The stress-strain curves of Nugget, TMAZ and HAZ are the same in the elastic region. However, in the plastic region the mechanical properties of TMAZ and Nugget are similar and the failure of these two tension test occurs

approximately the same, whereas the mechanical property of HAZ is strongest and failure occurs much later than with TMAZ and Nugget.

In micro-tensile tests, an extensometer is used to measure the extension. The extensometer underestimates the extension at the necking area because it cannot measure the exact local deformation but averages it on the whole specimen. The strain ε can be calculated as:

$$\varepsilon = \frac{\Delta l}{l_0} \quad \text{(2-1)}$$

As the extension measured in the necking area is lower than the real one, the plastic strain at failure obtained by micro-tensile tests is lower. A more accurate plastic strain at failure can be determined by simulations in Section 4.2.3.

2.3 Implementing Mechanical Properties of FSW in FE Models

Mechanical properties can be implemented in FE models by using various material models in LS-DYNA. Johnson and Cook [14] developed the Johnson-Cook model for material subjected to large strains, high strain rates and high temperatures for the purpose of dealing with the computations of high-velocity impact and explosion. This material algorithm is suitable for impact analysis which is involved in high strain rate in very short termination. The coefficients of this model can be determined according to the stress-strain curves.

Based on the local stress-strain curves in Figure 2-8, Lansiaux used data fitting method and developed the Johnson-Cook simplified material model for each zone in AA 2024 FSW plate [2].

2.3.1 Johnson-Cook Model and Johnson-Cook Simplified Model

The Johnson-Cook simplified material model represents the plastic stress with the following equation:

$$\sigma_y = (A + B\varepsilon_p^n)(1 + C\ln\dot{\varepsilon}_p^*) \text{ [15] (2-2)}$$

where A, B and C are constant parameters; n is the strain hardening exponent; σ_y is the effective plastic stress; ε_p is the effective plastic strain. In equation (2-2) $\left(\mathrm{A}+\mathrm{B}\varepsilon_{\mathrm{p}}^{\mathrm{n}}\right)$ presents the strain hardening characteristic of the material and $\left(1+\mathrm{C}\ln\dot{\varepsilon}_p^*\right)$ expresses the strain rate hardening characteristic.

$\dot{\varepsilon}_p^*$ is the normalized strain rate, and $\dot{\varepsilon}_p^*$ can be described as:

$$\dot{\varepsilon}_p^* = \frac{\dot{\varepsilon}_p}{\dot{\varepsilon}_o} \quad (2\text{-}3)$$

$\dot{\varepsilon_0}$ is the reference strain rate, which is set to 1.0 s^{-1}; $\dot{\varepsilon_p}$ is the effective plastic strain rate.

Compared with the Johnson-Cook model, the simplified model is faster in computations as the thermal effects and damage are ignored in the simplified model. The equation of the Johnson-Cook model can be expressed as:

$$\sigma_y = (A + B\varepsilon_p^n)(1 + C\ln\dot{\varepsilon}_p^*)(1 - T^{*m}) \text{ [15] (2-4)}$$

Where $(1-\mathrm{T}^{*\,\mathrm{m}})$ describes the softening effect of the increasing temperature caused by the plastic work; m is constant parameter. T* is the homologous temperature, which can be expressed as:

$$T^* = \frac{T - T_{Room}}{T_{Melt} - T_{Room}} \quad (2\text{-}5)$$

T is the current temperature, T_{Melt} is the melting point temperature, and $\mathrm{T_{Room}}$ is the room temperature.

In the Johnson-Cook simplified material model the effective plastic strain at failure is defined by a constant strain. However, in the Johnson-Cook model the plastic strain at failure is defined by the damage coefficient, which can be expressed as:

$$\varepsilon_p(atfailure) = [D_1 + D_2\exp(D_3\sigma^*)](1 + D_4\ln\dot{\varepsilon}_p)(1 + D_5T) \text{ [15] (2-6)}$$

where D_1, D_2, D_3, D_4 and D_5 are the damage coefficient; $\dot{\varepsilon_p}$ is the strain rate; T is the temperature and $\sigma^*$is the mean stress (σ_m) normalized by the effective stress (σ_{ep}), which is often referred to as triaxiality [16]. In equation (2-6) $(1 + D_4 ln\dot{\varepsilon_p})$ expresses the strain rate influence on the strain at failure; $(1 + D_5 T)$ describes the thermal effect and $D_2 \exp(D_3 \sigma^*)$ shows the effect of different triaxialities.

2.3.2 Data Fitting Method

Data fitting method is to use the least squares method. According to equation (2-2), the Johnson-Cook simplified model, the stress σ_y is the function of strain ε_p. An x-y function can be built, where x is the strain and y is the stress; $i = 1 \ldots n$.

$$y_i = f(x_i : (A; B; n)) = (A + Bx_i^n)(1 + C \ln x_i) \quad (2\text{-}7)$$

When defining values for x_i, another stress (y_i) and strain (x_i) curve can be plotted by equation (2-7).

The error between the test curve and the curve plotted by Johnson-Cook simplified material model can be calculated as:

$$r_i = y_{test} - y_i = y_{test} - f(x_i; (A; B; n; C)) \quad (2\text{-}8)$$

The square

$$S = \sum_{i=1}^{n} r_i^2 \quad (2\text{-}9)$$

Figure 2-11 illustrates the data fitting method. When refining the coefficient of A, B, n and C, the error can be reduced.

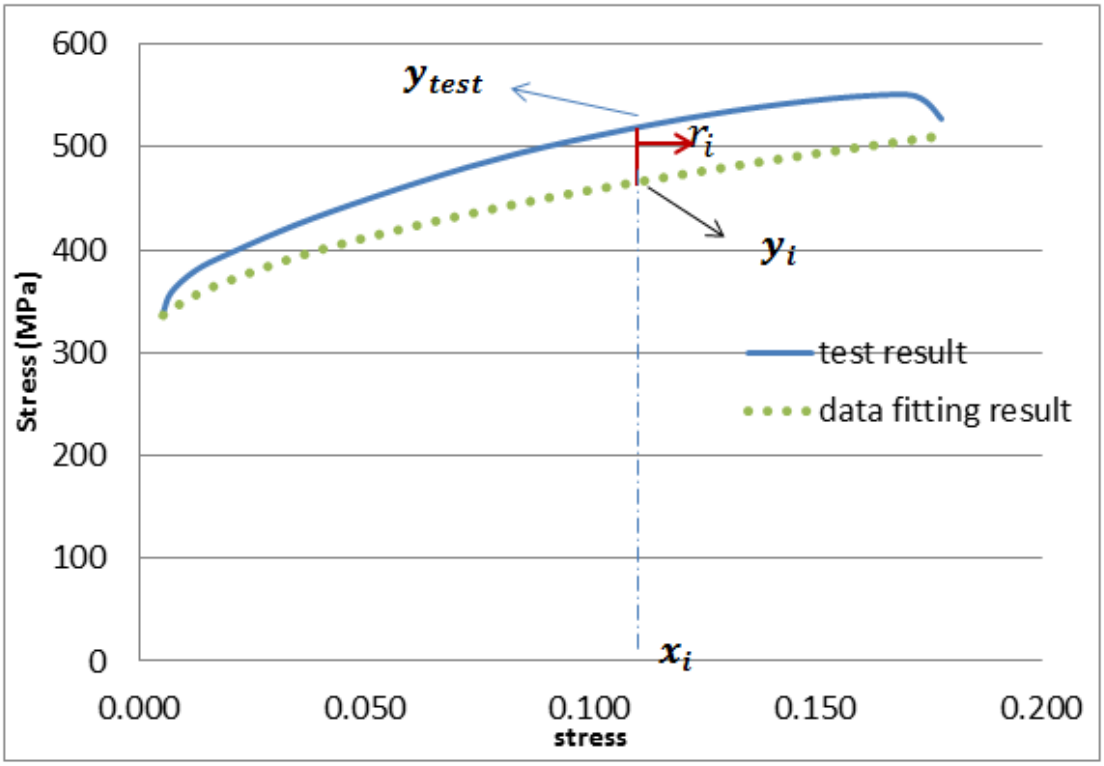

Figure 2-11 Illustration of data fitting

The best determination of the constants A, B, n and C will be able to minimise the sum of the residual squares. However, due to the lack of different strain rate local tensile tests of each zone in the AA2024 FSW plate, the parameter C cannot be defined. Thus Lansiaux [2] set C as zero in his research.

After data fitting, Lansiaux gave the Johnson-Cook simplified model for each zone in the AA 2024 FSW plate, as shown in Table 2-1.

Table 2-1 Parameters of the Johnson-Cook simplified model

	Density (g/cm^3)	Elastic modulus (Gpa)	Poison ratio	A (Mpa)	B (Mpa)	N
Base material	2.77	73.1	0.33	352	440	0.42
Nugget	2.77	73.1	0.33	326.41	585.18	0.501
TMAZ	2.77	73.1	0.33	139.28	632.48	0.290
HAZ	2.77	73.1	0.33	248.50	714.59	0.537

2.4 Residual Stress

The residual stress in the FSW joint is induced by both heating and plastic deformation. During the FSW process the material in the welds expands due to the high temperature, and then contraction of the welds occurs due to the cooling of the welds. However the base material of the welded plates prevents the contraction of the welds, resulting in residual stress in both longitudinal and transverse direction.

2.4.1 Residual Stress Measurement Methods

Several methods have been developed to measure residual stresses. By using the X-ray diffraction method, James and Mahoney [17] obtained residual stress in the 7050Al-T7451 FSW joint.

The cut compliance method [18] is used to measure the longitudinal residual stress (y direction, welding line, as shown in Figure 2-12).

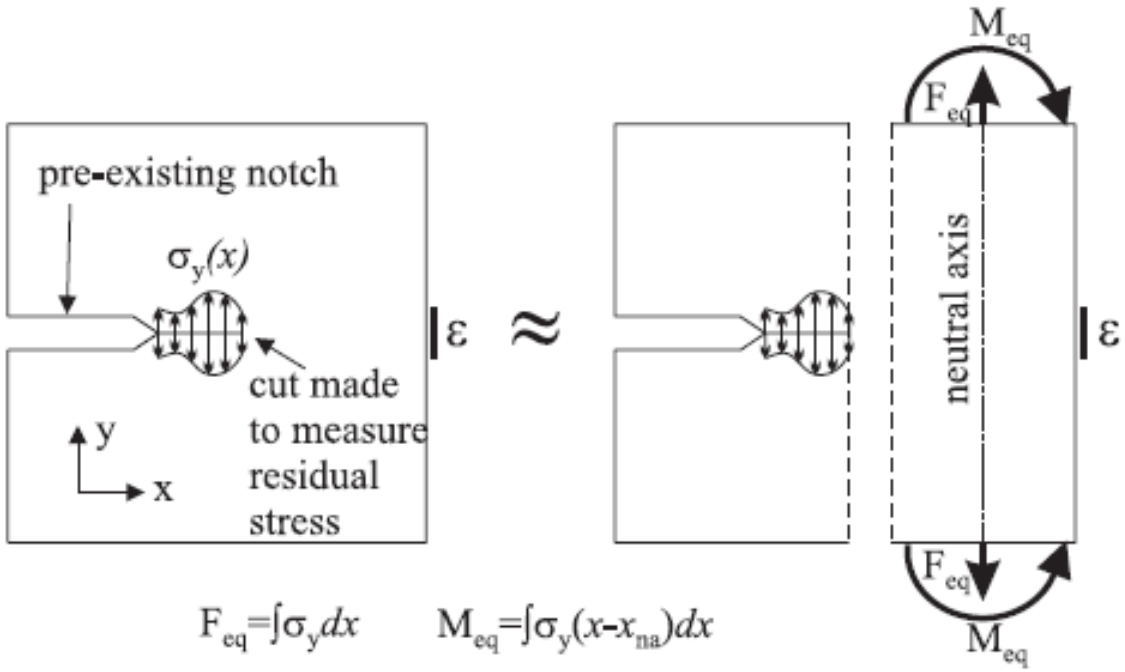

Figure 2-12 Cut compliance specimen [18]

By saw cutting along the notch (x direction), the residual stress releases and causes the residual strain. The gauge ε can be measured. Then the residual stress can be calculated by an equivalent of force and moment.

By using the cut compliance method, Buffa et al. [19] measured the longitudinal residual stress in a 3 mm thick AA7075-T6 plate. Figure 2-13 presents the measured residual stresses with pin and without pin. The figure also shows the shoulder size is 12 mm (the pin size is described as 4 mm in [19]).

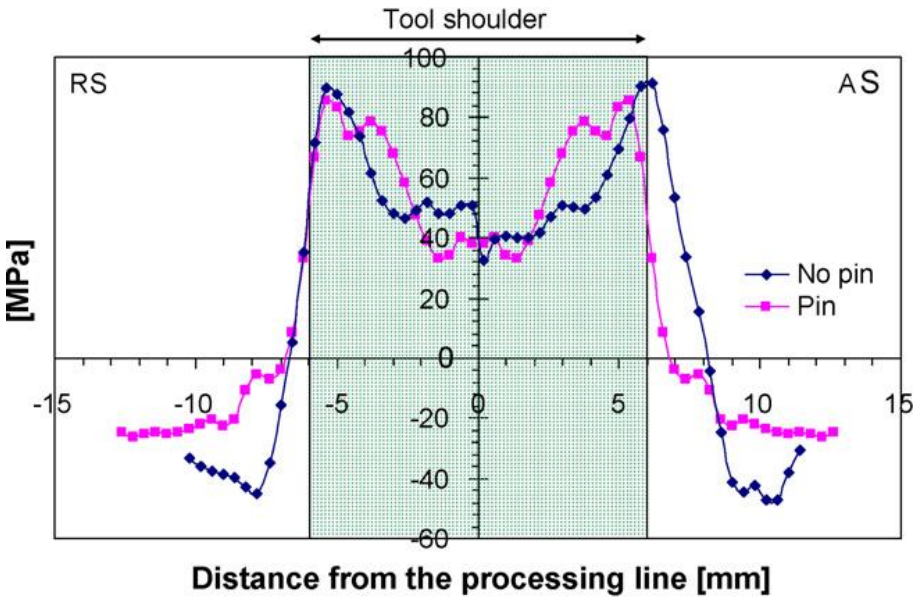

Figure 2-13 Longitudinal residual stresses of AA 7075 FSW plate [19]

2.4.2 Characteristic of FSW Residual Stress

Chen and Kovacevic [20] measured the longitudinal and transverse residual stress in Aluminium 6061-T6 plate and performed simulations to predict the residual stress in each direction. As shown in Figure 2-14, the longitudinal residual stress (x direction) is much larger than that in transverse one (z direction).

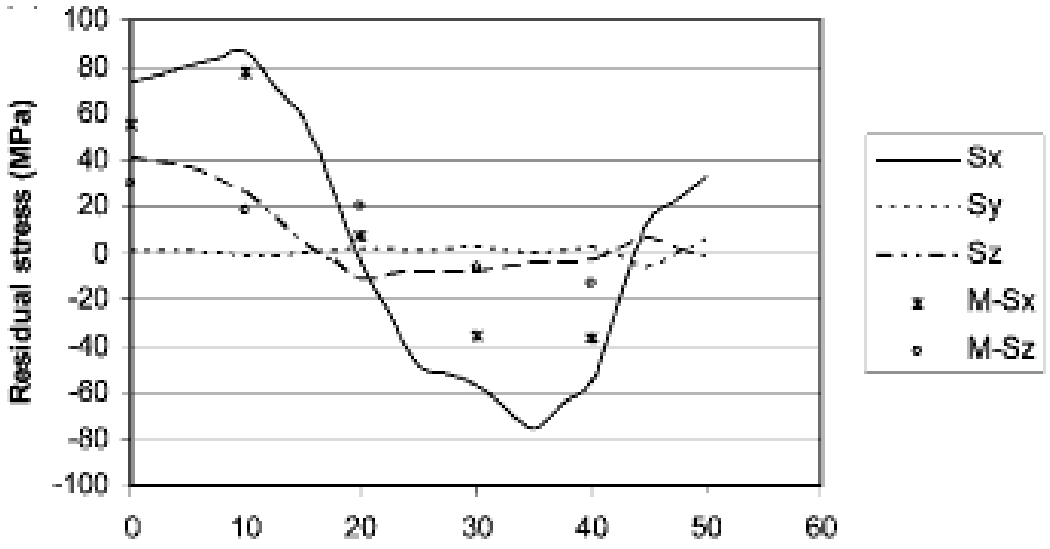

Figure 2-14 Simulated (S) residual stress in x, y, z direction and measured (M) residual stress (x is the longitudinal direction; z is the transverse; y is the direction through thickness) [20]

Several similar studies [21-23] on the residual stress measurement on FSW joints have generalized the typical characteristics of an FSW aluminium alloy joint: first, the longitudinal residual stress is much greater than the transverse one; second, the longitudinal residual stress forms an M-shape curve.

Since the transverse residual stress is much lower than the longitudinal one, this thesis is only concerned with longitudinal residual stress.

2.4.3 Implementing Longitudinal Residual Stress in FE Model

Based on Figure 2-13, Lansiaux [2] used trigonometric polynomials to decompose the longitudinal residual stress and developed a programme to implement it in FE model.

The original curve in Figure 2-13 does not reach the static equilibrium between tension and compression, thus needs to be altered (shown in Figure 2-15) first. Put simply, the method is that the area below zero MPa (compression stress) should equal that up to zero MPa (tension stress).

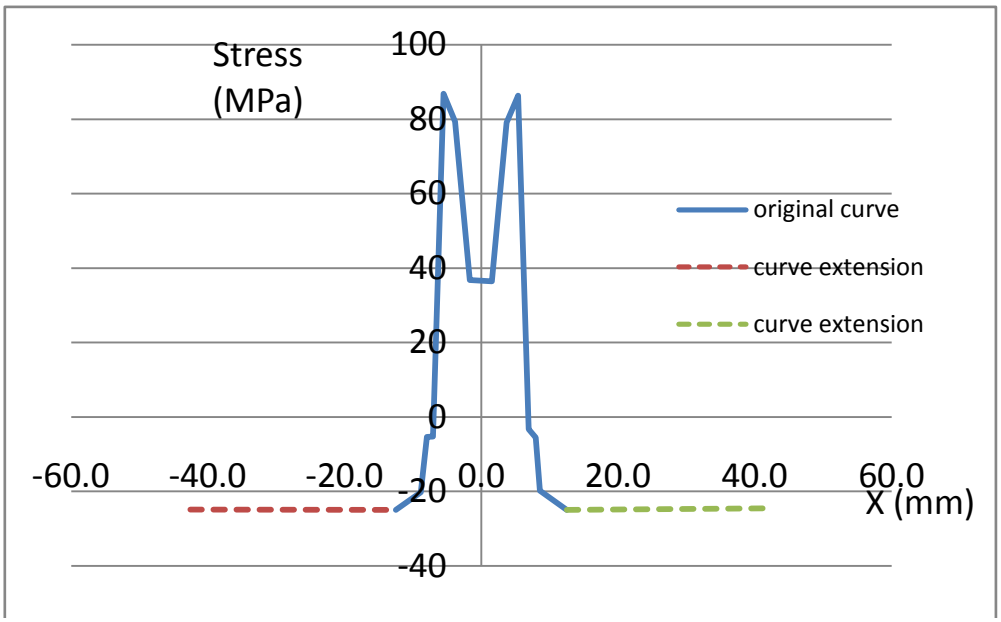

Figure 2-15 Altered longitudinal residual stress

The compression stress is extended from ± 12.5 mm to ± 42.5 mm and the value remains the same (24.52 MPa).

A programme can be developed to implement longitudinal residual stress by using trigonometric polynomials which can be expressed as:

$$f(x) = cn + \sum_{n=1}^{N} a_n \cos(n\omega x) + \sum_{n=1}^{N} b_n \sin(n\omega x) \quad (2\text{-}10)$$

Where

cn is a constant

N is the order of the interpolation

n is the index

a_n is the even parameters

b_n is the odd parameters

ω is the pulsation or angular frequency.

As $\sum_{n=1}^{N} a_n \cos(n\omega x)$ is a basis of even functions and $\sum_{n=1}^{N} b_n \sin(n\omega x)$ is a basis of odd functions, the curve in Figure 2-15 can be fitted by the summing of these forms.

As the longitudinal residual stress presents an even curve, the function $f(x)$ should be even as well. Then the function can be expressed as:

$$f(x) = cn + \sum_{n=1}^{N} a_n \cos(n\omega x) \quad (2\text{-}11)$$

After data fitting, Lansiaux [2] gave the coefficients of the interpolation when N was set to 10 in his thesis. Table 2-2 presents these coefficients.

Table 2-2 Coefficients of interpolation (N=10)

cn	27.55	ω	0.2788
a_1	41.99	a_2	-28.61
a_3	-18.30	a_4	8.359
a_5	7.026	a_6	-2.741
a_7	-1.609	a_8	3.893
a_9	0.756	a_{10}	-2.548

2.5 Penetration of Thin AA 2024 Plate

As the dynamic response of FSW AA 2024 plate will be compared with the plate without FSW, this section reviews the penetration study of thin AA 2024 homogeneous plate at a low impact velocity (around 200 m/s).

Buyuk et al. [24] carried out experiments to simulate the impact on AA 2024-T3/T351of different thicknesses from airplane engine fragments. The ballistic limits of 1/16, 1/8 and 1/4 inch thick plate were investigated by tests. The initial impact velocity and residual velocity were recorded during the experiment. The FE analytical simulations were also performed to compare with the result of the experiment.

The ballistic limit for 1/8” thick plate is about 700 ft. /s (213.36 m/s), which is exactly the same as the impact velocity on the fuel tank access cover according to the requirement of tests in AMC 25.963(e) of CS-25.

The aim of their research was to develop finite element modelling for the aviation community to predict ballistic impact of engine fragments on airplane structures, which is similar to the objective of the current thesis.

In the experiments, the 12” × 12” square target plates procured in three different thicknesses namely 1/16”, 1/8” and 1/4” were attached to the 1” wide edge support frame, leaving a 10” ×10” target area. The 0.5” diameter impact projectile was made of 52100 chrome alloy steel.

The ballistic limits of various thicknesses of targets are shown in Figure 2-16. During the impact, the initial impact velocity reduced as the impact energy was absorbed by the target. The residual velocity is used to describe the exit velocity of the projectile after penetrating the target.

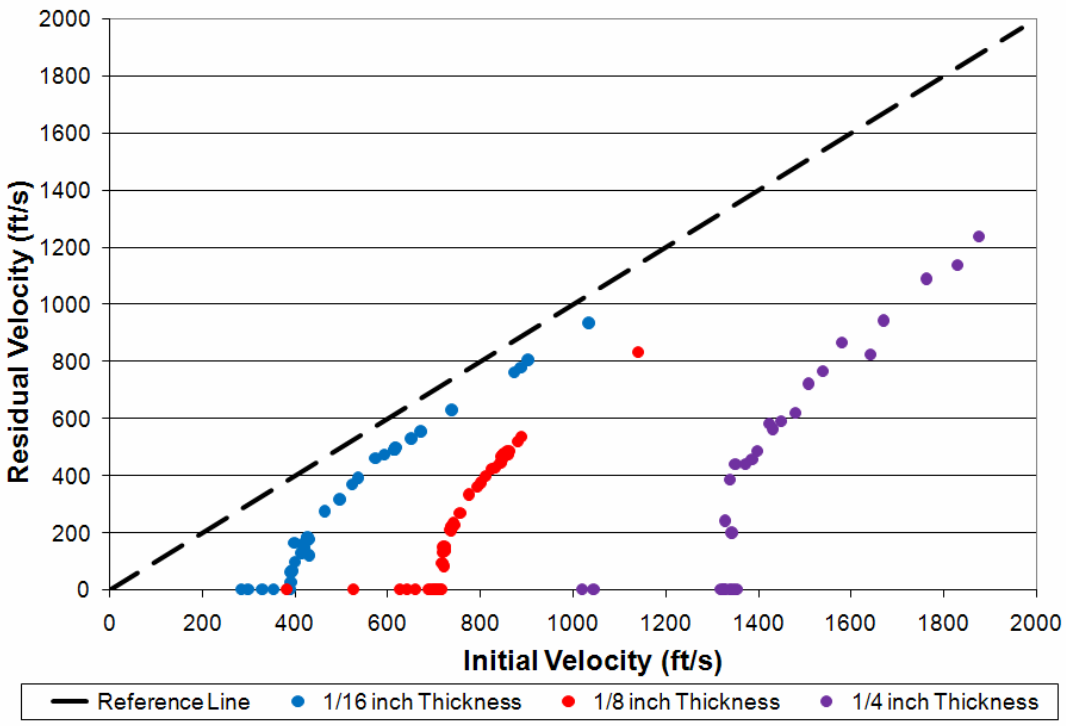

Figure 2-16 Ballistic Limits of different thickness of AA 2024-T3/T351 plate [24]

The penetration through 1/8” plate is illustrated in Figure 2-17.

Front view

Rear view

Figure 2-17 Test Result of impact on 1/8″ thick plate [24]

The material they chose for modelling engine fragments was 52100 chrome alloy steel, which will be used as the projectile material in the current research.

2.6 Requirement of AMC25.963 (e) of CS-25

Figure 2-18 illustrates the impact on the fuel tank access cover from engine debris.

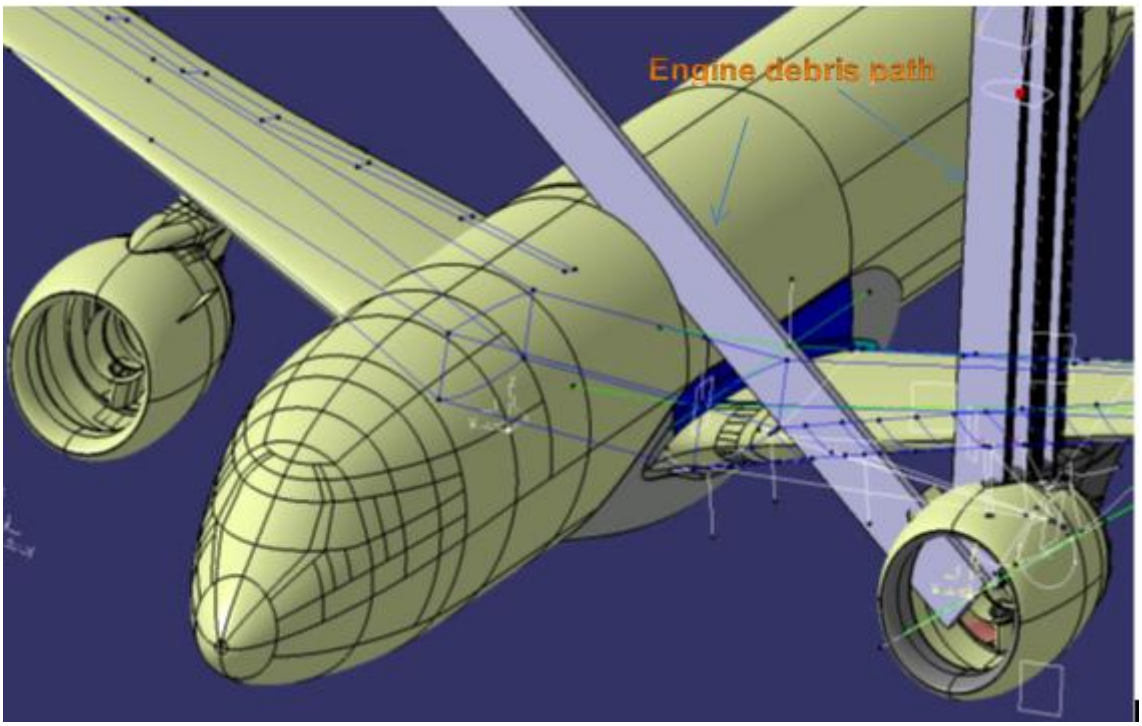

Figure 2-18 Illustration of the engine debris impact after engine failure [25]

According to Regulation AMS 25.963, the impact from engine debris is described as follows: “an energy level corresponding to the impact of a 9.5 mm (3/8 inch) cube steel debris at 213.4 m/s (700 fps), 90 degrees to the impacted surface or area should be used.” [5]

Based on the requirement above, this research will perform the simulation of a steel 9.5 mm cube-shaped projectile impact on the Aluminium 2024 FSW plate at a velocity of 213.4 m/s.

2.7 Finite Element Analysis

“The finite element method is a numerical procedure for solving a continuum mechanics problem with an accuracy acceptable to engineers” [26]. With almost

40-years devolvement of the finite element analysis (FEA) methods, various kinds of commercial FEA software have been developed.

LS-DYNA is considered to be adapted in drop or impact problem as its advantages in element type, material model and contact type [27]. In this thesis, FEA software LS-DYNA is chosen to simulate the impact.

The equation of motion can be expressed as:

$$P_n = M\ddot{u}_n + C\dot{u}_n + Ku_n \quad \text{(2-12)}$$

M is the mass; C the damping coefficient; K stiffness coefficient; u_n the displacement; $\boldsymbol{P_n}$ the force at time t_n.

LS-DYNA uses the explicit central difference scheme to integrate the equation of motion. As shown in Figure 2-19, the nonlinear problem can be dealt with by a numerical solution.

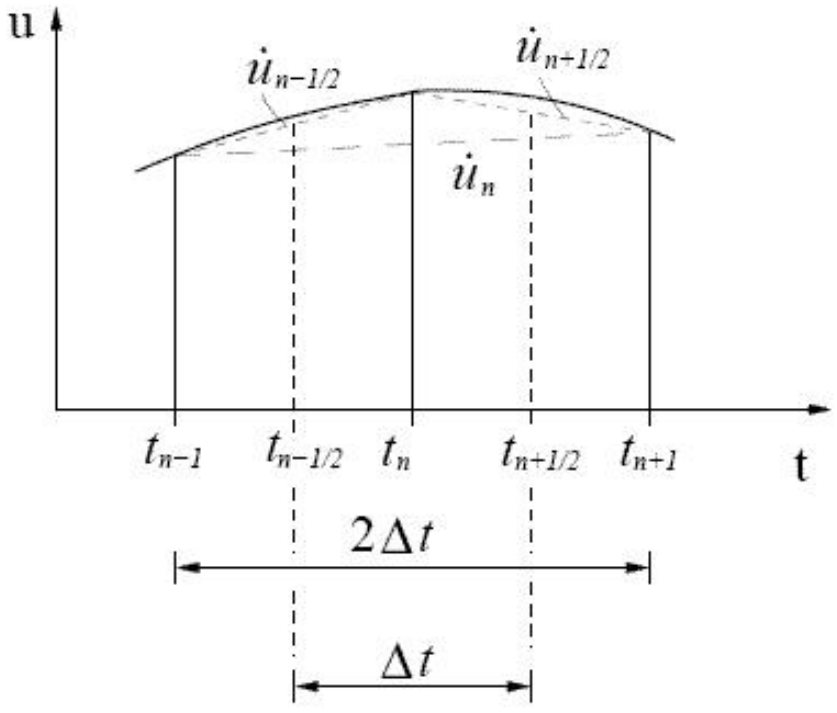

Figure 2-19 Central difference time integration [28]

Velocity:

$$\dot{u}_n = \frac{1}{2\Delta t}(u_{n+1} - u_{n-1}) \quad (2\text{-}13)$$

Acceleration:

$$\ddot{u}_n = \frac{1}{\Delta t}(\dot{u}_{n+\frac{1}{2}} - \dot{u}_{n-\frac{1}{2}}) = \frac{1}{\Delta t}(\frac{u_{n+1} - u_n}{\Delta t} - \frac{u_n - u_{n-1}}{\Delta t}) = \frac{1}{(\Delta t)^2}(u_{n+1} - 2u_n + u_{n-1}) \quad (2\text{-}14)$$

Δt is the time step.

When substituting equation (2-13) and equation (2-14) into equation (2-12), equation (2-15) can be obtained:

$$(M + \frac{1}{2}\Delta t C)u_{n+1} = \Delta t^2 P_n - (\Delta t^2 K - 2M)u_n - (M - \frac{\Delta t}{2}C)u_{n-1} \quad (2\text{-}15)$$

For lumped mass and damping the matrix M is diagonal.

$$M = \begin{bmatrix} m_1 \cdots 0 \\ \vdots \ddots \vdots \\ 0 \cdots m_n \end{bmatrix}$$

The inversion of diagonal matrix M and C is trivial.

$$M = \begin{bmatrix} \frac{1}{m_1} \cdots 0 \\ \vdots \ddots \vdots \\ 0 \cdots \frac{1}{m_n} \end{bmatrix}$$

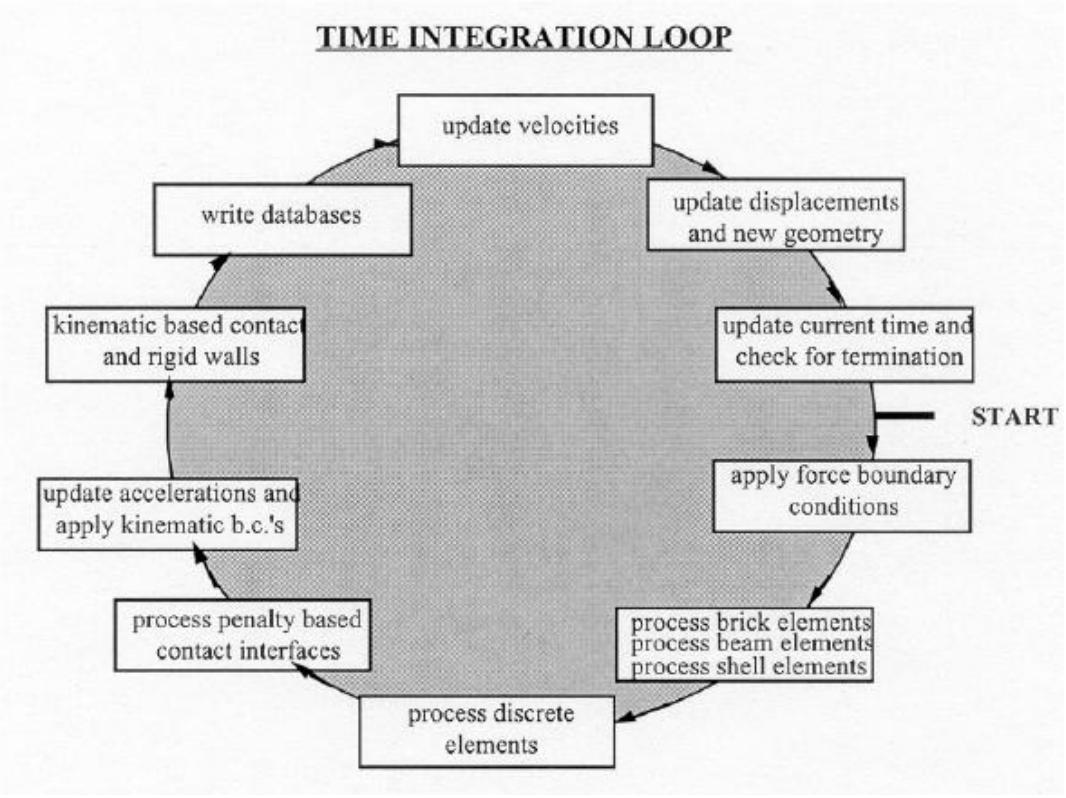

Figure 2-20 Time integration loop in LS-DYNA [29]

Figure 2-20 presents the time integration loop in LS-DYNA. At the beginning of one time circle, boundary conditions and elements are implemented, then accelerations are updated. Finally, new velocities and displacements are calculated.

The disadvantage of explicit formulation is its stability [27], which depends on the limitation of time step (Δt) that is required to avoid error accumulation in the time integration. Basically, time step limitation can be satisfied by refining the elements size and material properties.

3 Friction Stir Welds Modelling

3.1 Methodology of Friction Stir Welds Modelling

First, FSW geometry is modelled based on the microstructural zones of the welds. Second, an appropriate material model is developed to implement the mechanical properties of each zone in the FSW model. After the FE model of the FSW global tensile specimen has been built, validation will be done by comparing it with the global tensile test, as mention in Section 2.2.3.

3.2 Geometry of the FSW Joint Model

The geometry of the FSW model is built based on both the FSW plate's microstructural shape and the size of each zone. The microstructural shape and size can be obtained from microscopy pictures of the cross-section perpendicular to the welding line.

Genevois [13] has performed experiments to study the microstructure of the Aluminium Alloy 2024 FSW joint. Figure 3-1 shows the microscopy pictures of the AA 2024 FSW cross-section. "AS" is the advancing side and "RS" is the retreating side.

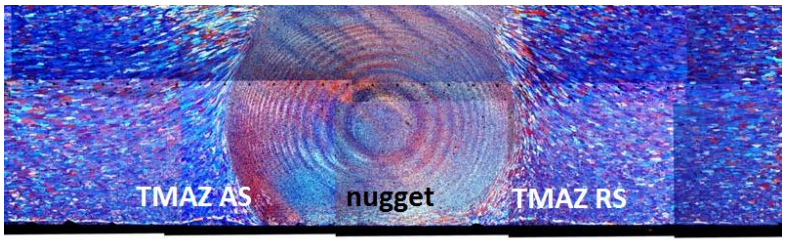

Figure 3-1 Micrograph of the AA 2024 FSW joint [13]

Genevois also gave the approximate size of each zone in the AA2024 FSW joint, as shown in Table 3-1.

Table 3-1 Size of each zone in AA 2024 friction stir welds

	HAZ	TMAZ AS	Nugget	TMAZ RS	HAZ
Dimension(mm)	14.5	2.1	6.45	3.1	13

According to the microstructural shape shown in Figure 3-1 and the dimensions of each zone (Table 3-1), the FE model of the FSW joint can be built, as shown in Figure 3-2.

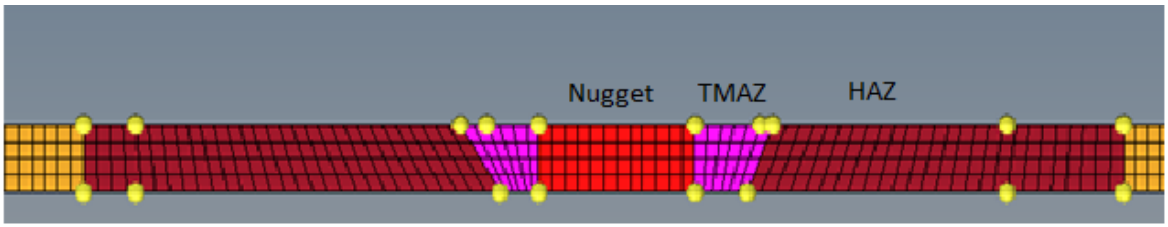

Figure 3-2 Screenshot of the FE model of the FSW joint

The size of each zone in the welds varies due to different welding parameters and welding tools (pin and shoulder). However, the size of each zone in a wide range of FSW joints is not available. Since the investigation into the relationship between the dimensions of each zone and the welding tool size has been introduced (see Section 2.1), the approximate size can be estimated according to the pin diameter and shoulder diameter, as shown in Figure 3-3. As no studies investigated the relationship between the HAZ and tool size, the size of HAZ is assumed same as that of TMAZ.

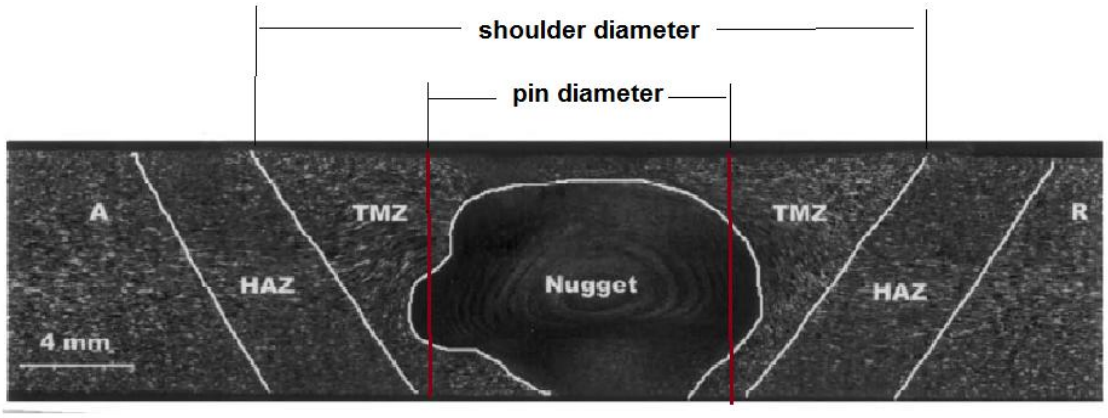

Figure 3-3 Relationship between size of each zone and tool size (picture modified based on Figure 2-1)

Thus the approximate geometry of the FSW model can be built according to the dimensions of the pin and shoulder if the microstructural shape and size of each zone obtained from the microscopy pictures are not available.

As the width of the TMAZ and HAZ zone varies through the thickness, modelling with shell elements is difficult in this research. Thus solid elements are used instead to form the FE model of the FSW plate.

3.3 Material Model of Aluminium Alloy 2024 FSW Joint

In this research a Johnson-Cook model for FSW joint is developed based on both the Johnson-Cook simplified model of FSW joints in Table 2-1 and the Johnson-Cook model of AA 2024 (shown in Table 3-2) developed by Lesuer [30].

Table 3-2 Johnson Cook model of AA 2024

Parameter	Notation	Value
Density (g/cm3)	ρ	2.77
Young's modulus (GPa)	E	73.1
Shear modulus (GPa)	G	27.5
Poison ratio	ν	0.33
Yield stress (MPa)	A	369
Strain hardening modulus (MPa)	B	684
Strain hardening exponent	n	0.73
Strain rate coefficient	C	0.0083
Thermal softening exponent	m	1.7
Room temperature (K)	T_{Room}	294
Melting temperature (K)	T_{Melt}	775
Strain rate factor (s^{-1})	EPSO	1.0
Specific heat (10E-3J/Ton-°K)	CP	875E+6
Damage parameter 1	D1	0.13
Damage parameter 2	D2	0.13
Damage parameter 3	D3	-1.5
Damage parameter 4	D4	0.011
Damage parameter 5	D5	0

The values of parameters A, B and n of each zone in the welds are derived from Table 2-1. As lack of data, the other parameters, i.e. strain rate parameter C,

damage coefficient (D_1-D_5) and thermal coefficient (M, TRoom and T_{Melt}) of each zone in the AA 2024 FSW plate will use the same value as AA 2024 Johnson-Cook model (see Table 3-2) at first stage. Later in this research, part of these values will be modified.

A new material model for each zone (the Nugget, TMAZ, HAZ and BM) of AA 2024 FSW joint can be developed, as shown in Table 3-3.

Table 3-3 Johnson-Cook model in each zone of AA 2024 FSW joint

Parameter	Notation	Value			
		BM	HAZ	TMAZ	Nugget
Density (g/cm3)	ρ	2.77			
Elastic modulus (GPa)	E	73.1			
Shear modulus (GPa)	G	27.5			
Poisson ratio	ν	0.33			
Yield stress (MPa)	A	352	326.41	139.28	248.50
Strain hardening modulus (MPa)	B	440	585.18	632.48	714.59
Strain hardening exponent	n	0.42	0.501	0.290	0.537
Strain rate coefficient	C	0.0083			
Thermal softening exponent	m	1.7			
Room temperature (K)	T_{Room}	294			
Melting temperature (K)	T_{Melt}	775			
Strain rate factor (s^{-1})	EPSO	1.0			
Specific heat (10E-3J/Ton-°K)	CP	875E+6			
Damage parameter 1	D_1	0.13			
Damage parameter 2	D_2	0.13			
Damage parameter 3	D_3	-1.5			
Damage parameter 4	D_4	0.011			
Damage parameter 5	D_5	0			

3.4 Validation of Friction Stir Welded Joint Model

3.4.1 Global Tensile Specimen Model

A FE model of a global tensile specimen is built to create validation by comparing it with the global tensile test experiment. The global tensile specimen is modelled based on the study of Genevois in Section 2.2.

The specimen measures 50 mm long in the useful area, about 6 mm wide and 2 mm thick. Although the original plates measure 6 mm thick, the specimens were machined to 2 mm thickness to obtain the deformation in the centre. The tension speed is 4 mm/min [13] (0.067 mm/s, strain rate 1.33E-3 s-1). The Johnson-Cook material model is used with the parameters shown in Table 3-3. The size of each zone is based on Table 3-1.

The FE model built by HYPERMESH is shown in Figure 3-4.

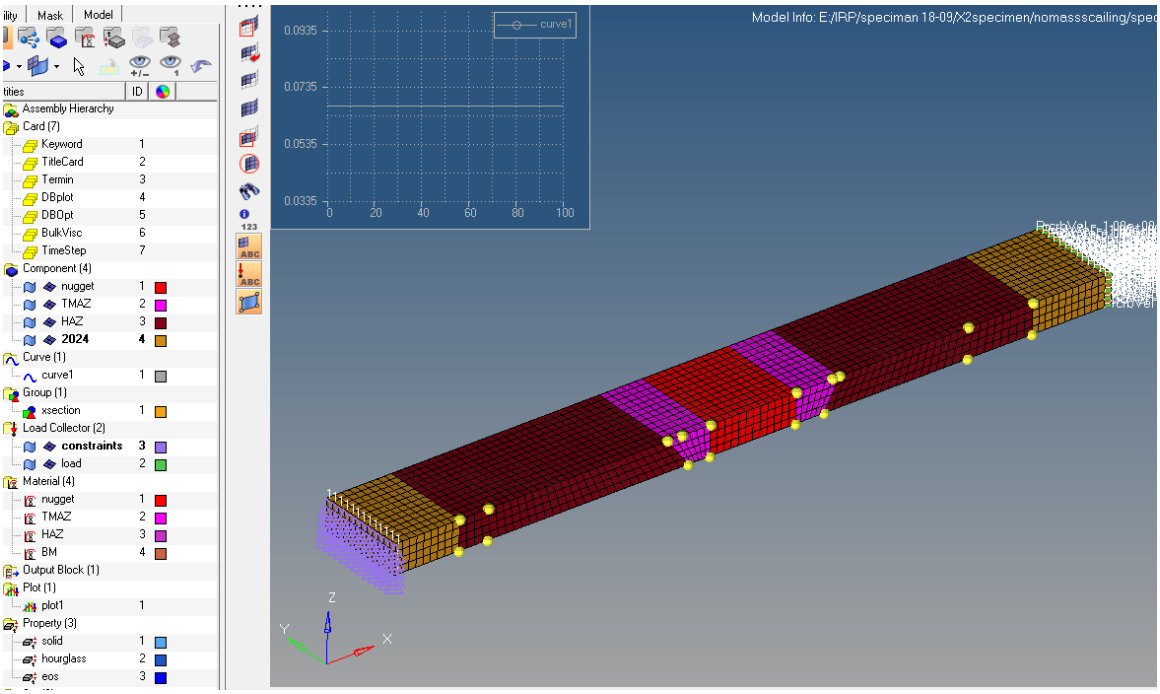

Figure 3-4 Screenshot of the global tensile test model

Table 3-4 describes the model specifics of the global tensile specimen.

Table 3-4 Model specifics of the global tensile specimen

Units		**Ton-metre-second.**
Time acquisition		Termination: 80 seconds ; DT: 0.5 second; DT2MS: -5e-5second
Dimension of specimen		50 mm high, 6 mm wide, 2 mm thick
Property of specimen		Solid property.
Material model of each zone in FSW joint		Johnson-Cook (*MAT15). Values obtained from Table 3-3
Load collector		
		Bottom layer nodes restrained in translational X (dof=1)
	Velocity	Constant 0.067 mm/s during 100 seconds
Time history		NODOUT provides x-displacement time histories SECFORC provides x-force time histories for the top row elements
Equation of state		Grüneison (*EOS4), C_0=5328000 mm/s; S1=1.338; $gama_0$=2; a=0.48. (date obtained from[24])
Hour glass		Equation: Flanagan-Belystchko stiffness form with exact volume integration for solid elements

3.4.2 First Simulation

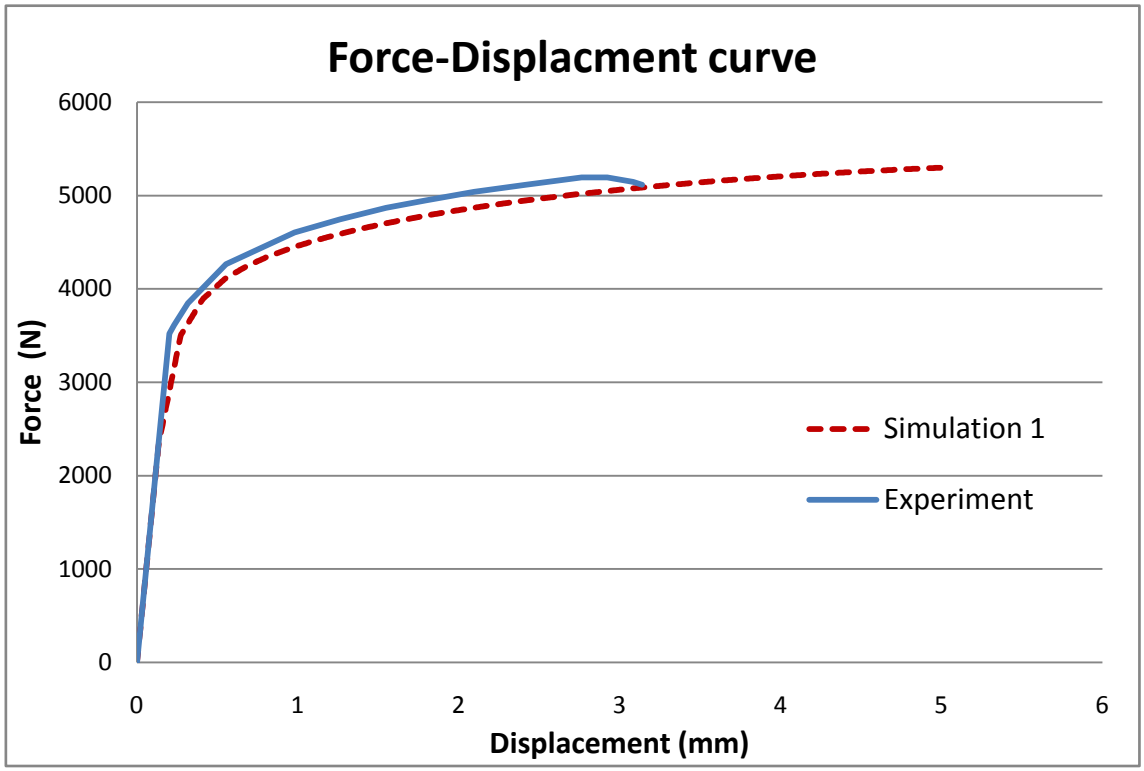

Figure 3-5 Force-displacement curves of simulation and comparison with the results of experiment

As shown in Figure 3-5, the elastic region of the simulation fits the experiment well.

However, the significant error is failure in the simulation. The failure occurs at approximately 3.1 mm in the experiment, while the simulation shows that the model fails at 5.4 mm. It is apparent that the failure in the simulation occurs much later than the tensile test.

As the effective plastic strain at failure is calculated by equation (2-6) in the Johnson-Cook model,

$$\varepsilon_p(atfailure) = [D_1 + D_2 \exp(D_3\sigma^*)](1 + D_4 \ln \dot{\varepsilon}_p)(1 + D_5 T) \quad (2\text{-}6)$$

this error is caused by the imprecise definition of the damage coefficients (D_1-D_5) in the Johnson-Cook material model of Nugget, TMAZ and HAZ.

3.4.3 New Damage Coefficients of the Johnson-Cook Model

In this section, new damage coefficients will be developed to correct the error. Assuming that the failure occurs in the Nugget and the specimen fails when the global displacement is 3.1 mm, the plastic strain ε_p at failure of Nugget can be obtained according to the simulation.

Figure 3-6 illustrates the simulation when the displacement is 3.1 mm; the plastic strain at failure of the Nugget at this moment is 0.128, as shown in Figure 3-7.

As mentioned in Section 2.2.6, the mechanical property of TMAZ is very close to that of the Nugget, the plastic strain ε_p at failure of TMAZ therefore can be assumed to be the same as that of the Nugget, which can be 0.128

Calculated via equation (2-6), the plastic strain ε_p at failure of AA 2024 base material is 0.19 when strain rate is 0.00133s^{-1}. As the material property of HAZ is stronger than TMAZ and Nugget (see Figure 2-10) and HAZ zone is the transition between BM and TMAZ zone, it can be assumed that the plastic strain ε_p at failure of HAZ can be the middle of the TMAZ (0.128) and the base material (0.19), which can be 0.155.

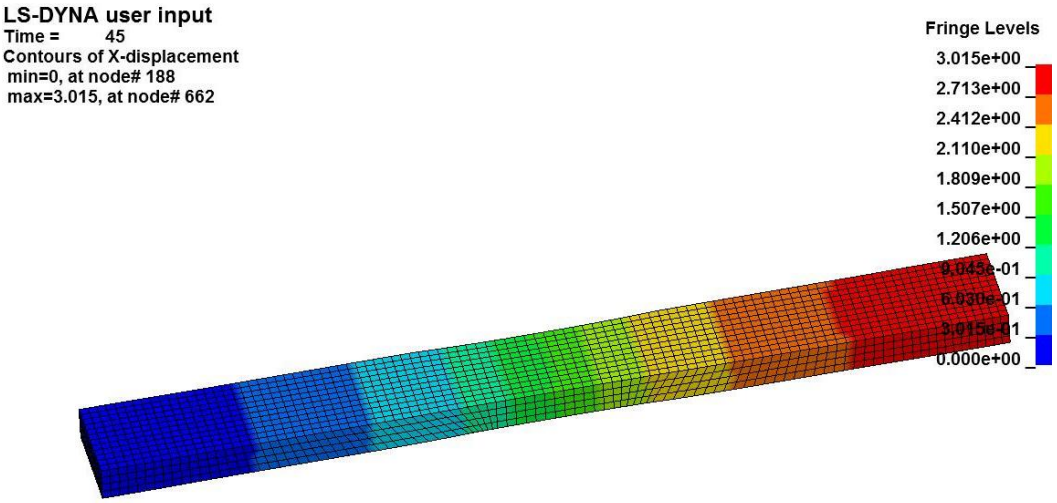

Figure 3-6 Screenshot of displacement 3.1 mm

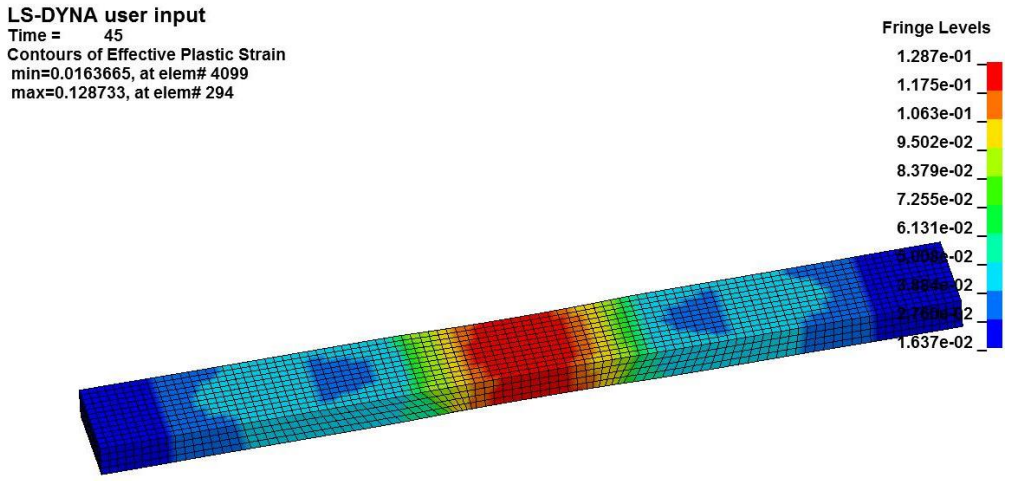

Figure 3-7 Screenshot of the plastic strain at displacement 3.1 mm

According to equation (2-6), the damage coefficient D_1-D_5 can be calculated based on the plastic strain ε_p at failure.

In tension test the temperature rise is so low that the thermal effect can be ignored. Thus coefficient D_5 of each zone will remain at 0. As lack of various strain rates tensile tests, D_4 will also remain the same (0.011).

Thus the plastic strain at failure can be expressed as:

$$\varepsilon_p at failure = [D_1 + D_2 \exp(D_3 \sigma^*)](1 + 0.011 \ln \dot{\varepsilon}_p)(1 + 0 \times T) \quad (3\text{-}1)$$

where $(1 + 0.011 ln\dot{\varepsilon_p})(1 + 0 \times T)$ is constant. D_1, D_2 and D_3 can be determined from several plastic strains at failure with different triaxialities. However, due to the lack of data, D_1, D_2 and D_3 cannot be defined accurately.

As shown in equation (3-1), the strain at failure is most sensitive to D_1, only D_1 will be modified to satisfy the real strain at failure, while D_2 and D_3 will remain unchanged.

Before determining the damage coefficient D_1, the triaxiality σ^* of the tensile specimen needs to be calculated. σ^* can be calculated as:

$$\sigma_* = \frac{\sigma_m}{\sigma_{ep}} \quad (3\text{-}2)$$

The mean stress can be calculated as:

$$\sigma_m = \frac{1}{3}(\sigma_1 + \sigma_2 + \sigma_3) \quad (3\text{-}3)$$

In tensile tests, the stress can be the uniaxle stress in the x vector.

$$\sigma_{ep} = \begin{bmatrix} \sigma_x & 0 & 0 \\ 0 & 0 & 0 \\ 0 & 0 & 0 \end{bmatrix}$$

As there is no stress in the other axles in tensile tests, σ_m will be 1/3 σ_{ep}. Therefore, σ^* of the tensile specimen is 0.333 (1/3).

D_2 is 0.13, D_3 is -1.5, D_4 is 0.011, D_5 is 0 and strain rate $\dot{\varepsilon_p}$ is 0.00133s^{-1}.Then equation (2-6) can be written as:

$$\varepsilon_p at failure = [D_1 + 0.13\exp(-1.5 \times 0.333)](1 + 0.011 \times \ln 0.00133) \quad (3\text{-}3)$$

The strain rate is 0.00133s^{-1}, ε_p the plastic strain at failure of the Nugget, TMAZ and HAZ are 0.128, 0.128 and 0.155 respectively. A new damage coefficient D_1 of each zone can be determined via equation (3-3).

The new values of damage coefficients are shown in Table 3-5.

Table 3-5 Modified damage coefficients of each zone

	Nugget	**TMAZ**	**HAZ**	**BM**
$\boldsymbol{D_1}$	0.059	0.059	0.087	0.13
$\boldsymbol{D_2}$	0.13	0.13	0.13	0.13
$\boldsymbol{D_3}$	-1.5	-1.5	-1.5	-1.5
$\boldsymbol{D_4}$	0.011	0.011	0.011	0.011
$\boldsymbol{D_5}$	0	0	0	0

3.4.4 Second Simulation

A new tensile FE model for static tension load with a modified damage coefficient has been built. Figure 3-8 illustrates the force-displacement curve of the second simulation and the comparison with the results of the global tensile test.

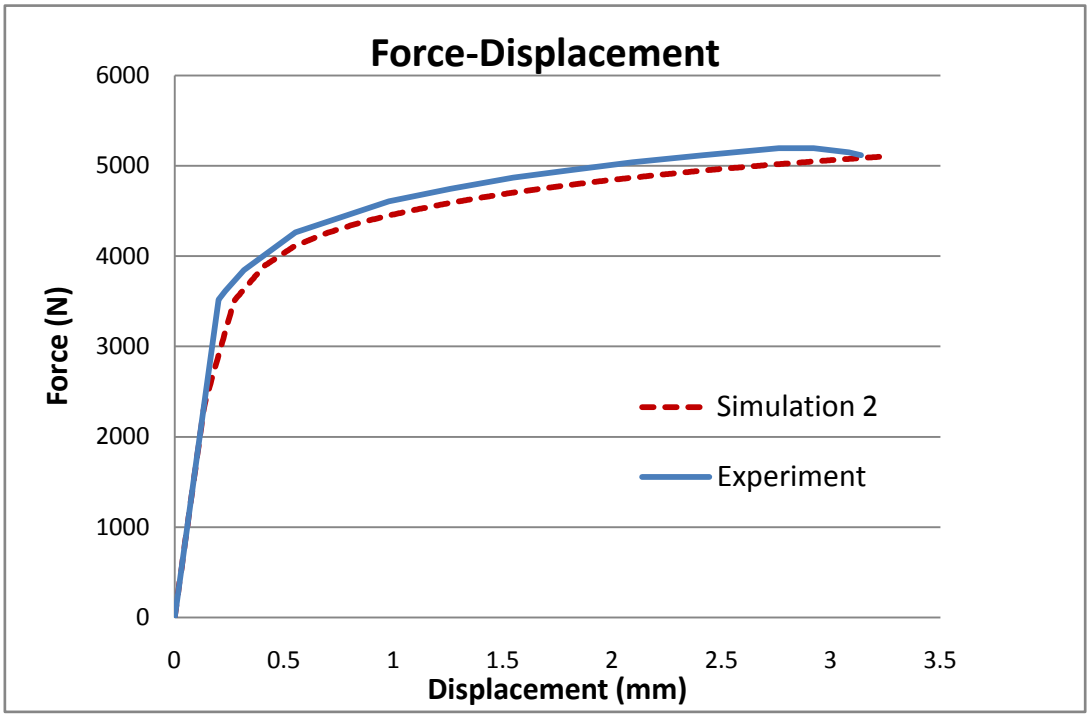

Figure 3-8 Force-displacement curves of second simulation and comparison with the experiment

3.4.5 Material Model Conclusion

The failure of the second simulation occurs approximately at the same point as the experiment and the simulation in the elastic region is well modelled.

There is a small divergence in the plastic region. This is because the A, B and n are determined when setting the strain rate coefficient C to zero due to the lack of several strain rates local tensile tests. The values of A, B and n should be slightly inaccurate. However, as lack of data, this slight divergence has to be neglected in this research. Further experimental research can be carried out to obtain more accurate values of A, B, n and C.

The final material model (Johnson-Cook Model) of each zone of the FSW joint is shown in Table 3-6.

Table 3-6 Final material model of FSW zones

Parameter	Notation	Value			
		BM	HAZ	TMAZ	Nugget
Density (g/cm3)	ρ	2.77e-9			
Young's modulus (GPa)	E	73.1			
Shear modulus (GPa)	G	27.5			
Poisson ratio	ν	0.33			
Yield stress (MPa)	A	352	326.41	139.28	248.5
Strain hardening modulus (MPa)	B	440	585.18	632.48	714.59
Strain hardening exponent	n	0.42	0.501	0.290	0.537
Strain rate coefficient	C	0.0083	0.0083	0.0083	0.0083
Thermal softening exponent	m	1.7			
Room temperature (K)	T_{Room}	294			
Melting temperature (K)	T_{Melt}	775			
Strain rate factor (s^{-1})	EPSO	1.0			
Specific heat (10E-3J/Ton-°K)	CP	875E+6			
Damage parameter 1	D_1	0.13	0.087	0.059	0.059
Damage parameter 2	D_2	0.13			
Damage parameter 3	D_3	-1.5			
Damage parameter 4	D_4	0.011			
Damage parameter 5	D_5	0			

4 Numerical Study of Penetration on AA 2024 Plate

The AA 2024 FSW plate in the final model needs to be compared with a model without an FSW joint. In addition, the minimum thickness of the skin panel which can withstand the impact from engine debris according to the AMS 25.963 has not been determined. Thus, in this chapter models will be built to simulate the impact on a homogeneous AA 2024 plate from engine debris.

On the other hand, mesh quality plays a significant role in finite element (FE) analysis. Plate models of the AA 2024 plate with and without an FSW joint require refinement to avoid the influence of mesh quality. The refinement can be done by reducing the mesh size.

The way to determine the proper mesh size can be: first, perform simulations of penetrations of plate with various impact velocities; second, compare the residual velocities after penetration with the experimental results.

The proper mesh size for AA 2024 homogeneous plate can be determined, as experimental studies of penetration on AA 2024 homogeneous plate are available. However, as lack of similar experiments on AA 2024 FSW plate, it has to be assumed that the proper mesh density for AA 2024 homogenous plate would be fine for AA 2024 FSW plate model.

4.1 Simulation of Impact on AA 2024 Plate

Based on the experimental study of the impact on the 1/8” target plate operated by Buyuk et al. [24] (see Section 2.5), the impact on AA 2024 plate will be simulated.

The projectile is 1/4” radius sphere steel projectile (52100 chrome alloy steel). The target is 10” × 10”, 1/8” thick AA 2024 plate. The validation can be made by comparison with the experiment results.

4.1.1 Mesh Size

The initial impact velocities for modelling are 213, 220, 225, 230, 240 and 260 m/s. The three different models of the target vary in mesh size. The mesh was refined from element size 0.8 mm to 0.6 mm and 0.4 mm in order to see the element size effect on simulations, as shown in Table 4-1.

The mesh size of the target model at the impact area is shown in Table 4-1.

Table 4-1 Three different mesh size of the target model

Mesh Size	Mesh Shape	Number of Elements Through the Thickness	Element size (mm)
1	Cubic brick	4	0.8
2	Cubic brick	6	0.6
3	Cubic brick	8	0.4

The mesh size 2 is shown in Figure 4-1.

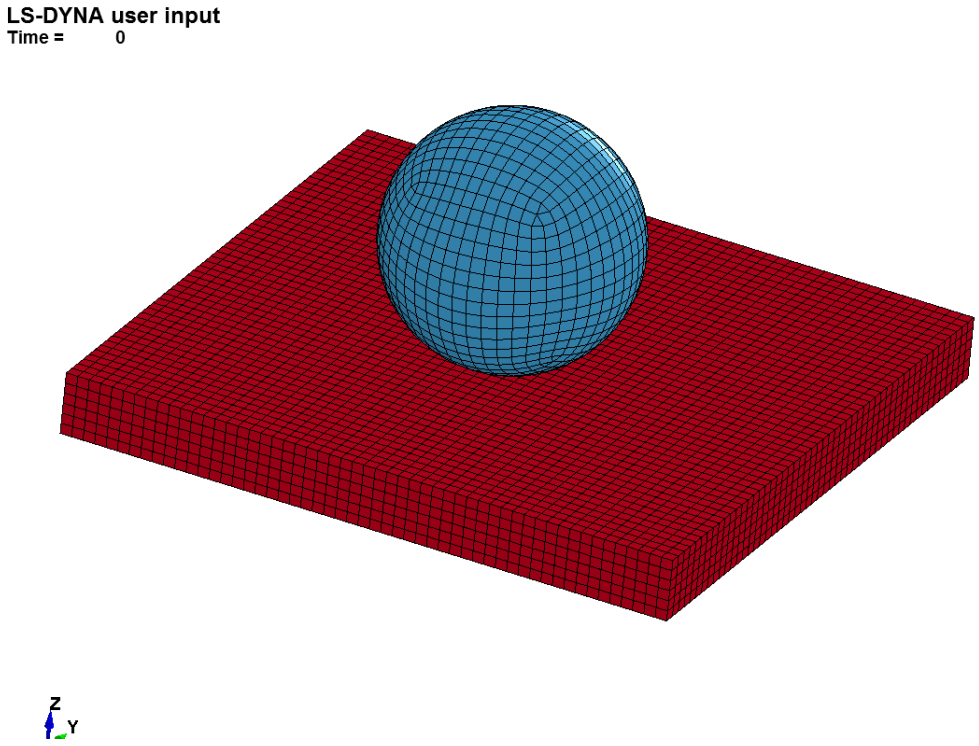

Figure 4-1 Screen shot of mesh size 2 (6 elements through the thickness)

4.1.2 Material Model

The material model for the steel projectile (52100 chrome alloy steel) is plastic kinematic hardening model (*MAT_3_PLASTIC_KINEMATIC).

The yield stress can be calculated as:

$$\sigma_Y = [1 + (\frac{\dot{\varepsilon}}{C})^{\frac{1}{P}}]\sigma_0 \quad (4\text{-}1)$$

Where σ_0 is the initial yield stress; $\dot{\varepsilon}$ is the strain rate; C and P are Cowper-Symonds strain rate coefficient.

As the experiments showed that there is no sign of yielding or failure in the projectile [24], the failure strain is set to zero. The strain rate coefficients C and P are also zero since the strain rate is not considered.

The parameters of the plastic kinematic model for 52100 chrome alloy steel obtained from [31] are shown in Table 4-2.

Table 4-2 Parameters of the plastic kinematic model for 52100 chrome alloy steel

Density	Elastic modulus	Poisson ratio	Yield stress	Tangent modulus	Strain rate coefficient	Failure strain
7.74 g/cm^3	206 GPa	0.33	470 MPa	0	C=0 P=0	0

The parameters in Table 3-2 (the Johnson-Cook model for AA 2024) are used for the target plate model.

4.1.3 Impact Model Description

The specifics of the impact model are shown in Table 4-3.

Table 4-3 Impact model description

Units	**Tons-millimetres-seconds**	
Termination	0.0003s	
Dimensions	Plate	10” (250 mm) long, 10” (250 mm) wide,1/8” thick
	Projectile	1/4"(6.35 mm) radius sphere
Load factors	Constraints	Edge Layers nodes of the plate are fully restrained
	Initial velocities	All nodes of projectile translate in Z-direction with various velocities (which are 213, 220, 225, 230, 240 and 260 m/s.)
Contact	Contact type	*CONTACT_ERODING_SURFACE_TO_SURFACE”
	Contact card	Static and dynamic coefficient of friction (FS) is 0.5 between aluminium target and steel projectile; EROSOP and IADJ is active
Material model		
	Plate	Johnson-Cook model (*MAT_15) (see Table 3-2)
	Projectile	Plastic kinematic model (*MAT_3) (see Table 4-2)
Section model		
	Solid section	Both plate and projectile
	Equation of state	Grüneison (*EOS4) for plate, C_0=5328000 mm/s; S1=1.338; gama$_0$=2; a=0.48. (date obtained from[24]) Applied to plate elements
	Hourglass	Equation: Flanagan-Belystchko stiffness form with exact volume integration for solid elements applied to both projectile and plate
Sets	Gauge nodes	3 different nodes on the surface of the projectile; used for OUTPUT_BLOCK “Velocities-time”

4.1.4 Simulations and Results

The penetration simulation of mesh size 2 is shown in Figure 4-2. The main impact area is cut to show the result more clearly.

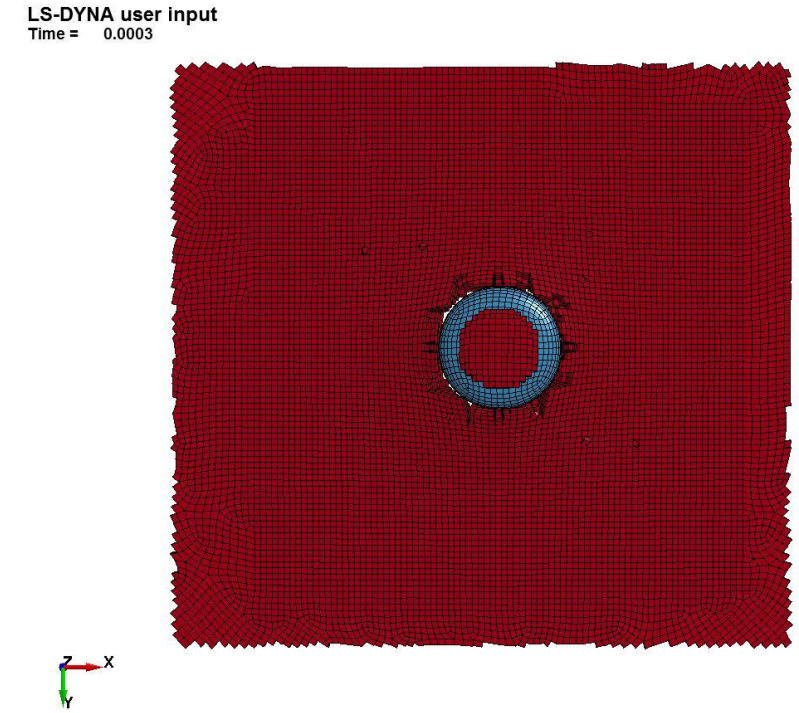

(a) View from bottom

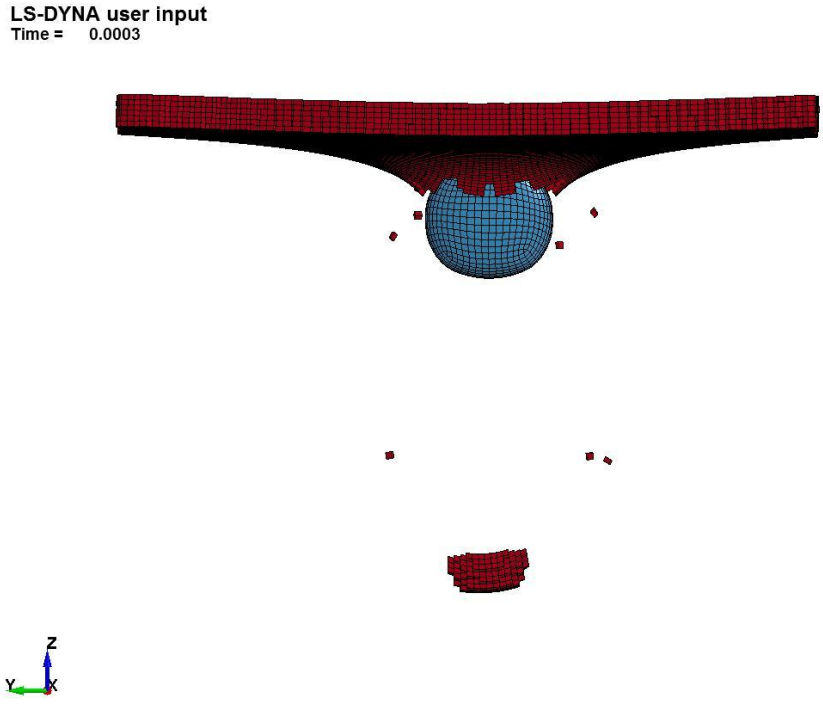

(b) Side view

Figure 4-2 Penetration simulation of mesh size 2

As shown in Table 4-4, the ballistic limits of different models vary in their initial impact velocities.

Table 4-4 Predicting residual velocities of different mesh size

Mesh size 1 (4 elements through thickness)		Mesh size 2 (6 elements through thickness)		Mesh size 3 (8 elements through thickness)		Tests	
Initial velocity m/s	Residual velocity m/s	Initial velocity m/s	Residual velocity m/s	Initial velocity m/s	Residual velocity m/s	Initial velocity m/s	Residual velocity m/s
213	0	213	0	213	45	213	0
220	0	220	37	220	74	220	47
225	0	225	69	225	87	225	72
230	42	230	80	230	97	230	82
240	89	240	107	240	116	240	108
260	133	260	141	260	151	260	141

The comparison between the result of experiments and the simulations are shown in Figure 4-3.

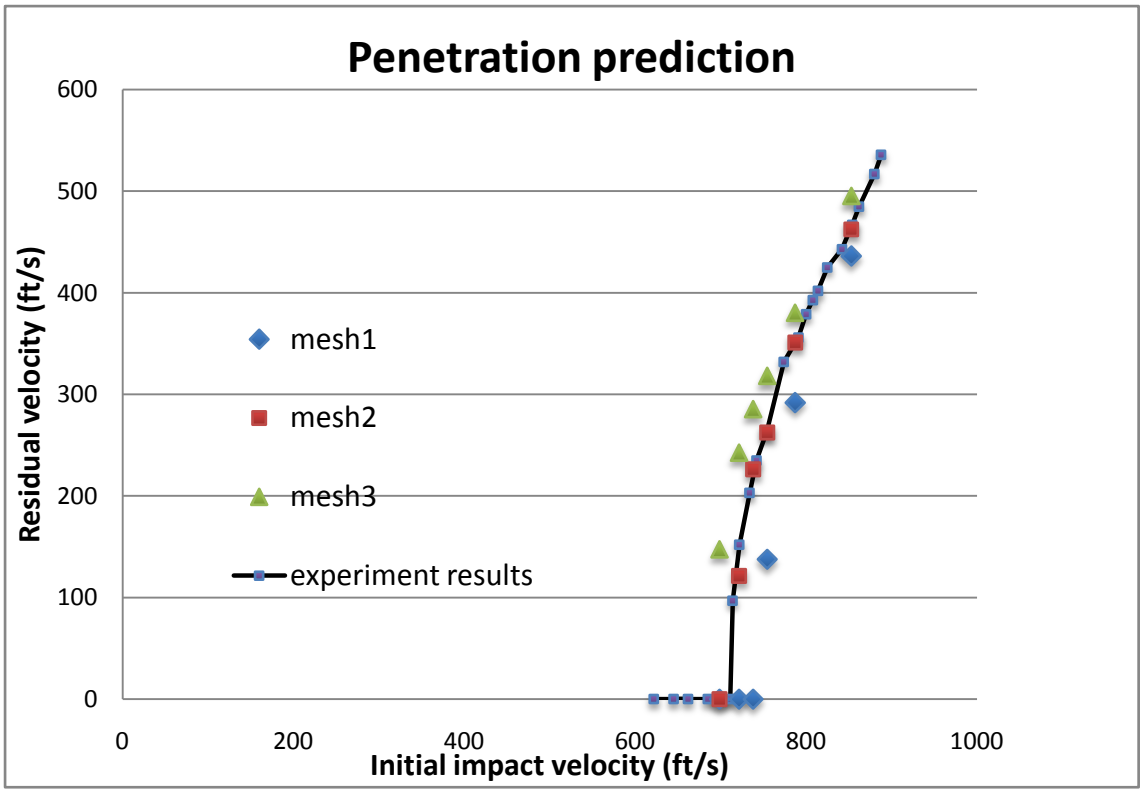

Figure 4-3 Ballistic limits prediction of different mesh size

As shown in Figure 4-3 and Table 4-4, it can be concluded that mesh size influences the ballistic limits significantly: the smaller the mesh, the lower the initial velocity of the ballistic limits. In model of the mesh size 1 (4 elements through thickness) the penetration occurs at 230 m/s, which is higher than the experimental result (about 213 m/s), whereas the models of the mesh size 2 and the mesh size 3 agree better with the test results. Their ballistic limits are 220 and 213 m/s respectively.

When refining the mesh size, the simulation would be more accurate, which means the results of the model of the mesh size 3 would be closer to the tests. However, in this series of simulations, the model of the mesh size 2 agreed better than that of mesh size 3. This is because the Johnson-Cook material model developed by Lesuer [30] is weaker than the real AA 2024 material. As shown in Figure 4-4, the predicted failure in tension occurs at a strain of 0.23, whereas in the experimental data the strain at failure is 0.30 (obtained from [30]), which indicates that the real AA 2024 material is stronger than the Johnson-Cook material model.

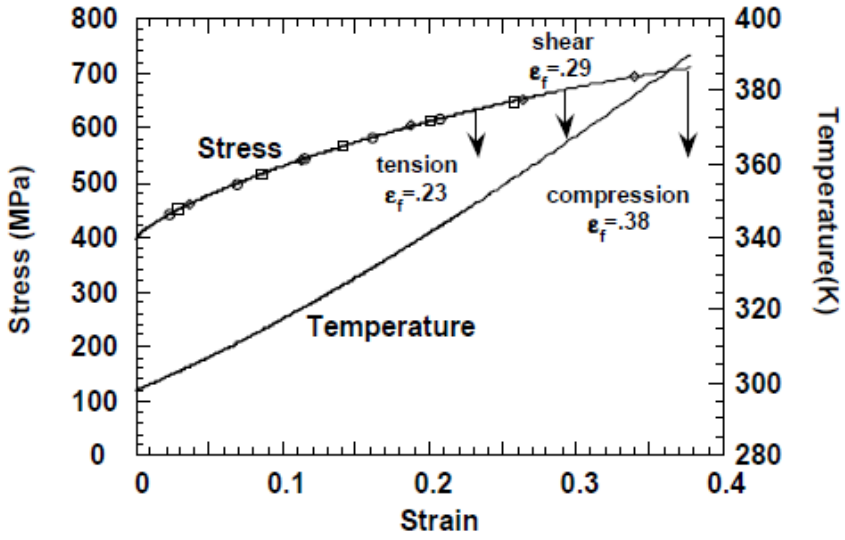

Figure 4-4 Predicted Stress-Strain curve using data from research of Lesuer [30]

On the other hand, the model of the smaller mesh results in more elements and the simulation costs much more computational time. Therefore, as an

appropriate compromise with reasonable accuracy and computational cost, mesh size 2 (6 elements though thickness, 0.6 mm/element) will be applied to both plate models with and without FSW joints.

4.2 Impact on Aluminium Alloy 2024 Plate from Engine Debris

According to AMS 25.963, the 1/4” radius sphere projectile of the impact model, above in Section 4.1, is modified to a steel 9.5 mm cube-shaped projectile. In this section, the impact velocity remains same, which is 213.4 m/s; the area of the plate is also the same as the impact models above, which is 10”× 10”. Only the thickness of the AA 2024 plate varies.

The thickness is 2.4 mm in first model. The impact simulation is shown in Figure 4-5. The plate is penetrated and the residual velocity of the projectile is around 90 m/s. Obviously the 2.4 mm thick AA 2024 plate cannot satisfy the requirement according to AMS 25.963.

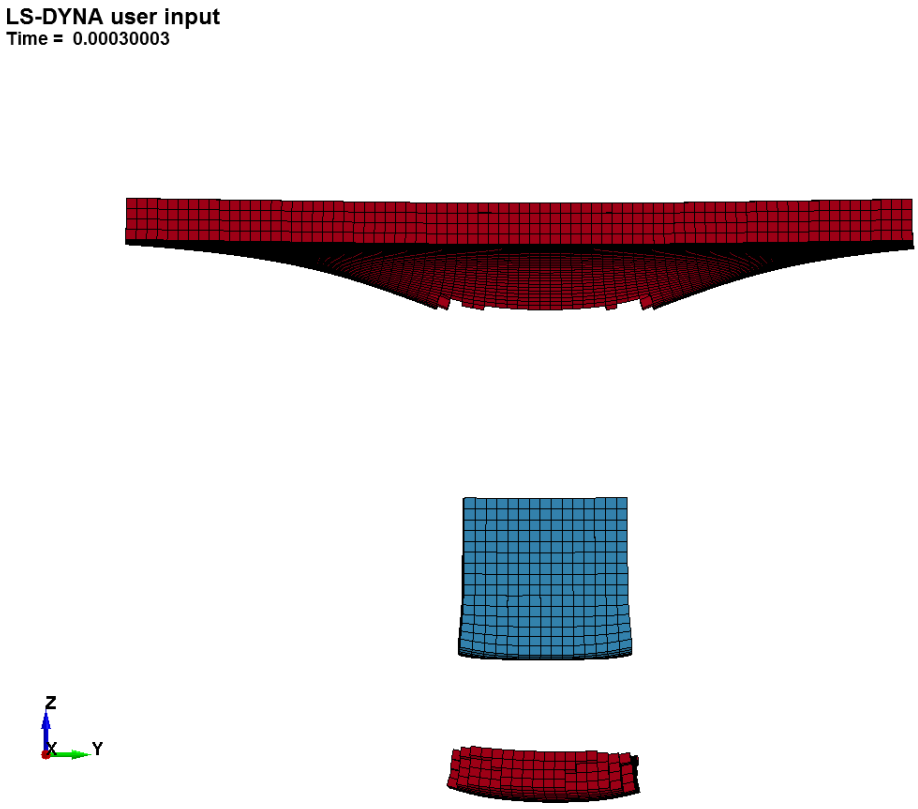

Figure 4-5 Cube projectile impact on 2.4 mm AA 2024 plate

In the second model, a layer element (size 0.6 mm) is added to the plate. The thickness is increased up to 3.0 mm. The prediction shown in Figure 4-6 indicates that although the elements of the plate around the impact area experienced a large deformation, no element has failed. Thus penetration has not occurred.

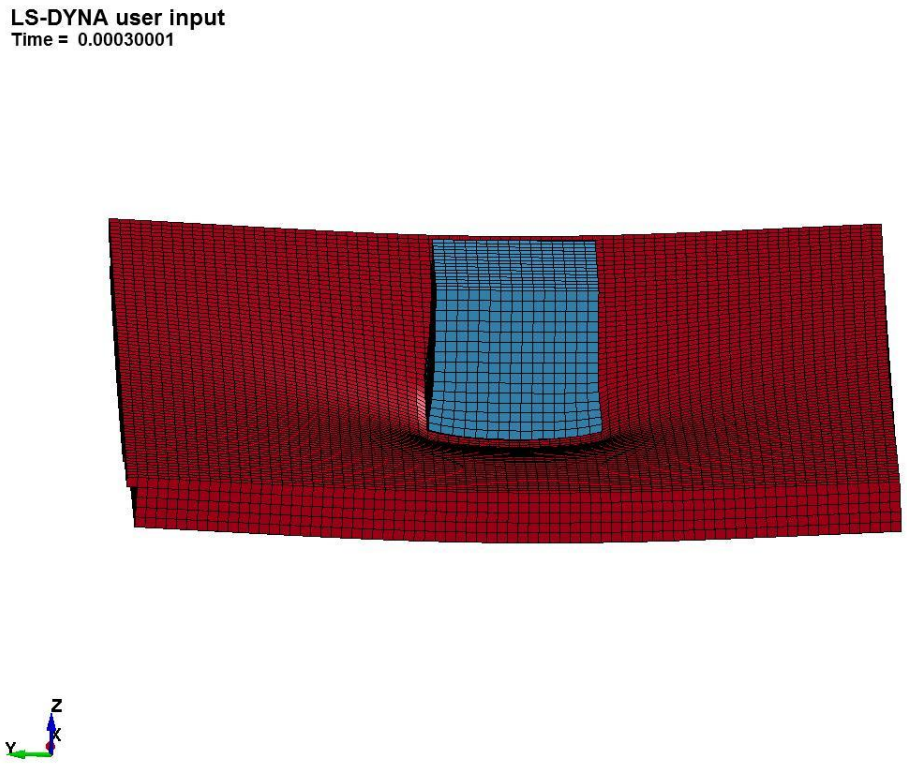

Figure 4-6 Cube projectile impact on 3.0 mm AA 2024 plate

Therefore, 3 mm thick AA 2024 plate withstands the impact and the minimum thickness of the target plate in the final impact model will be 3 mm.

5 Final Models of Impact on FSW Plate

The minimum thickness has been determined; the material model of each zone in the Aluminium Alloy 2024 FSW plate has been developed and the mesh density of the target plate has been determined. Then the final impact model of the FSW plate can be built.

The material model of the FSW plate is the Johnson-Cook model (obtained from Table 3-6). The material of the steel cube-shaped projectile is 52100 chrome alloy steel. The plastic kinematic hardening model is used for this steel (see Table 4-2). The mesh density in the centre of the impact area is 0.6 mm.

The dimensions of the target plate are 250 mm × 250 mm. The thickness of the FSW plate is 3.0 mm; the size of the cubic projectile is 9.5 mm.

5.1 Geometry of a 3 mm Aluminium Alloy 2024 FSW Plate Model

As mentioned in Section 4.1, the geometry of the FSW model can be built according to the dimensions of the pin and shoulder. The welding tool chosen for the 3 mm thick plate could be a 4 mm diameter pin with a 12 mm diameter shoulder (see Figure 2-13). The geometry of the 3 mm thick AA 2024 FSW joint model can be built, as shown in Figure 5-1 and Figure 5-2.

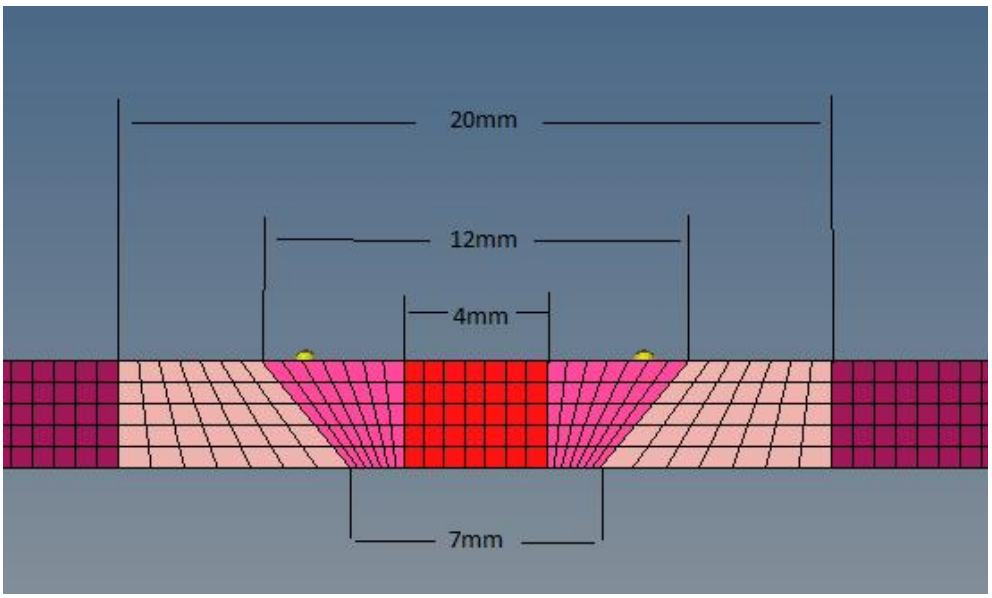

Figure 5-1 Geometry of an AA 2024 FSW plate model (3.0 mm thick)

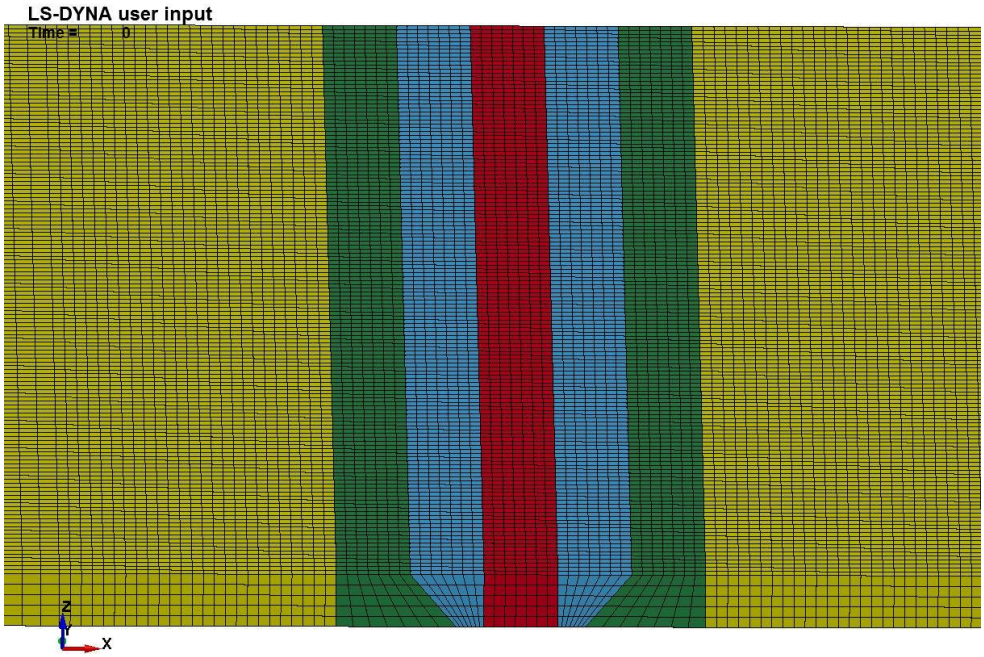

Figure 5-2 3D view of the plate model with FSW geometry

5.2 AA 2024 Homogeneous Plate Model with FSW Geometry

An FE model of a 3 mm thick AA 2024 plate is built with the FSW geometry, as shown in Figure 5-3. Only the AA 2024 material model is implemented in the plate model. This impact simulation will be compared with the FE model of the AA 2024 plate without FSW geometry in Section 5.2 to check if the different geometry of plate models will affect the simulation.

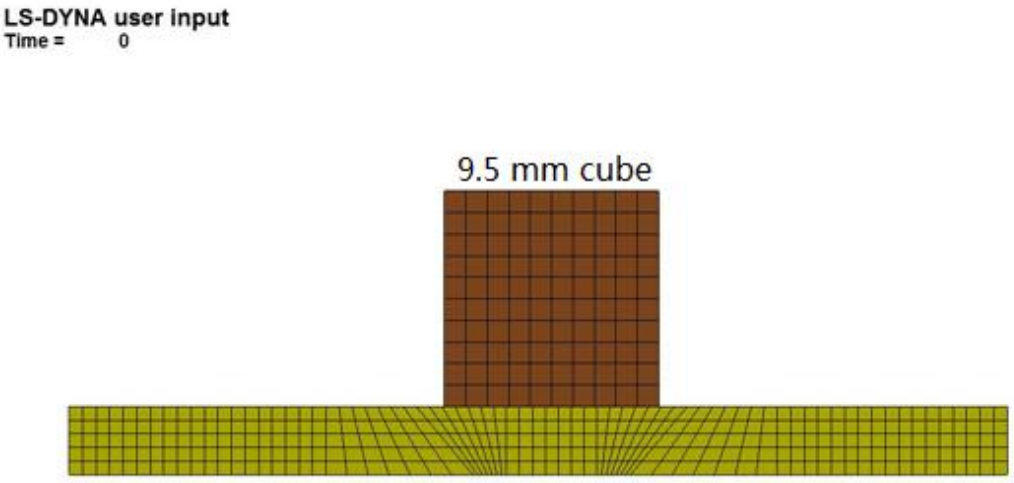

Figure 5-3 AA 2024 plate model with FSW Geometry

The mesh density in the impact area is 0.6 mm, which is same as the model in Section 5.2. The only difference is the FSW joint geometry.

Figure 5-4 shows the result of these two simulations. No penetration occurred in either simulation.

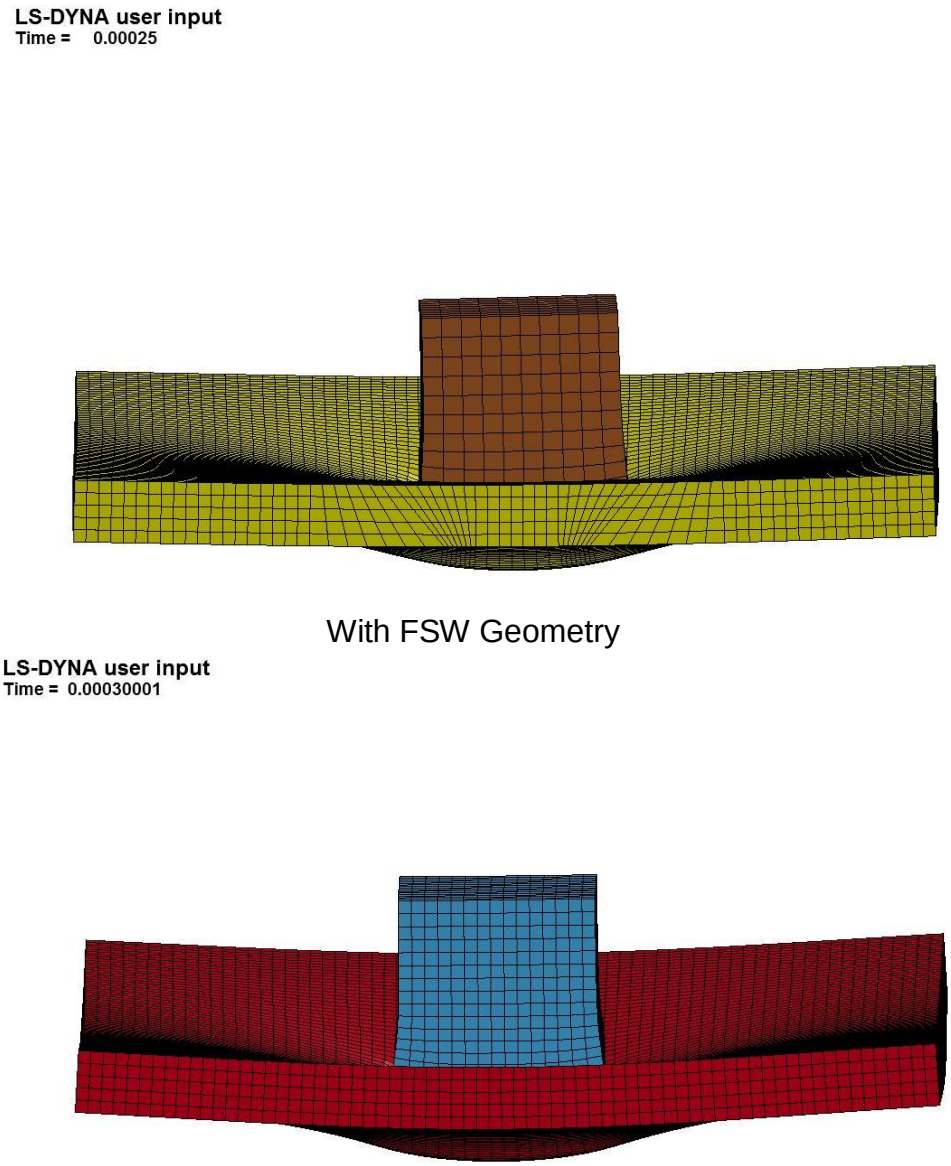

With FSW Geometry

Without FSW Geometry

Figure 5-4 Simulations of impact on 3 mm thick AA 2024 plate

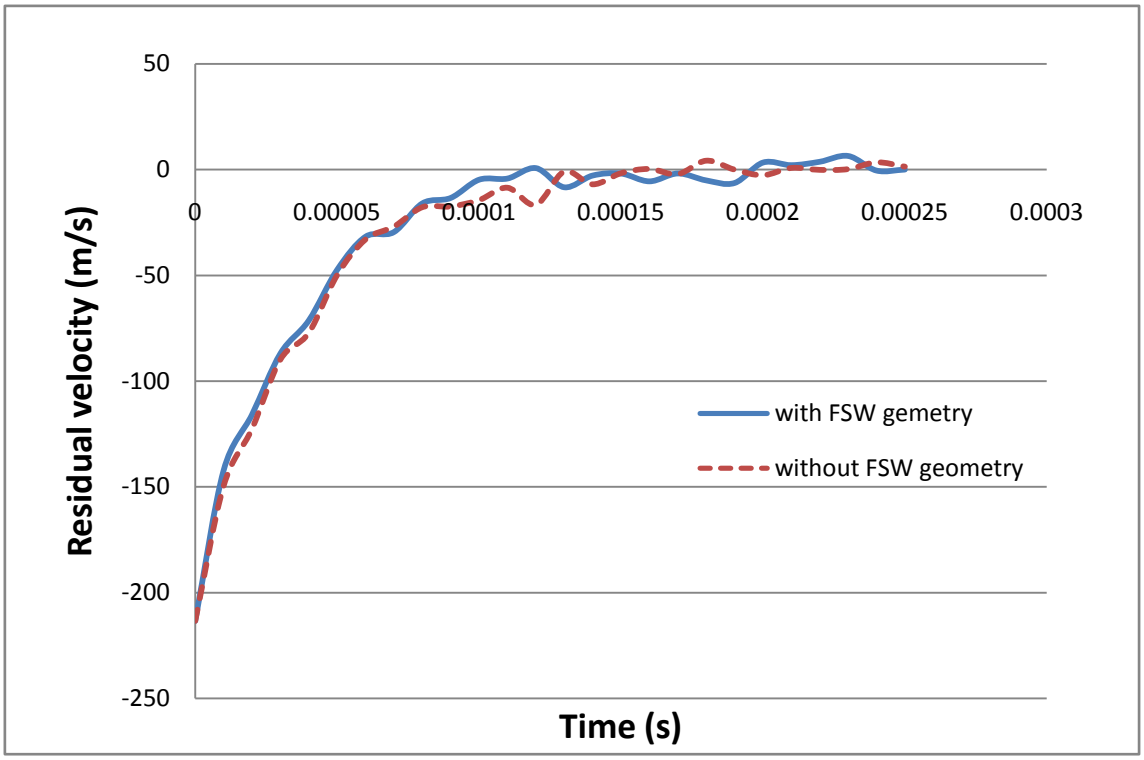

Figure 5-5 Residual velocities of the impact simulations with and without FSW geometry

As shown in Figure 5-5, the residual velocity curves of these two simulations are very close and at 0.00025s the residual velocities are approximately the same.

In the model with FSW geometry only two elements of the plate failed, while in the model without FSW geometry no element failed.

It can be concluded that the influence of FSW geometry on the impact simulation is so small that it can be ignored. As in the impact model without FSW geometry the material model and mesh density have already been validated with the experiments in Chapter 5, the impact model with FSW geometry would be fine for further simulations.

5.3 Simulation of Impact on 3.0 mm FSW Plate

In this section, the impact model with both FSW geometry and FSW material model is built. The description of the 3.0 mm thick plate model is presented in Table 5-1.

Table 5-1 Description of 3.0 mm thick plate model

Units	**Tons-millimetres-seconds**	
Termination	0.00025s	
Dimensions	Plate	250 mm long, 250 mm wide, 3 mm thick
	Projectile	9.5 mm cube-shaped projectile
Load factors	Constraints	Edge Layers nodes of the plate are fully restrained
	Initial velocities	All nodes of projectile translate in Z-direction with 2134000 mm/s
Contact (Projectile and plate)	Contact type	*CONTACT_ERODING_SURFACE_TO_SURFACE"
	Contact card	Static and dynamic coefficient of friction (FS) is 0.5 between aluminium target and steel projectile; EROSOP and IADJ is active
Contact between each zone	Contact type	*CONTACT_ERODING_SINGLE _SURFACE"
	Contact card	EROSOP and IADJ is active
Material model	Plate	Johnson cook model (*MAT_15) Nugget, TMAZ,HAZ,BM (see Table 3-6)
	Projectile	plastic kinematic model (*MAT_3) (see Table 4-2)
Section model	Solid section	Both plate and projectile
	Equation of state	Grüneison (*EOS4) for plate, C_0=5328000 mm/s; S1=1.338; gama$_0$=2; a=0.48. (data obtained from[24]) applied to plate elements
	Hourglass	Equation: Flanagan-Belystchko stiffness form with exact volume integration for solid elements applied to both projectile and plate

5.4 Impact Model with Longitudinal Residual Stress

In this section, the longitudinal residual stress will be implemented in the Aluminium Alloy 2024 FSW plate. As the experimental data of the longitudinal residual stress in the 3 mm thick AA 2024 FSW plate is not available, the longitudinal residual stress of 3 mm thick AA 7075 FSW plate will be used instead.

$$f(x) = cn + \sum_{n=1}^{N} a_n \cos(n\omega x) \quad (2\text{-}11)$$

Equation (2-11) is used to develop a Matlab programming (see Appendix A) to calculate the longitudinal residual stress according to x direction nodal value for each plate element. The coefficients of cnt, a_n and ω are obtained from Table 2-2. After the stress of all the elements has been calculated, it can be implemented in LS-DYNA input file.

Figure 5-6 shows the longitudinal residual stress implemented in the plate model.

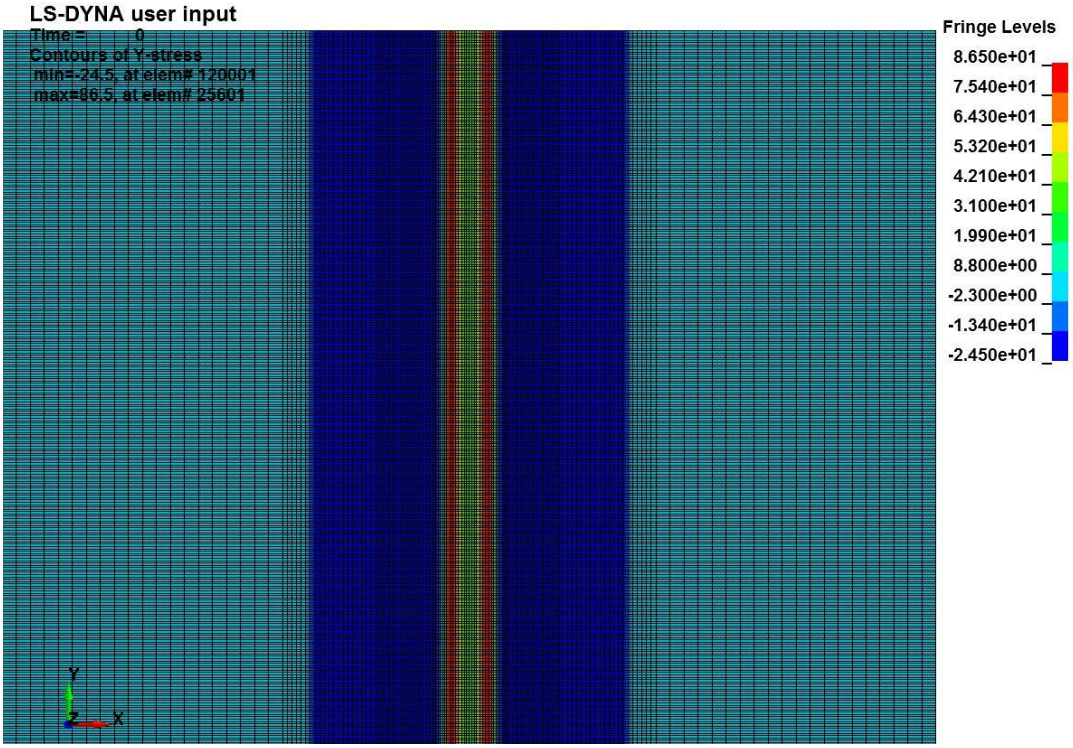

Figure 5-6 Longitudinal residual stress implemented in plate model (Unit: Mpa)

After the longitudinal residual stress has been implemented in the FSW plate model, the impact on the centre of the welds (Nugget) is simulated.

The comparisons are shown in Figure 5-7, Figure 5-8, Figure 5-9 and Table 5-2 to analyse the effects of the longitudinal residual stress. The main impact area is cut to show the result more clearly.

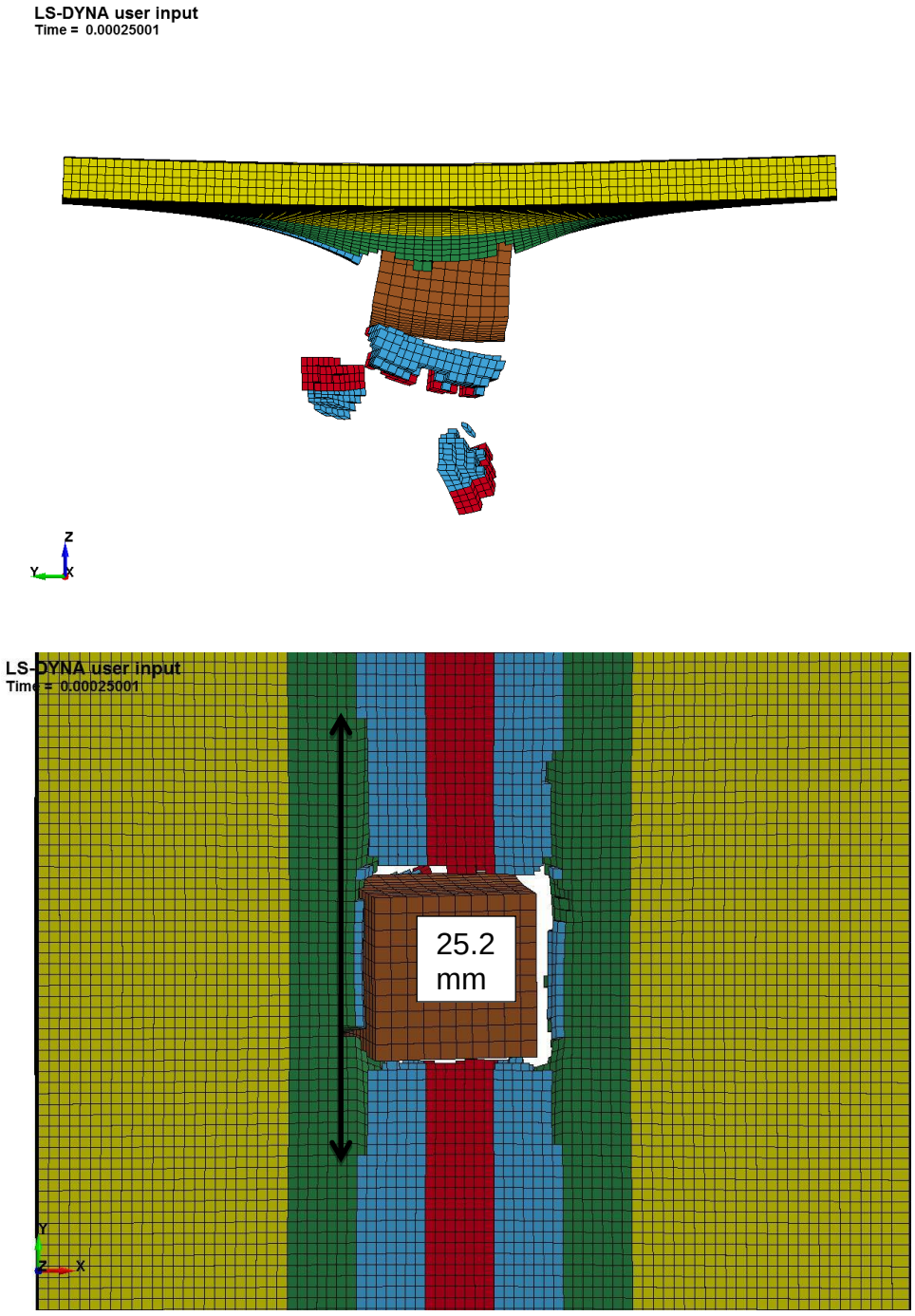

without longitudinal residual stress

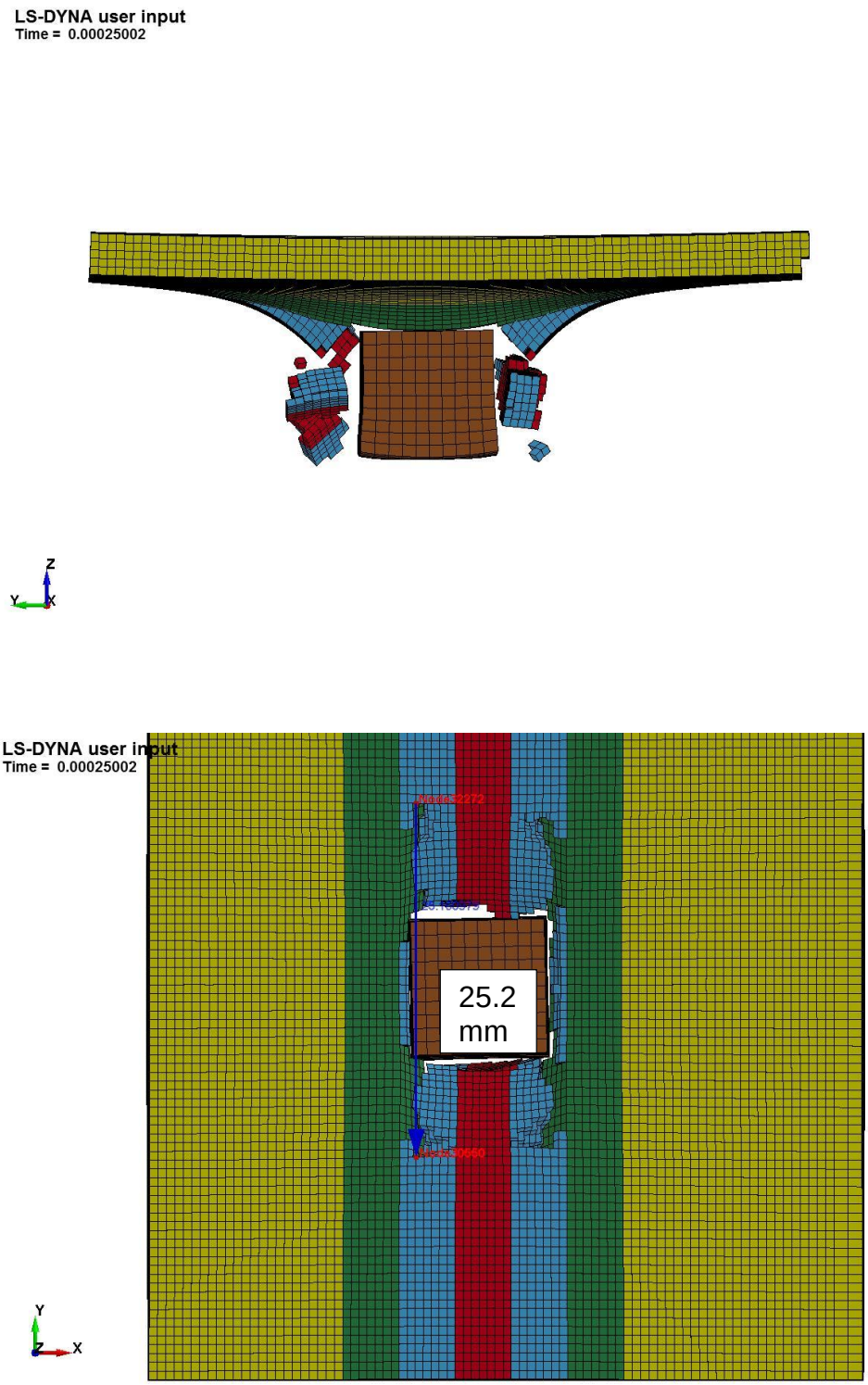

with longitudinal residual stress

Figure 5-7 Simulations of the impact with and without longitudinal residual stress

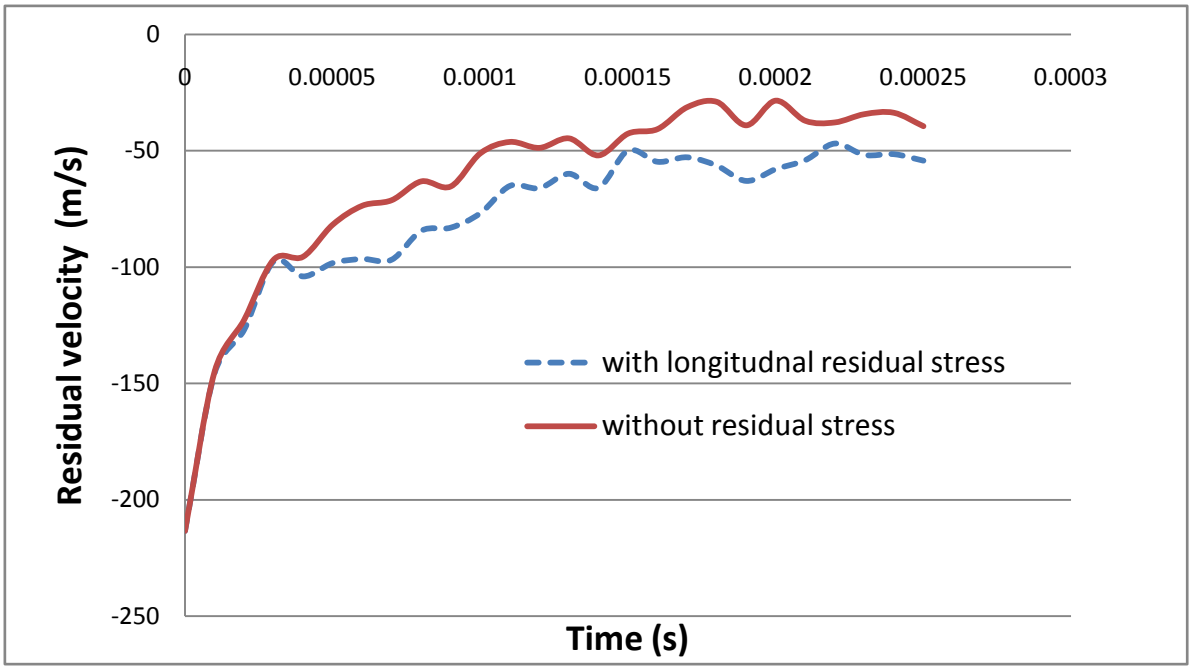

Figure 5-8 Residual impact velocity of the simulations with and without longitudinal residual stress

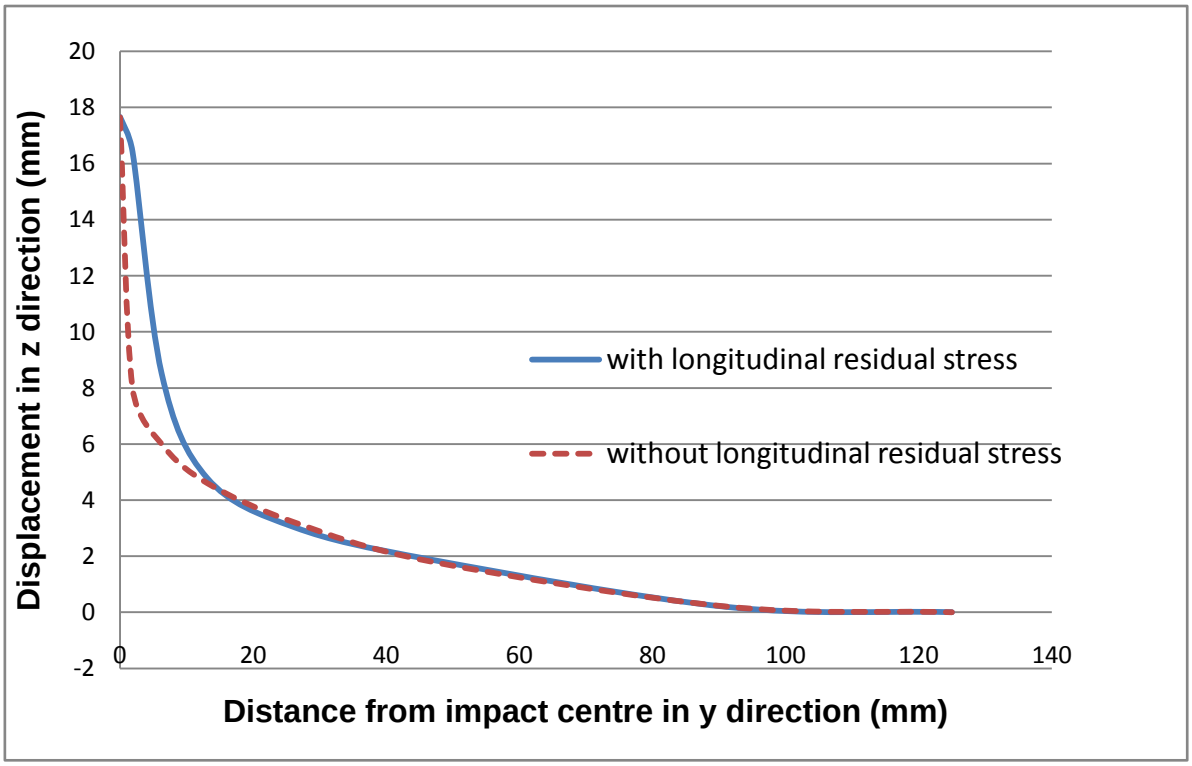

Figure 5-9 Comparison of plate-centre displacement

Figure 5-9 shows the plate-centre displacement of the simulations with and without longitudinal residual stress. The y direction is the direction of the longitudinal residual stress; the z direction is the direction of the impact velocity. The displacements are measured from the impact centre to the edge of the plate.

The plot indicates that: the overall displacement of the simulation with longitudinal residual stress is larger than that without longitudinal residual stress.

Table 5-2 Comparison of the results of the impact on the FSW plate with and without longitudinal residual stress

	With residual stress	Without residual stress
Elements failed	1593	1490
Residual velocity	-54 m/s	-39 m/s
Maximum crack length	25.2 mm	25.2 mm
Segments	6	3

The simulations show that the longitudinal stress has an influence on the dynamic response after impact:

First, the failed elements and residual impact velocity increase after longitudinal residual stress is implemented.

Second the plate model has a much greater deformation and more significant failure in y (longitudinal) direction.

In addition, in the impact on the Nugget, the residual velocity of the projectile is about 54 m/s. Thus it can be concluded that: although the 3.0 mm thick AA2024 can remain safe after impact (no penetration), the penetration occurs after the same impact on the same thickness of AA 2024 FSW plate. As the residual

velocity of the projectile is still fast, it might do severe damage to the fuel tank. According to Regulation AMS 25.963, the simulation shows that the 3.0 mm thick FSW plate may fail after impact from engine debris.

5.5 Impact on 3.0 mm FSW Plate with Different Impact Positions

In the impact simulation above, the impact centre was made on the centre (nugget zone). When repositioning the impact centre from the centre of the welds (Nugget) to TMAZ, HAZ and Base Material, additional simulations can be studied. Table 5-3 describes the different distances measured from the impact centre to the FSW joint centre. The longitudinal residual stress is also implemented in the following models.

Table 5-3 Description of impact positions

Impact centre position	Distance from centre of welds to centre of projectile
TMAZ	4.75 mm
HAZ	9.75 mm
BM (a)	14.50 mm
BM (b)	19.75 mm

The results of each simulation are shown in Figure 5-10, Figure 5-11, Figure 5-12 and Figure 5-13 respectively.

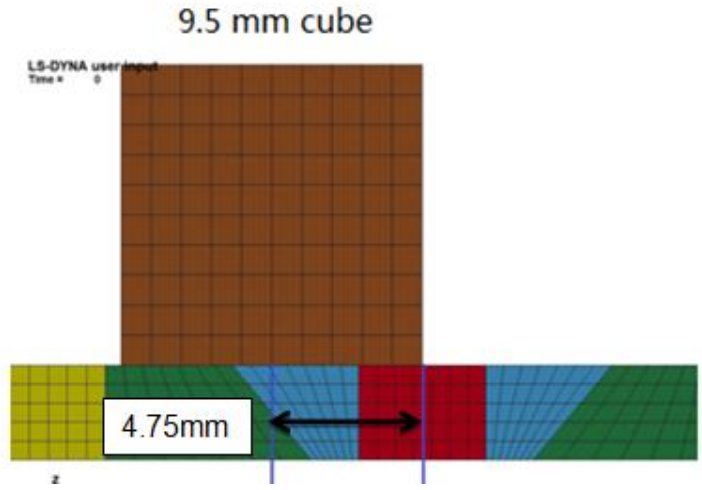

t= 0s

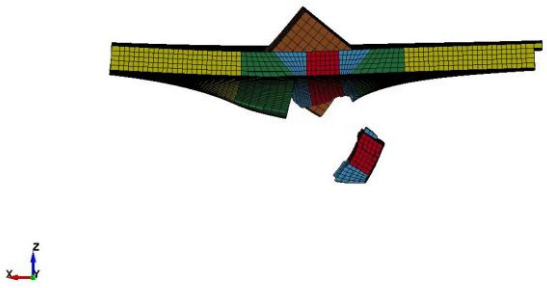

t=0.00028s

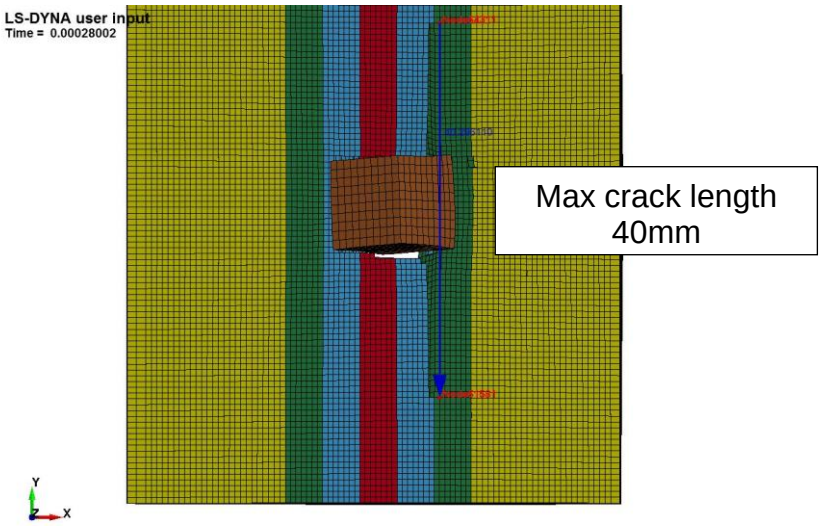

view from top

Figure 5-10 Impact centre on TMAZ

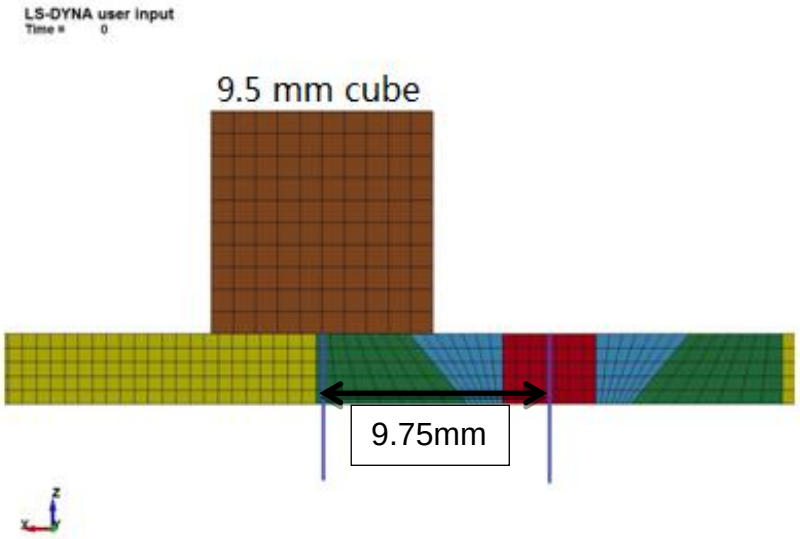

t=0s

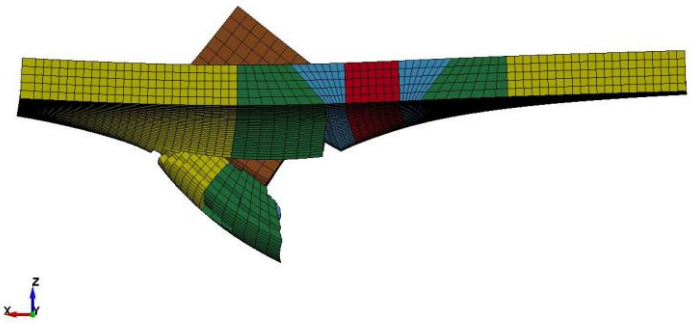

t=0.00028s

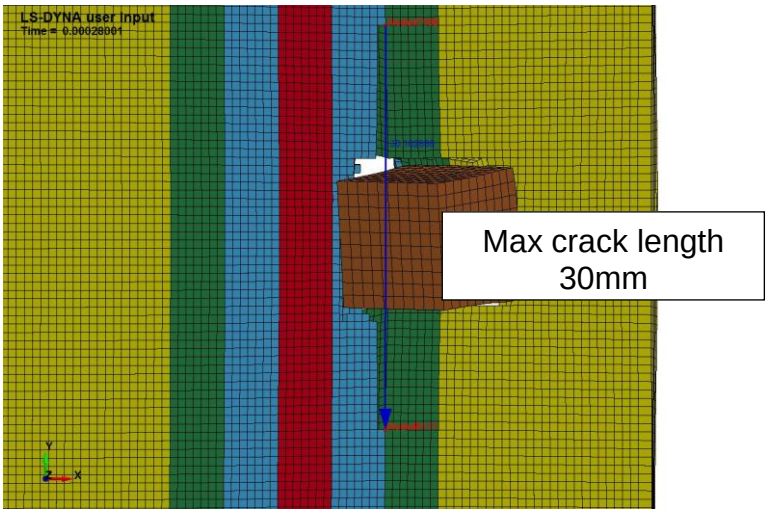

view from top

Figure 5-11 Impact centre on HAZ

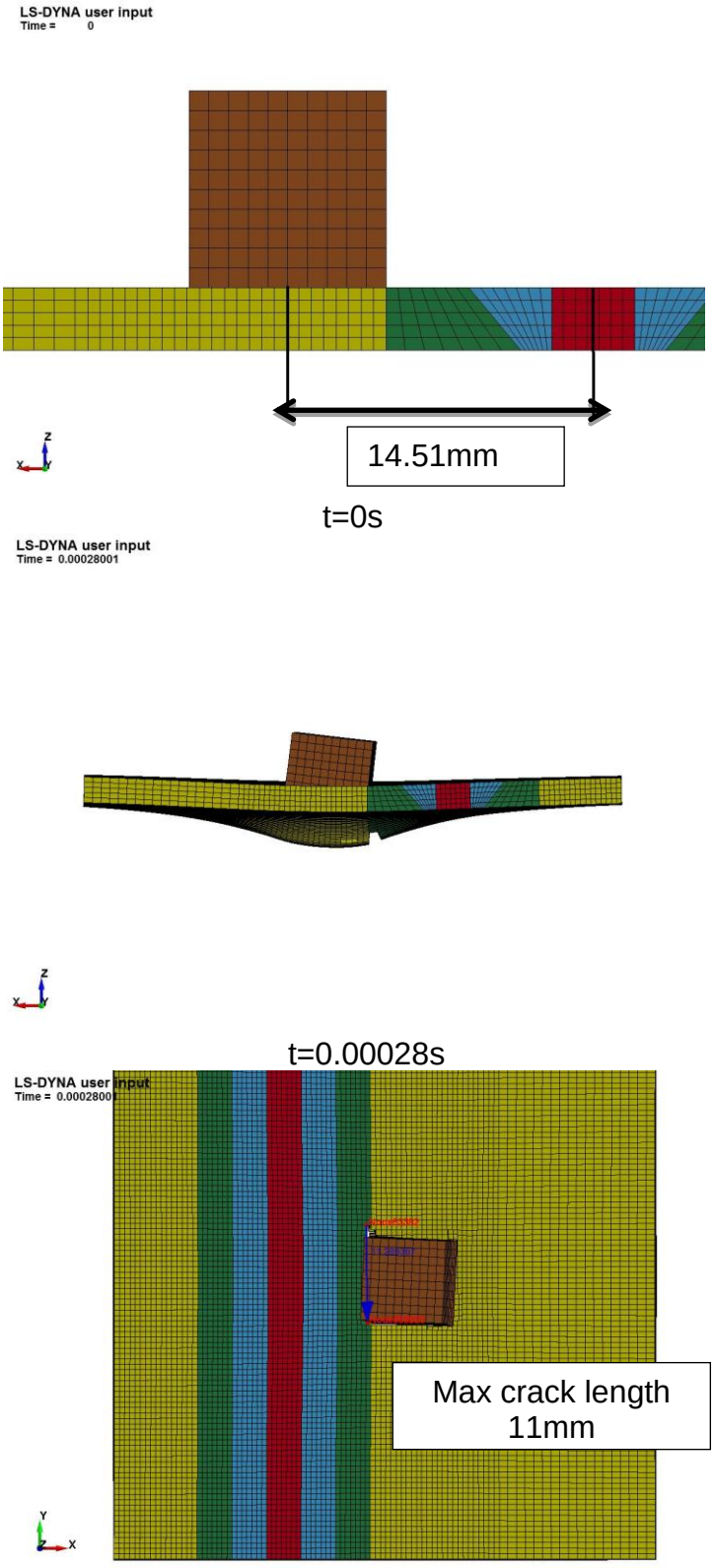

Figure 5-12 Impact on BM (a) (14.5 mm from centre of welds to impact centre)

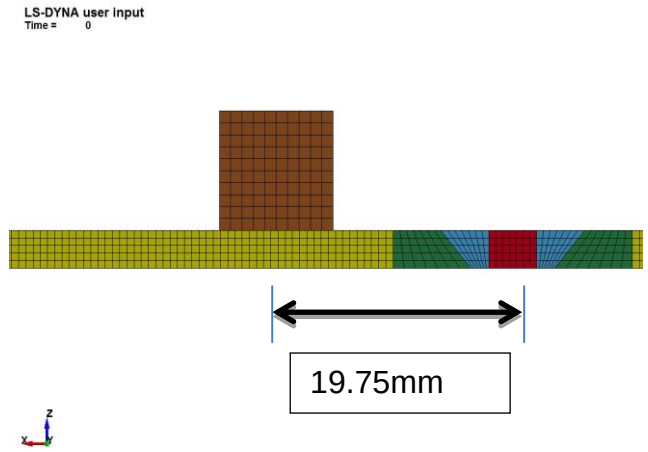

t=0s

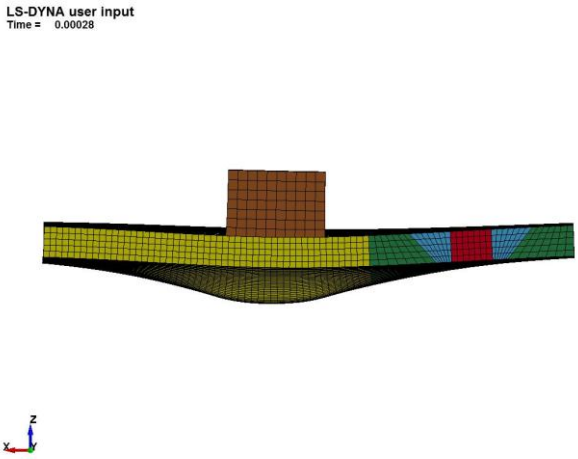

t=0.00028s

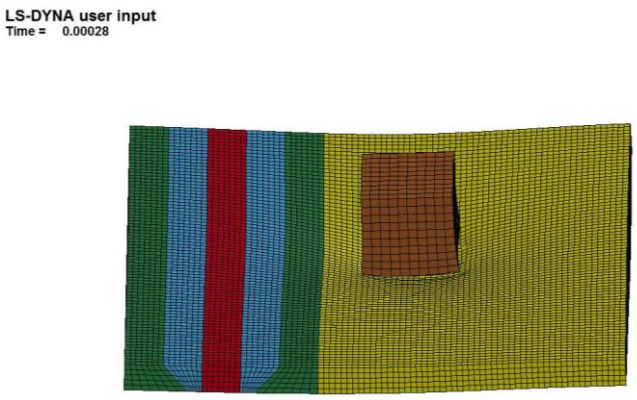

view from top

Figure 5-13 Impact on BM (b) (19.75 mm from centre of welds to impact centre)

The residual velocity of each impact simulation is shown in Figure 5-14.

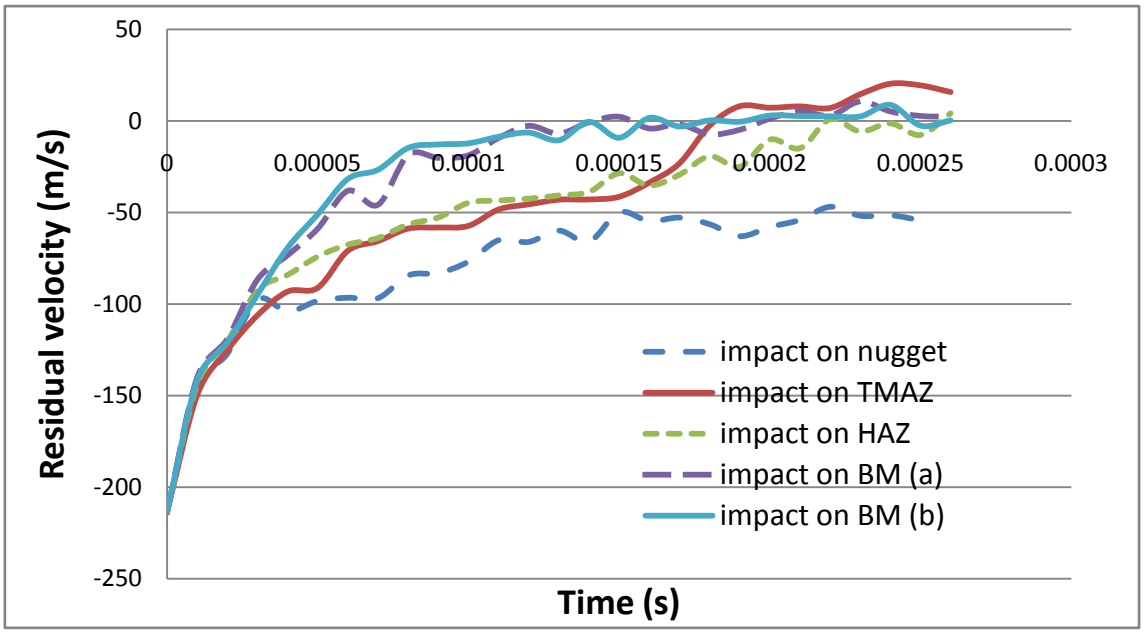

Figure 5-14 Comparison of residual velocity of various impact positions

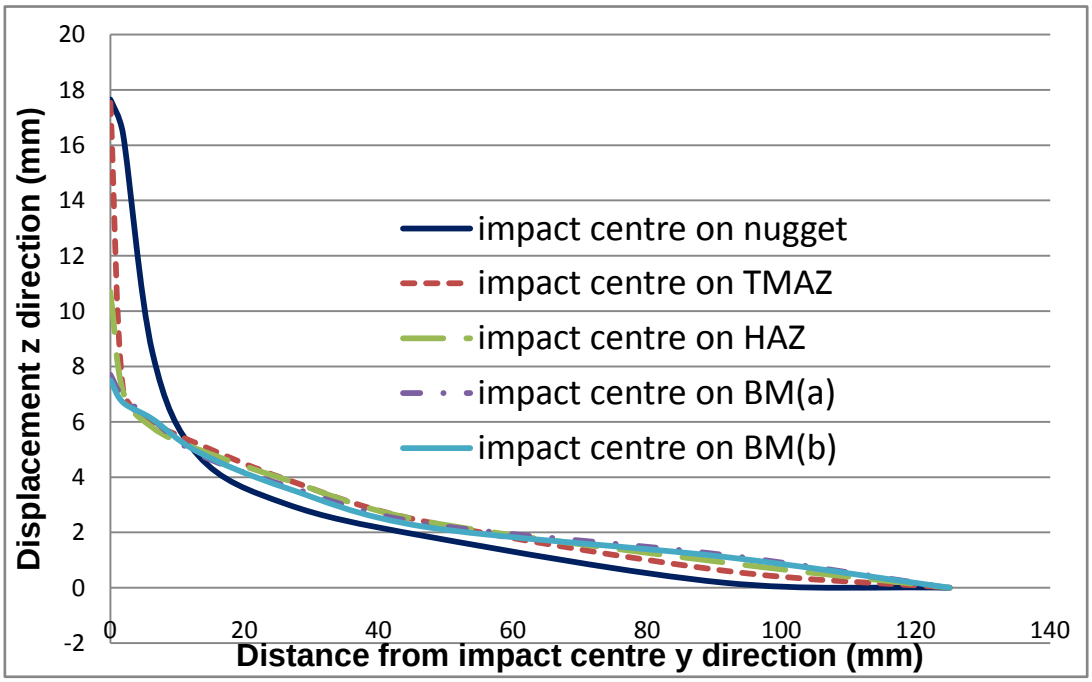

Figure 5-15 Comparison of the plate-centre displacement of different simulations

Figure 5-15 shows the plate-centre displacement of the models with different impact centres. The displacement of the model with impact centre on the

nugget is the largest; the displacement of the model with impact centre on TMAZ is the second largest; the displacement of the model with impact centre on HAZ is the third one; the displacement of the model with impact centre on BM (b) is the smallest while that with impact centre on BM (a) is slightly larger than BM (b).

Table 5-4 Comparison of the results of various impact positions

	Impact centre on Nugget	Impact centre on TMAZ	Impact centre on HAZ	Impact centre on BM (a)	Impact centre on BM (b)
Elements fail	1593	930	689	245	28
Residual velocity	-54 m/s	15 m/s	4.1 m/s	2.3 m/s	0.3 m/s
Displacement of impact centre	17.65 mm	17.56 mm	10.71 mm	7.72 mm	7.55 mm
Maximum crack length	25.2 mm	40 mm	30 mm	11 mm	0
Segments failed	6	1	0	0	0
Penetration	yes	no	no	no	no

The simulations indicate that the projectile penetrated the FSW plate when impact centre was made on the nugget, while no penetration occurs when the impact centre was made on the TMAZ, HAZ or BM.

According to the data shown in Table 5-4, the following be concluded: further away from the centre of the welds (Nugget), fewer elements fail; smaller displacement occurs in the impact centre of the plate; the maximum crack length reduces when changing impact position apart from centre. When the impact centre is about 19.75 mm away from the centre of the welds, there would be only deformation without any crack in the plate.

It can also be concluded that the impact on the centre (nugget) of the plate will be the most dangerous situation. In the later simulation, only the impact on the centre of the plate will be focused on.

The results of impact on BM (b) (19.75 mm from welds centre to impact centre) can be compared with the result of impact on homogenous AA 2024 plate (shown in Figure 5-5, with FSW geometry).

Figure 5-16 and Table 5-5 show that the results (residual velocity, failed elements i.e.) of these two simulations are very close. This is because in the model of BM (b) the impact centre was so far away (19.75 mm) from the welds that it may have the same results as the impact on homogenous AA 2024 plate.

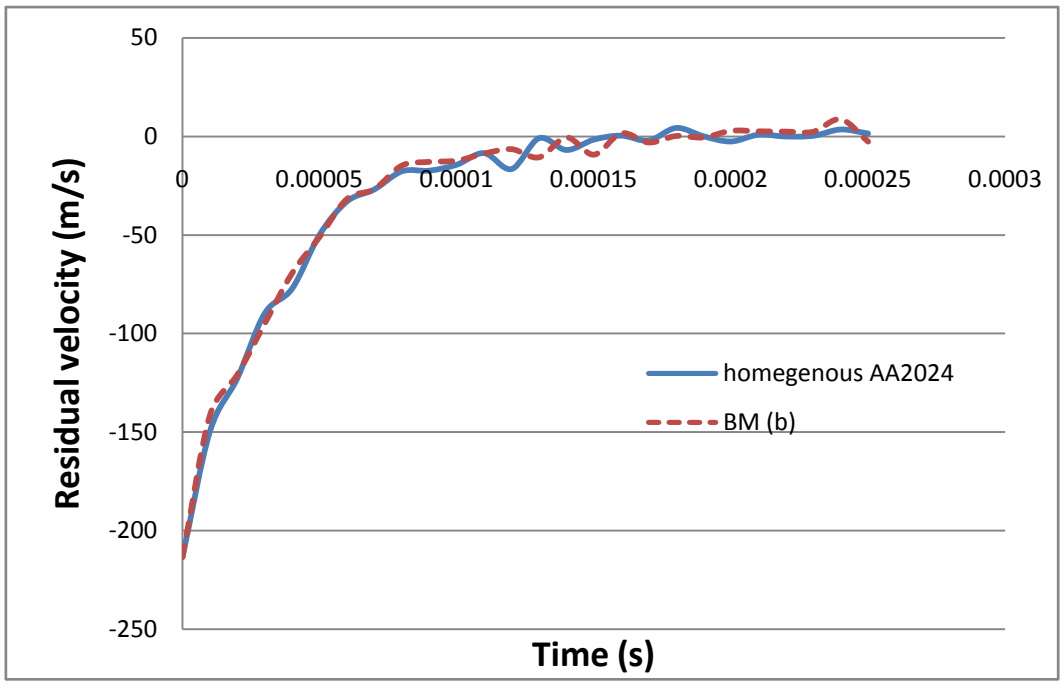

Figure 5-16 Residual velocity of BM (b) and homogenous AA 2024

Table 5-5 Comparison of the results of impact on BM (b) and impact on homogenous AA 2024 plate

	Impact centre on BM (b)	Impact on AA 2024 plate
Elements fail	28	2
Residual velocity	0.3 m/s	1.4 m/s
crack	no	no

5.6 Model with Stringers

Two stringers (1 mm thick) built in shell elements are added to the plate model. The dimensions are shown in Figure 5-17. The contact tyre of the stringer and the plate is TIEDED_SURFACE_TO_SURFACE.

The material model of the stringer is AA 2024 which is as the same as the base material of the plate model. Rivets are not involved in this model.

Edge layers nodes of the plate are fully restrained. The nodes of both ends of the stringer are fully restrained as well. The impact was made in between the stringers, as shown in Figure 5-18.

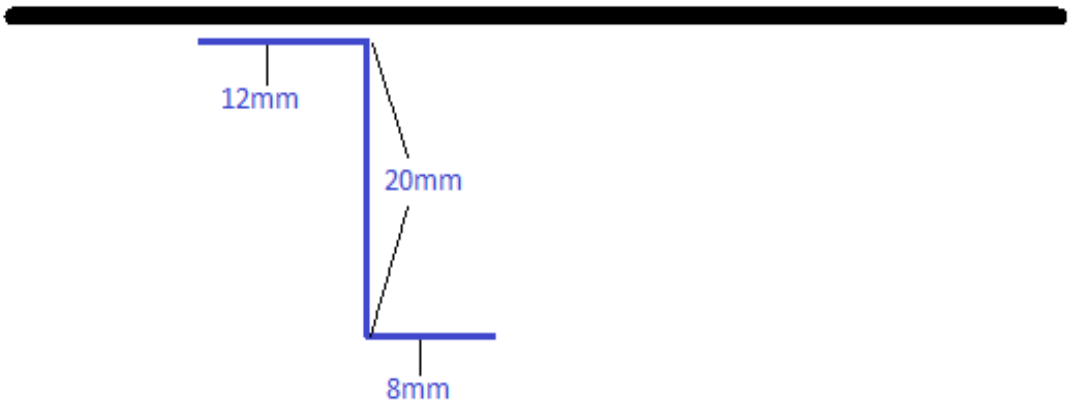

Figure 5-17 Dimensions of stringers

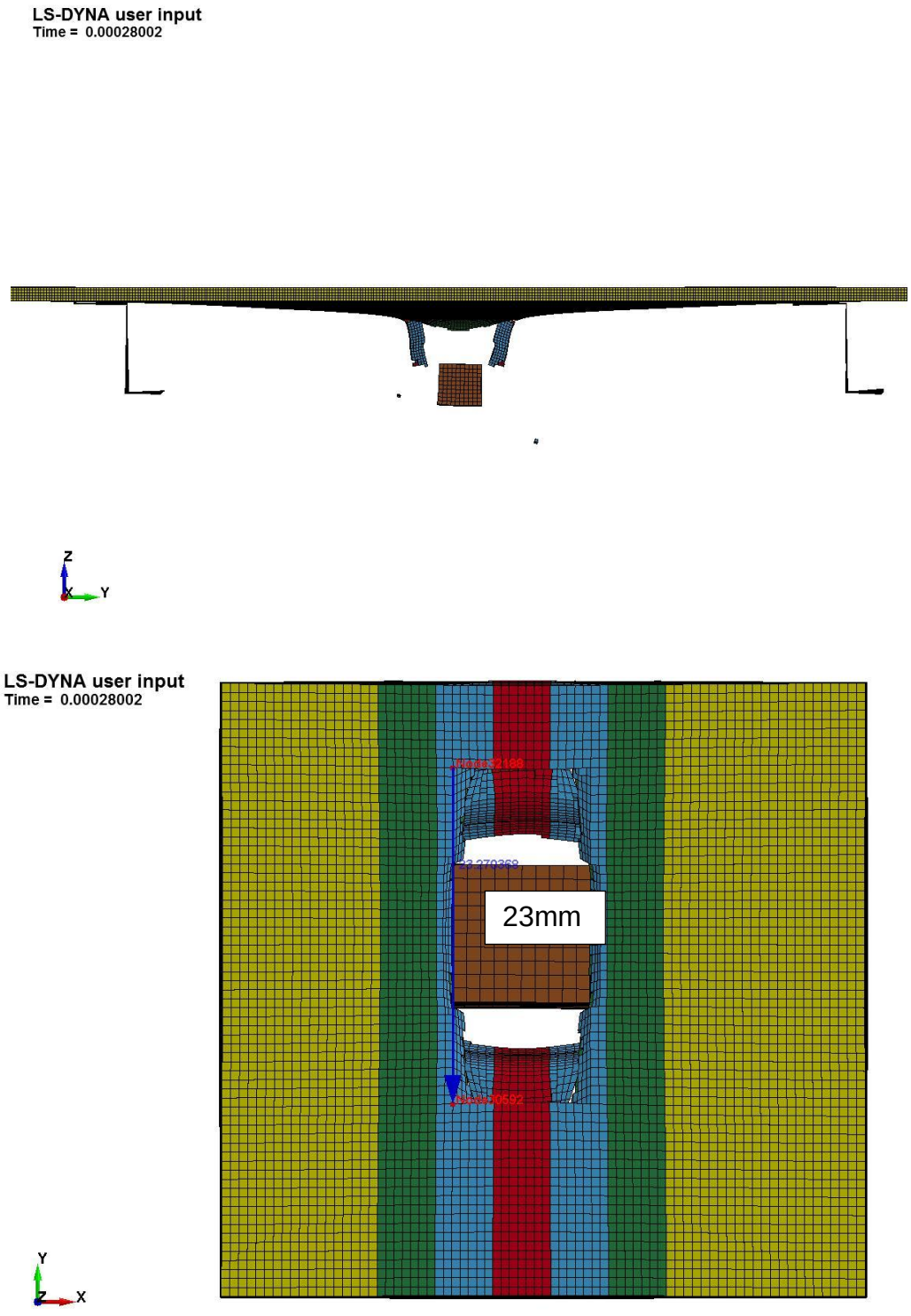

Figure 5-18 Simulation of impact on the FSW plate with stringers

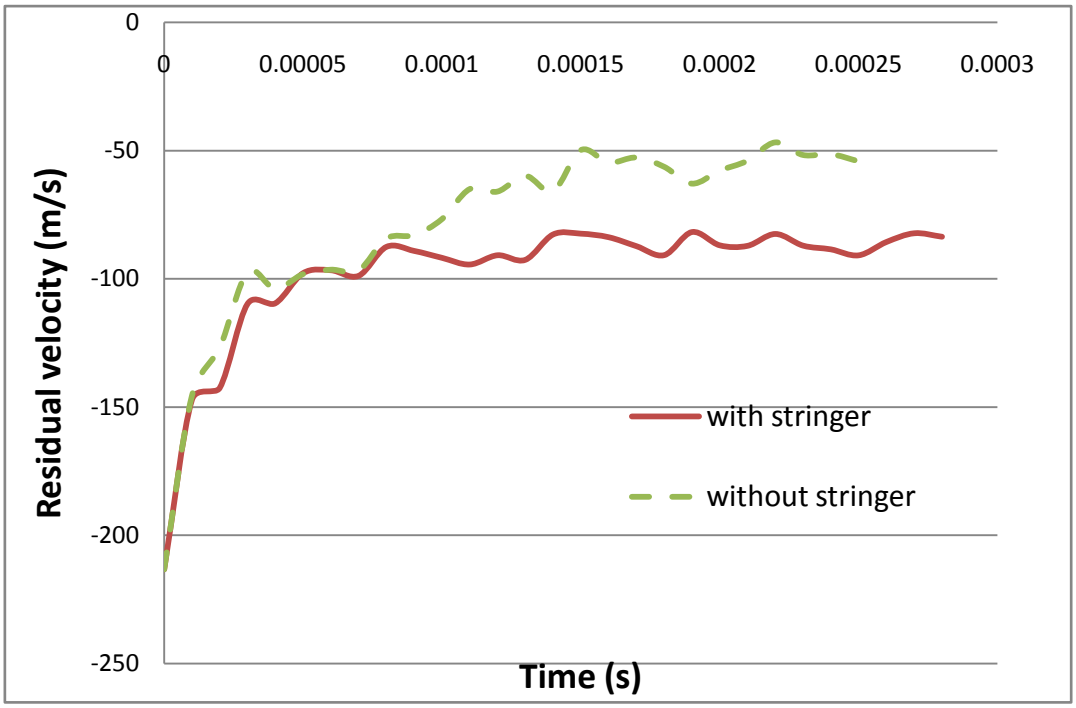

Figure 5-19 Comparisons of the impact on the FSW plate with and without stringers

Figure 5-18 and Figure 5-19 show the result of the simulation: 1277 elements failed after the impact; residual impact velocity is 80 m/s; the maximum crack length is 23 mm. Thus it can be concluded from the simulation that when adding the stringer to the plate, the engine debris will cause more significant damage to the plate. The reason is that the stringers added more stiffness to the FSW plate, as shown in Figure 5-20. However more stiffness decreased the toughness of the plate and then the projectile could cause more damage .

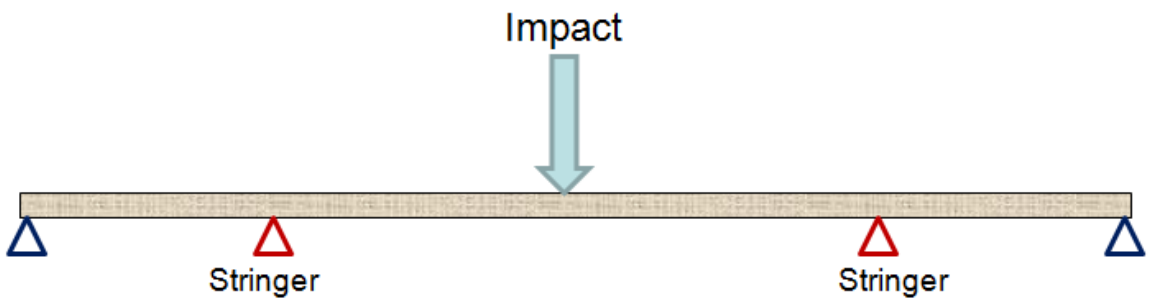

Figure 5-20 Illustration of adding stringers

5.7 Simulation of Impact on a 3.6 mm Plate

In this section, the thickness of the FSW plate model is increased to 3.6 mm. Rai. R. et al. [32] reviewed the friction stir welding tools for different thickness of the work piece. When welding a 4 mm thick Aluminium Alloy 7020-T6 plate, the pin diameter would be 3 to 8 mm and the shoulder size would be 10 to 20 mm. Thus a FSW tool with a 4 mm diameter pin and 12 mm diameter shoulder could be suitable for a 3.6 mm plate. By using the same welding tool, it can be assumed that the size of each zone in the FSW joint and the longitudinal residual stress of a 3.6 mm AA2024 FSW plate would be the same as those of a 3 mm plate. Then the 3.6 mm thick target plate can be built with only an increase in the thickness of the plate model.

This section is concerned with only the impact on the Nugget area as the impact on the Nugget area is the most dangerous situation (see Section 6.5).

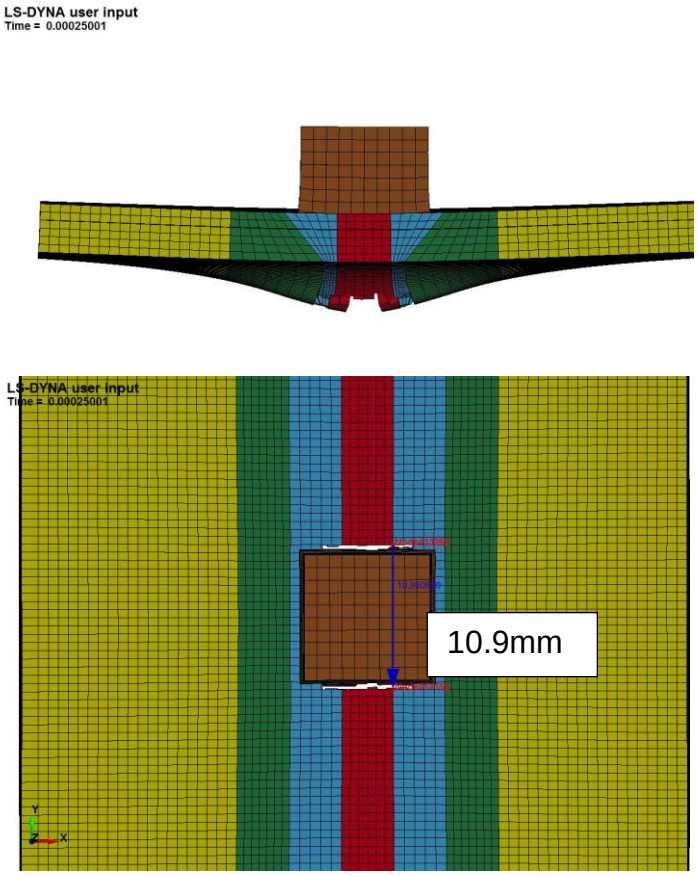

Figure 5-21 Simulation of the impact on 3.6 mm thick plate

Figure 5-21 shows that: although the meshes of the Nugget and TMAZ around the impact area have experienced deformation and part of them has failed, the projectile has not penetrated the FSW plate.

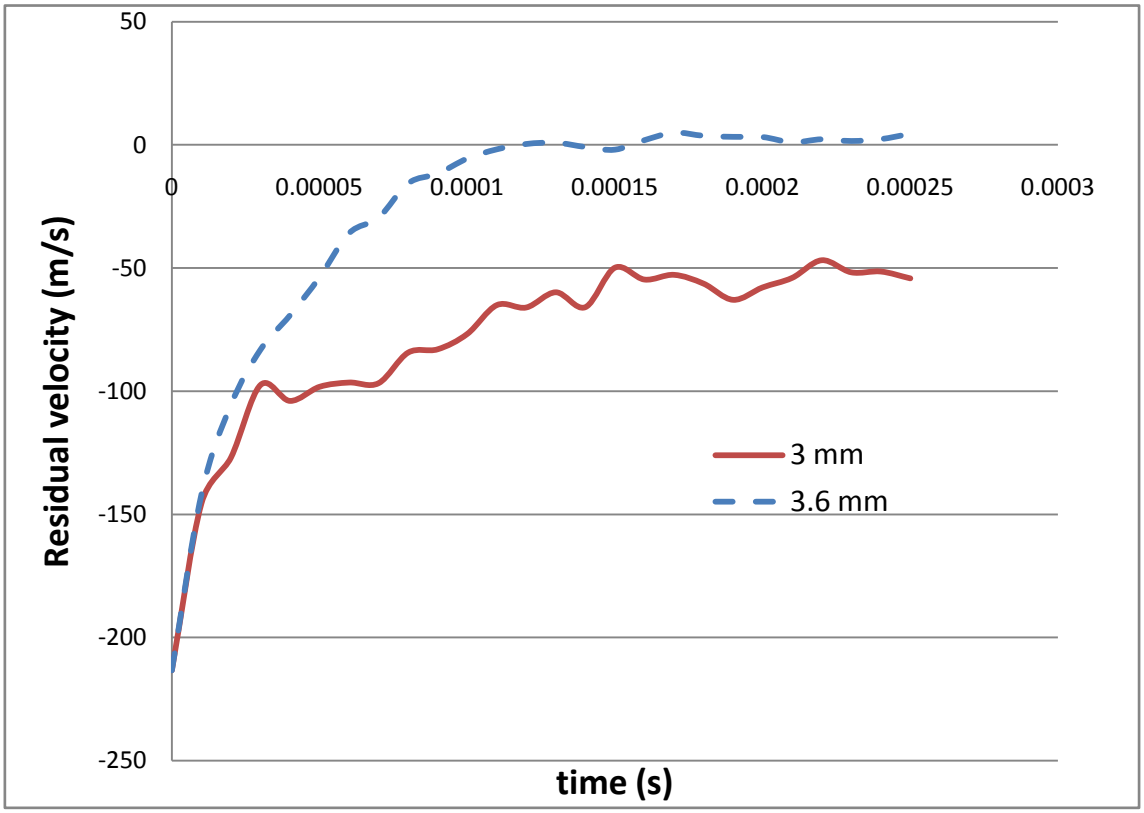

Figure 5-22 Comparison of impact on 3 mm and 3.6 mm FSW plate

In this simulation the velocity of the projectile reduced dramatically and the projectile was finally stopped, as shown in Figure 5-22. 667 elements failed in the simulation and the maximum crack length was 10.9 mm.

It can be concluded that: the 3.6 mm thick FSW plate can remain safe and resistant to penetration after impact. According to the Regulations, the minimum thickness of the AA 2024 FSW plate which can withstand the impact is 3.6 mm.

5.8 Discussion

An interesting discovery was found when rechecking the FE models. After the Johnson-Cook material model has been implemented in to the FE model, the value of the longitudinal residual stress was altered, as shown in Figure 5-23.

The value reduced 1/3 when comparing with the original plate model with longitudinal residual stress (see Figure 5-6). However, the distribution of the longitudinal residual stress still remained same with only the values altered in regularity.

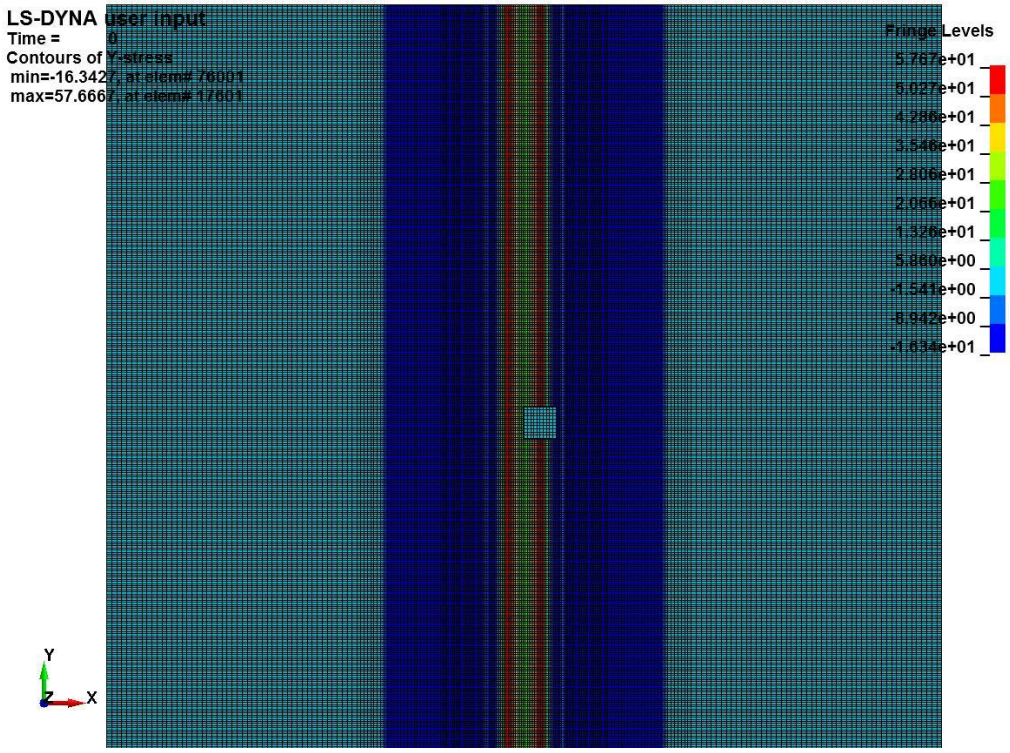

Figure 5-23 Altered longitudinal residual stress (unit: MPa)

Constitutive models which do not employ equation of state calculate the total stress directly, while the model with equation of state calculates only the deviatoric stress [33]. In this research the equation of state is necessary when using the Johnson-Cook material model.

The reason may be that the equation of state recalculated the stress. In LS-DYNA, total stress is the sum of deviatoric stress and pressure. The mean stress is equal to pressure.

By using equation (3-3), the mean stress can be calculated as:

$$\sigma_m = \frac{1}{3}(\sigma_1 + \sigma_2 + \sigma_3) \quad (3\text{-}3)$$

The deviatoric stress is a matrix calculated as:

$$\left[\delta\sigma_{ij}\right] = \begin{bmatrix} \sigma_{11} - \sigma_m & \sigma_{12} & \sigma_{13} \\ \sigma_{21} & \sigma_{22} - \sigma_m & \sigma_{23} \\ \sigma_{13} & \sigma_{32} & \sigma_{33} - \sigma_m \end{bmatrix}$$ [34] (6-1)

where σ_1, σ_2 and σ_3 are σ_x, σ_y (longitudinal stress) and σ_z respectively. In this research only the longitudinal residual stress is implemented in the model. The initial stress in x and z direction is zero. Thus the mean stress (σ_m) is 1/3 the stress in y direction (σ_y).

According to equation (6-1), the initial deviatoric stress ($\sigma_y - \sigma_m$) in the longitudinal direction is 1/3 lower than total stress (σ_y). As the magnitude of the longitudinal stress value changed is 1/3, the assumption can be that Figure 5-23 possibly shows the initial deviatoric longitudinal stress after the Johnson-Cook material model has been implemented. The assumption will be investigated in the further work.

5.9 Summary

First, two models of 3 mm thick AA 2024 FSW plate were studied. One was with longitudinal residual stress while the other was without. In both simulations the projectile hit the centre of the welds (nugget). The results of the residual velocity, failed elements, maximum crack length and failed segments were compared. The comparison showed that in the plate model with residual stress the residual velocity was higher, and; the failed elements and segments were more. It could be concluded that the longitudinal residual stress altered the dynamic response of the FSW plate and made the plate weaker when in a hard projectile impact situation. The reason may be that the longitudinal residual stress could add to the stress caused by impact and then increase the total stress, thus more damage. Therefore, the longitudinal residual stress cannot be ignored in this research.

Then additional simulations in which the impact centre varied were performed to investigate the effect of different impact centres and to find out which one was

the most dangerous. In these simulations the impact centre was changed from the centre of the plate (nugget) to the TMAZ, HAZ and BM. The residual velocity, failed elements, maximum crack length and failed segments were also compared.

The results showed that:

- The penetration occurred only when the impact centre was made in the centre (nugget). Although the tensile test showed that TMAZ has the lowest mechanical property of all the zones in FSW, the impact centre on the nugget was the most dangerous. This is because the projectile size is bigger than the size of the nugget and the TMAZ. In the impact on nugget the projectile hit nugget and the both two TMAZ, while in the impact centre on TMAZ the projectile hit only one TMAZ, HAZ and BM (as show in Figure 5-10).
- The maximum crack length and failed elements reduced when the impact position changed to further away from the centre;
- When the projectile hit the area about 19.75 mm away from the welds centre, crack did not occur.

Thus it can be concluded that the FSW would weaken the plate and the centre of the welds would be the weakness area.

Further research was done by adding stringers to the plate. The simulations showed that the projectile will cause more significant damage in contrast to the model without stringers. The reason may be that adding stiffness would reduce the toughness.

Finally, by increasing the thickness of the plate up to 3.6 mm, a further simulation was carried out. Even if the projectile hit the weakest area (Nugget), penetration did not occur. Thus the simulation indicated that a 3.6 mm thick AA 2024 FSW plate could remain safe after impact from engine debris.

6 Conclusion and Recommendations

6.1 Conclusion

In this research the AA 2024 FSW plate model was well developed. The Johnson-Cook material model which is suitable for high strain rate material was chosen for the hard projectile impact simulation. The parameters of the material model were determined by data fitting methods and then validated by global tensile tests on the FSW specimen. The penetrations with various impact velocities of 1/4" AA 2024 plate were simulated to determine a proper mesh density and minimum thickness of a humongous AA 2024 plate.

Then a 3 mm FSW plate was tested and the results were compared with the humongous plate. In the simulation of the FSW target plate engine debris penetrated when impacting on the Nugget, while in same thick humongous AA 2024 plate no element failed and no penetration occurred. When increasing the thickness up to 3.6 mm, the projectile did not penetrate the plate. According to the goal based on AMC 25.963(e) of CS25, the projectile should not penetrate the plate. Thus when using the FSW process in the aircraft skin joining, a 3.6 mm thick FSW skin would be required to satisfy the Regulations.

As a 3.6 mm skin is commonly used in aircraft, the FSW process may be suitable for aircraft skin prone to the impact of engine debris.

6.2 Recommendations

Some future work needs to be done to improve the accuracy of the simulations.

First, the Johnson-Cook material model needs to be refined. Local tensile tests of Nugget, TMAZ and HAZ with different strain rates should be done to refine the parameters (A, B, n and C) of the Johnson-Cook material model. As mentioned in Section 4.2.3, due to lack of tensile tests with different triaxialities, the damage coefficients D_1-D_3 are not accurate enough. These local tensile specimens with different strain rates could be also made with different notch radii to obtain different triaxialities.

The maximum stress triaxiality can be calculated as

$$\sigma^*_{\max} = \frac{1}{3} + \ln(1 + \frac{a}{2R}) \quad [35] \ (6\text{-}1)$$

a is the minimum thickness of the specimen in the necking region and R is the initial notch radii. In this way, a more accurate damage coefficient could be determined.

Second, as the longitudinal residual stress has an important effect on the dynamic response of the FSW plate, the transverse residual stress could be also implemented in the plate model to estimate how important the effect of the transverse residual stress could be.

Third, the skin of an airplane experiences tension or compression during the flight. More realistic simulations could be performed by adding the induced stress.

Fourth, a finite element model of AA 2024 plate joined by riveting can be built. A impact in the same simulation can be performed to compare with the dynamic response of the plate joined by FSW.

Finally, some experimental studies of the impact on AA 2024 FSW plate can be conducted. Then validation can be done by comparing these with the results of FE model.

REFERENCES

1. Mishra, R. S. and Ma, Z. Y. (2005), “Friction stir welding and process”, *Material Science and Engineering,* vol. 50, pp.1-78.

2. Lansiaux, R. (2010), “Simulation of Bird-Strike on Friction Stir Welded Panel”, MSc thesis, *Cranfield University.*

3. Flight (2008), Eclipsing the past, available at http://www.flightglobal.com/news/articles/eclipsing-the-past-206252/.

4. Photos-Qantas A380 Engine Failure (2011), available at http://blog.flightstory.net/1570/photos-qantas-a380-engine-failure/.

5. European Aviation Safety Agency (5 August 2010), “Certification specifications for large aeroplanes CS-25 Amendment 9”.

6. Dubourg, L., Merati. A. and Jahazi, M. (2010), “Process optimisation and mechanical properties of friction stir lap welds of 7075-T6 stringers on 2024-T3 skin”, *Material and Design*, Vol.31, pp.3324-3330.

7. Liu, H. J., Fujii, H., Maeda, M. and Nogi, K. (2003), “Tensile properties and fracture location of friction-stir-welded joints of 2017-T351 aluminium alloy”, *Journal of Material Processing Technology*, Vol. 142, pp. 692-696.

8. Lockwood, W. D., Tomaz, B. and Reynolds, A. P. (2002), “Mechanical response of friction stir welded AA2024: experiment and modelling”, *Material Science and Engineering*, Vol. 323, pp. 348-353.

9. Reynolds, A. P. (2000), “Visualization of material flow in an autogenous friction Stir Weld”, *Science and Technology of Welding and Joining,* vol.5, no. 2, pp. 120-124.

10. Attallah, M. M. and Salem, H. G. (2005), “Friction stir welding parameters: a tool for controlling abnormal grain growth during subsequent heat treatment”, *Material Science and Engineering,* Vol. 391, pp. 51-59.

11. Chao, Y. J., Wang, Y. and Miller, K. W. (2001), “Effect of friction stir welding on dynamic properties of AA 2024-T3 and AA 7075-T7351”, *the Department of Mechanical Engineering, University of South Carolina.*

12. Moreira, P., Santos, T., Tavares, S., Trummer, V., Vilaca. P. and de Castro, P. (2009), “Mechanical and metallurgical characterization of friction stir welding joints of AA6061-T6 with AA 6082-T6”, *Material and Design*, Vol. 30, pp. 180-187.

13. Genevois, C. PhD thesis, (2004), “Genèse des microstructures lors du soudage par friction malaxage d’alliages d’aluminium de la série 2000 & 5000 et comportement mécanique resultant”, *Institut Nationale Polytechnique de Grenoble, Grenoble, France.*

14. Johnson, G. R. and Cook, W. H. (1983), “A constitutive model and data for metals subjected to large strains, high strain rates and high temperatures”, *Seventh International Symposium on Ballistics.*

15. Hallquist, J.O. (2007), “LS Dyna, keyword user's manual volume 1”, *LSTC*, version 971st, Troy, Michigan.

16. Gupta, N. K., Iqbal, M. A. and Sekhon, G. S. (2006), “Experimental and numerical studies on the behavior of thin aluminium plates subjected to impact by blunt- and hemispherical-nosed projectiles”, *International Journal of Impact Engineering*, Vol. 32, pp. 1921-1944.

17. James, M. and Mahoney, M. (1999), “Proceedings of the First International Symposium on Friction Stir Welding”, *Thousand Oaks*.

18. Prime, M. B. (1999), “Residual Stress Measurement by Successive Extension of a Slot: The Crack Compliance Method”. *Applied Mechanics Reviews,* Vol. 52, No.2, pp. 75-96.

19. Buffa, G., Pasta, S. and Shivpuri, R. (2008), “On the thermo-mechanical loads and the resultant residual stresses in friction stir processing operations”, *CIRP Annals - Manufacturing Technology*, Vol. 57, pp. 287-290.

20. Chen, C. M. and Kovacevic, R. (2003), “Finite element modeling of friction stir welding—thermal and thermomechanical analysis”, *International Journal of Machine Tools & Manufacture*, Vol. 43. pp. 1319-1326.

21. Lemmen, H J. K., Alderliesten, R. C., Pieters. R. R. G. M. and Benedictus. R. (2008), "Influence of Local Yield Strength and Residual Stress on Fatigue in Friction Stir Welding", *American Institute of Aeronautics and Astronautics*.

22. Staron, P., Kocak, M. and Williams, S. (2002), “Residual stresses in friction stir welded Al sheets”, Appl. Phys., Vol. 74, pp. 1161-1162.

23. Donne, C. D, Lima, E., Wegener, J., Pyzalla, A., Bushlaps, T., (2001), “Proceedings of the Third International Symposium on Friction Stir Welding”, Kobe, Japan.

24. Buyuk, M., Loikkanen, M. and Kan, C. S. (2008), “Explicit Finite Element Analysis of 2024-T3/T351 Aluminum Material Under Impact Loading for Airplane Engine Containment and Fragment Shielding”, DOT/FAA/AR-08/36, Air Traffic Organization Operations Planning Office of Aviation Research and Development Washington, DC 20591.

25. European Aviation Safety Agency (2009), EASA perspective on safe composite damage tolerance and maintenance practices.

26. Cook. R. D. (1989), “Concepts and applications of finite element analysis”, 3rd edition.

27. Wu, J., Song, G., Yeh. C. and Wyatt, K. (1998), “Drop/Impact Simulation and Test Validation of Telecommunication Products”, *Applied Simulation and Modeling Research (ASMR).*

28. Time integration, LS-DYNA Support (2011), available at http://www.dynasupport.com/tutorial/ls-dyna-users-guide/time-integration.

29. Hallquist, J. O. (2006), “LS-DYNA theory manual”, Livermore Software Technology Corporation.

30. Lesuer, D. R. (2000), “Experimental Investigations of Material Models for Ti-6Al-4V Titanium and 2024-T3 Aluminum”, DOT/FAA/AR-00/25, U.S. *Department of Transportation Federal Aviation Administration Office of Aviation Research* Washington, DC 20591.

31. Buyuk, M., Loikkanen, M. and Kan, C. S. (2005), “A computational and experimental analysis of ballistic impact to sheet metal aircraft structures”, 5th Europe LS-DYNA Users Conference.

32. Rai, R., De, A., Bhadeshia, H. K. D. H. and Debroy. T. (2011), “Review: Friction stir welding tools”, *Science and Technology of Welding and Joining*.

33. Equation of state, LS-DYNA Support (2011), available at http://www.dynasupport.com/howtos/general/equation-of-state .

34. Engelder, T., “Deviatoric stressitis: a virus infecting the Earth Science Community”, Department of Geosciences, The Pennsylvania State University.

35. Yan, C., Ma, W., Burg. V., Mai, Y. –W. and Geers, M. (2006), “Notch effects in tensile behavior of AM60 magnesium alloys”, *Key engineering materials,* Vol. 312, pp. 59-64.

APPENDICES

Appendix A Parameters of Johnson-Cook Material Model

Table A-1 Final Johnson-Cook material model of each zone in FSW plate

Parameter	Notation	Value			
		BM	HAZ	TMAZ	Nugget
Density (g/cm3)	ρ	2.77			
Young's modulus (GPa)	E	73.1			
Shear modulus (GPa)	G	27.5			
Poisson ratio	v	0.33			
Yield stress (MPa)	A	352	326.41	139.28	248.5
Strain hardening modulus (MPa)	B	440	585.18	632.48	714.59
Strain hardening exponent	n	0.42	0.501	0.290	0.537
Strain rate coefficient	C	0.0083	0.0083	0.0083	0.0083
Thermal softening exponent	m	1.7			
Room temperature (K)	TR	294			
Melting temperature (K)	TM	775			
Strain rate factor (s^{-1})	EPSO	1.0			
Specific heat (10E-3J/Ton-°K)	CP	875E+6			
Damage parameter 1	D1	0.13	0.087	0.059	0.059
Damage parameter 2	D2	0.13			
Damage parameter 3	D3	-1.5			
Damage parameter 4	D4	0.011			
Damage parameter 5	D5	0			

Appendix B Simulation of Global Tensile Specimen Input file

```
$$ HM_OUTPUT_DECK created 15:49:57 10-26-2011 by HyperMesh Version 11.0.0.47
$$ Ls-dyna Input Deck Generated by HyperMesh Version  : 11.0.0.47
$$ Generated using HyperMesh-Ls-dyna 971 Template Version : 11.0.0.47
*KEYWORD
*CONTROL_TERMINATION
$$  ENDTIM    ENDCYC     DTMIN    ENDENG    ENDMAS
     80.0
*CONTROL_TIMESTEP
$$  DTINIT    TSSFAC      ISDO    TSLIMT     DT2MS      LCTM     ERODE MSIST
                           -5.000E-05
*CONTROL_BULK_VISCOSITY
$$      Q1        Q2        IBQ
      2.0       0.1
$$DATABASE_OPTION -- Control Cards for ASCII output
*DATABASE_GLSTAT
      2.0         1
*DATABASE_NODOUT
      2.0         1
*DATABASE_SECFORC
      2.0         1
*DATABASE_BINARY_D3PLOT
$$ DT/CYCL      LCDT      BEAM      NPLTC
      1.0
        0
*NODE
      1            3.0            0.0            0.0

      …
6587 19.958333333333            6.0            0.0
*MAT_JOHNSON_COOK
$HMNAME MATS       1nugget
        12.7700E-09   27481.0   73100.0      0.33
    248.5    714.59     0.537    0.0083       1.7     775.0     294.0       1.0
875000000.                          0.0590      0.13      -1.5     0.011
      0.0
*MAT_JOHNSON_COOK
$HMNAME MATS       2TMAZ
        22.7700E-09   27481.0   73100.0      0.33
   139.28    632.48     0.29    0.0083       1.7     775.0     294.0       1.0
875000000.                          0.0590      0.13      -1.5     0.011
      0.0
*MAT_JOHNSON_COOK
```

```
$HMNAME MATS       3HAZ
       32.7700E-09   27481.0   73100.0      0.33
   326.41    585.18     0.501    0.0083       1.7     775.0     294.0       1.0
875000000.                            0.087      0.13      -1.5     0.011
      0.0
*MAT_JOHNSON_COOK
$HMNAME MATS       4BM
       42.7700E-09   27481.0   73100.0      0.33
    352.0     440.0      0.42    0.0083       1.7     775.0     294.0       1.0
875000000.                            0.13      0.13      -1.5     0.011
      0.0
*PART
$HMNAME COMPS       1nugget
$HWCOLOR COMPS       1       3

       1        1        1        3        2
$HMNAME COMPS       2TMAZ
$HWCOLOR COMPS       2       8

       2        1        2        3        2
$HMNAME COMPS       3HAZ
$HWCOLOR COMPS       3      20

       3        1        3        3        2
$HMNAME COMPS       42024
$HWCOLOR COMPS       4      51

       4        1        4        3        2
*SECTION_SOLID
$HMNAME PROPS       1solid
       1        1
*EOS_GRUNEISEN
$HMNAME PROPS       3eos
       3 5328000.0     1.338                      2.0      0.48

*HOURGLASS
$HMNAME PROPS       2hourglass
       2        5
*DATABASE_CROSS_SECTION_SET_ID
$HMNAME GROUPS       1xsection
$HWCOLOR GROUPS       1      50
       1
       1        2                                    0        0
*ELEMENT_SOLID
     1      1    5210    5726    5633    5100    5209    5725    5632    5099
…
4800      4    6515    6527    4819    5904    6575    6587    5278    5187
$$
```

```
$$ Sets Defined In HyperMesh
$$
*SET_NODE_LIST
$HMSET
$HMNAME SETS       1topnode
         1
       209       325       328       332       370       540       653       658
       …
6576
*SET_NODE_LIST
$HMSET
$HMNAME SETS       3gauge
         3
       604      6554
$$
$$ Sets Defined In HyperMesh
$$
*SET_SOLID
$HMSET
$HMNAME SETS       2topelement
         2
      4225      4226      4227      4228      4229      4230      4231      4232
      …
4272
*BOUNDARY_SPC_NODE
$HMNAME LOADCOLS       3constraints
$HWCOLOR LOADCOLS       3      38
       790                 1
…
  103                1
*BOUNDARY_PRESCRIBED_MOTION_NODE
$HMNAME LOADCOLS       2load
$HWCOLOR LOADCOLS       2      55
     6576         1         0         1       1.0
…
209         1         0         1       1.0
*DATABASE_HISTORY_NODE_SET_LOCAL
$HMNAME OUTPUTBLOCKS       1timehistory
         3         0         1
*DEFINE_CURVE
$HMNAME CURVES       1curve1
$HWCOLOR CURVES       1      11
$HMCURVE     1    0 curve1
         1         0       1.0       1.0
                0.0             0.067
              100.0             0.067
*END
```

Appendix C Impact on 1/4 inch Thick Aluminium Alloy 2024 plate Input file (Mesh Size 2, Initial Velocity 213 m/s)

```
$$ HM_OUTPUT_DECK created 11:16:55 10-19-2011 by HyperMesh Version
11.0.0.47
$$ Ls-dyna Input Deck Generated by HyperMesh Version  : 11.0.0.47
$$ Generated using HyperMesh-Ls-dyna 971 Template Version : 11.0.0.47
*KEYWORD memory=150000000
*TITLE

*CONTROL_TERMINATION
$$  ENDTIM    ENDCYC     DTMIN    ENDENG    ENDMAS
3.0000E-04
*CONTROL_BULK_VISCOSITY
$$      Q1        Q2        IBQ
      2.0       0.1
$$DATABASE_OPTION -- Control Cards for ASCII output
*DATABASE_GLSTAT
1.0000E-05         1
*DATABASE_NODOUT
1.0000E-05         1
*DATABASE_BINARY_D3PLOT
$$ DT/CYCL      LCDT      BEAM     NPLTC
5.0000E-06
         0
*NODE
       1           30.0           30.0            0.0
       …
674607 6.9277108433735 -8.734939759036         -3.175
*MAT_PLASTIC_KINEMATIC
$HMNAME MATS       2steel
         27.8400E-09  206800.0       0.3     470.0       0.0
       0.0       0.0       0.0
*MAT_JOHNSON_COOK
$HMNAME MATS       12024
         12.7700E-09   27475.0   73084.0      0.33
     359.0     684.0      0.73    0.0083       1.7     775.0     294.0       1.0
875000000.                             0.13      0.13      -1.5     0.011
       0.0
*PART
$HMNAME COMPS       1plate
$HWCOLOR COMPS       1      29

         1         1         1         3         2
$HMNAME COMPS       2proj
```

```
$HWCOLOR COMPS       2      19

       2        1        2                2
*SECTION_SOLID
$HMNAME PROPS       1solid
       1
*EOS_GRUNEISEN
$HMNAME PROPS       3eos
       3 5328000.0     1.338       0.0       0.0       2.0      0.48

*HOURGLASS
$HMNAME PROPS       2hourglass
       2        5
*CONTACT_ERODING_SURFACE_TO_SURFACE_ID
$HMNAME GROUPS       4contact
$HWCOLOR GROUPS       4      11
       4
       2        1        3        3
     0.5

       1        1
*ELEMENT_SOLID
  93693        2   102101   101777   102258   102477   102477   102477   102477
102477
…
654179        1   635924   635926   635970   635966   674561   674563   674607
674603
$$
$$ Sets Defined In HyperMesh
$$
*SET_NODE_LIST
$HMSET
$HMNAME SETS       1gauge
       1
    98225     98852     98989
*BOUNDARY_SPC_NODE
$HMNAME LOADCOLS       5constrants
$HWCOLOR LOADCOLS       5      39
   572518                1        1        1        1        1        1
…
650072                1        1        1        1        1        1
*INITIAL_VELOCITY_NODE
$HMNAME LOADCOLS       6veloctity
$HWCOLOR LOADCOLS       6      55
   104956       0.0       0.0 -213000.0
…
  98122       0.0       0.0 -213000.0
*DATABASE_HISTORY_NODE_SET_LOCAL
```

```
$HMNAME OUTPUTBLOCKS       1velocities
        1        0        1
*END
```

Appendix D Longitudinal Residual Stress Matlab Programme

```
clear all;
close all;
load nodes.txt;
load elements.txt;
file=fopen(' residual stress.txt','w');
S=[];
w=0.278812468014942;
cnt=27.5546951497632;
a1=41.9934789437565;
a2=-28.6090895907605;
a3=-18.3004028512595;
a4=8.35895502333475;
a5=7.02559197414655;
a6=-2.74147529219754;
a7=-1.60878242574568;
a8=3.89288213071716;
a9=0.755956414501549;
a10=-2.54813781283501;
for i=1:1:length(elements),
x=[nodes(elements(i,3),2);nodes(elements(i,4),2);nodes(elements(i,5),2
);nodes(elements(i,6),2);nodes(elements(i,7),2);nodes(elements(i,8),2)
;nodes(elements(i,9),2);nodes(elements(i,10),2)];
X=mean(x);
if abs(X)<11.5,
Y=[elements(i,1) 1 0 0 0];
Z=[0
cnt+a1*cos(w*X)+a2*cos(2*w*X)+a3*cos(3*w*X)+a4*cos(4*w*X)+a5*cos(5*w*X
)+a6*cos(6*w*X)+a7*cos(7*w*X)+a8*cos(8*w*X)+a9*cos(9*w*X)+a10*cos(10*w
*X) 0 0 0 0 0];
S=[S;Y,Z];
elseif 11.5<abs(X)<42.5,
Y=[elements(i,1) 1 0 0 0];
Z=[0 -24.52 0 0 0 0 0];
S=[S;Y,Z];
end
end
for r=1:1:length(S),
fprintf(file,'%5d,%1d,%1d,%1d,%1d,\n%1d,%4.2E,%1d,%1d,%1d,%1d,%1d\n',S
(r,1),S(r,2),S(r,3),S(r,4),S(r,5),S(r,6),S(r,7),S(r,8),S(r,9),S(r,10),
```

```
S(r,11),S(r,12));
end
fclose('all');
```

Appendix E Impact on Nugget zone Input file (3.0 mm FSW plate with Longitudinal Residual Stress)

```
$$ HM_OUTPUT_DECK created 11:15:39 11-04-2011 by HyperMesh Version
11.0.0.47
$$ Ls-dyna Input Deck Generated by HyperMesh Version  : 11.0.0.47
$$ Generated using HyperMesh-Ls-dyna 971 Template Version : 11.0.0.47
*KEYWORD memory=250000000
*TITLE

*CONTROL_TERMINATION
$$  ENDTIM    ENDCYC     DTMIN    ENDENG    ENDMAS
2.6000E-04
*CONTROL_BULK_VISCOSITY
$$      Q1        Q2        IBQ
      2.0       0.1
$$DATABASE_OPTION -- Control Cards for ASCII output
*DATABASE_NODOUT
1.0000E-05         0
*DATABASE_BINARY_D3PLOT
$$ DT/CYCL      LCDT      BEAM     NPLTC
5.0000E-06
         0
*NODE
      1          -2.0         113.75          -2.4
…
569151          -4.75         120.25            0.0
*MAT_PLASTIC_KINEMATIC
$HMNAME MATS       5steel
         57.7400E-09  206842.0      0.33     470.0       0.0
       0.0       0.0       0.0
*MAT_JOHNSON_COOK
$HMNAME MATS       1nugget
         12.7700E-09   27481.0   73100.0      0.33
     248.5    714.59     0.537    0.0083       1.7     775.0     294.0       1.0
875000000.                            0.059      0.13      -1.5     0.011
       0.0
*MAT_JOHNSON_COOK
$HMNAME MATS       2TMAZ
         22.7700E-09   27481.0   73100.0      0.33
    139.28    632.48      0.29    0.0083       1.7     775.0     294.0       1.0
875000000.                            0.059      0.13      -1.5     0.011
```

```
      0.0
*MAT_JOHNSON_COOK
$HMNAME MATS       3HAZ
        32.7700E-09   27481.0   73100.0      0.33
   326.41    585.18     0.501    0.0083       1.7     775.0     294.0       1.0
875000000.                            0.087      0.13      -1.5     0.011
      0.0
*MAT_JOHNSON_COOK
$HMNAME MATS       42024
        42.7700E-09   27481.0   73100.0      0.33
    352.0     440.0      0.42    0.0083       1.7     775.0     294.0       1.0
875000000.                            0.13      0.13      -1.5     0.011
      0.0
*PART
$HMNAME COMPS       1nugget
$HWCOLOR COMPS       1       3

       1        1        1        2        3
$HMNAME COMPS       2TMAZ
$HWCOLOR COMPS       2      34

       2        1        2        2        3
$HMNAME COMPS       3HAZ
$HWCOLOR COMPS       3      43

       3        1        3        2        3
$HMNAME COMPS       4BM
$HWCOLOR COMPS       4      36

       4        1        4        2        3
$HMNAME COMPS       5projectile
$HWCOLOR COMPS       5      32

       5        1        5                 3
*SECTION_SOLID
$HMNAME PROPS       1solid
       1
*EOS_GRUNEISEN
$HMNAME PROPS       2eos4
       2 5328000.0     1.338                       2.0      0.48

*HOURGLASS
$HMNAME PROPS       3Hourglass
       3        5
*CONTACT_ERODING_SURFACE_TO_SURFACE_ID
$HMNAME GROUPS       1contact
$HWCOLOR GROUPS       1      50
       1
```

```
       5       2       3       2
     0.5

       1       1
*SET_PART_LIST
       2
       1       2       3       4
*ELEMENT_SOLID
     1      1   7868   8156   8204   7916  10172  10460  10508  10220
…
471000      5  507390  507441  507339  507288  503142  503143  502991
502990
$$
$$ Sets Defined In HyperMesh
$$
*SET_NODE_LIST
$HMSET
$HMNAME SETS       1gauge
       1
   502991
*BOUNDARY_SPC_NODE
$HMNAME LOADCOLS       1constraints
$HWCOLOR LOADCOLS       1      64
   562981                1       1       1       1       1       1
…
569150                1       1       1       1       1       1
$HMNAME LOADCOLS       2velocity
$HWCOLOR LOADCOLS       2      38
   504713                1       1       1       1       1       1
*INITIAL_VELOCITY_NODE
$HMNAME LOADCOLS       2velocity
$HWCOLOR LOADCOLS       2      38
   502990       0.0       0.0 -213400.0
…
568947       0.0       0.0 -213400.0
*DATABASE_HISTORY_NODE_SET_LOCAL
$HMNAME OUTPUTBLOCKS       1timehistory
       1       0       1
*INITIAL_STRESS_SOLID
1,1,0,0,0,
0,3.86E+001,0,0,0,0,0
…
420000,1,0,0,0,
0,-2.45E+001,0,0,0,0,0
*END
```